

**UCSF**

**UC San Francisco Electronic Theses and Dissertations**

**Title**

Chronic effects of traumatic brain injury on the corticothalamic circuit

**Permalink**

<https://escholarship.org/uc/item/4pq436j8>

**Author**

Holden, Stephanie

**Publication Date**

2020

Peer reviewed|Thesis/dissertation

Chronic effects of traumatic brain injury on the corticothalamic circuit

by  
Stephanie Holden

DISSERTATION  
Submitted in partial satisfaction of the requirements for degree of  
DOCTOR OF PHILOSOPHY

in  
Neuroscience

in the  
GRADUATE DIVISION  
of the  
UNIVERSITY OF CALIFORNIA, SAN FRANCISCO

Approved:

DocuSigned by:  
*Raymond Swanson* Raymond Swanson  
0DFAB9CE695D4BA... Chair

DocuSigned by:  
*Alexandra Nelson* Alexandra Nelson

DocuSigned by:  
*Kira Poskanzer* Kira Poskanzer

DocuSigned by:  
*Jeanne Paz* Jeanne Paz  
129DDCD87B64445...

---

Committee Members

Copyright 2020  
by  
Stephanie Holden

## **Acknowledgements**

I am so grateful for all the mentorship and support I have received throughout my PhD. First, I'd like to thank my thesis advisor, Jeanne Paz. She provided me with scientific and technical training and all the resources I could ask for so I could work on a project I was passionate about. I deeply admire her commitment to mentorship and appreciate how strongly she advocates for and supports her trainees. She has sent us to several international conferences, introduced us to her global network of scientific colleagues, and nominated us for several awards. Her optimism and unwavering belief in me gave me confidence and helped me to forge ahead through the ups and downs of graduate school.

Next, I'd like to thank the members of my qualifying and thesis committees: Felice Dunn, Alexandra Nelson, Kira Poskanzer, and Raymond Swanson, who served as my thesis committee chair. Their feedback helped to guide the direction of my project, especially in defining the scope of what was feasible or expected of me as a graduate student.

I would also like to specifically thank several colleagues in the Paz lab. I will never forget the support and kindness of Alexandra Clemente and Stefanie Makinson, who were my very first mentors in the lab. They made time to teach me new scientific techniques, answer my questions, and troubleshoot problems, and I looked forward to going to work every day because of them. Andrew Chang, Frances Cho, and Bryan Higashikubo have also been exceptional colleagues, co-authors, and friends. Thank you to Scott Brovarney and Irene Lew for being patient, attentive, and genial lab managers and for keeping our animal colonies running smoothly. Thanks to Joni Miyagi and Stephanie Tuazon, our administrative assistants, for keeping us updated on meetings and planning lab retreats. I also cannot forget all of the students we mentored in the lab, all of whom were quick learners and made impressive progress and contributions in such a short time. I learned so much and experienced great joy from teaching all of them.

I have had the pleasure of working with several collaborators on various projects, including the labs of Eleonora Aronica, Bruno Delord, Sheng Ding, Anita Luthi, and the scientists at Annexon Biosciences, Inc.

I'm lucky to have been part of many communities at UCSF – the two largest being the Neuroscience Graduate Program and the Gladstone Institutes. Thank you to all the people who have become scientific colleagues, mentors, and dear friends. I must acknowledge Françoise Chanut, a senior scientific editor at the Gladstone Institutes, who taught an excellent class on scientific writing and who edited my manuscript and thesis.

There are many people outside of the workplace who have been sources of love and support, and I would like to give a special thanks to my neuroscience program classmates, and my longest-running housemates Stefan Lemke, Match McGregor, and Perry Spratt for being my San Francisco family and making Fogwarts a fun and welcoming home.

Finally, I would like to thank my entire family, especially my sister and my parents, who have always believed in me and supported me with encouragement, laughter, and love. I would not be the scientist or the person I am today without them.

The work described in this thesis was supported by the Department of Defense, the National Institutes of Health/National Institute of Neurological Disorders and Stroke, the National Science Foundation, the Achievement Rewards for College Scientists (ARCS) Scholarship, and the Ford Foundation Dissertation Fellowship.

## Contributions

**Chapter 1** of this dissertation was written by Stephanie Holden, with a few paragraphs adapted from:

Cho, F.S., Clemente, A., Holden, S., Paz, J.T., 2017. Chapter 19 - Thalamic Models of Seizures *In Vitro*, in: Pitkänen, A., Buckmaster, P.S., Galanopoulou, A.S., Moshé, S.L. (Eds.), *Models of Seizures and Epilepsy* (Second Edition). Academic Press, pp. 273–284.

**Chapter 2** is reproduced in its entirety from:

Holden, S.S., Aboubakr, O., Higashikubo, B., Cho, F.S., Chang, A.H., Morningstar, A., Mathur, V., Kuhn, L.J., Suri, P., Sankaranarayanan, S., Andrews-Zwilling Y., Aronica, E., Yednock, T., Paz, J.T., 2020. Complement factor C1q mediates chronic neuron loss and inflammation post-brain injury. *bioRxiv*. 2020.05.29.120220 [Preprint] (2020). Available from: doi:10.1101/2020.05.29.120220.

SSH and JTP conceptualized the project, and wrote and edited the manuscript. SSH administered and/or carried out all experiments including investigation, analysis, and visualization. OA contributed to the anti-C1q histology study and did antibody treatments, histological staining, imaging, and image analysis under the mentorship of SSH. BH contributed to setup and data analysis for the chronic ECoG recordings. FSC helped with surgeries and data analysis for the chronic ECoG recordings. AHC and ARM contributed to histological staining and imaging. SS, YAZ, and TY provided the anti-C1q antibodies and gave feedback on all anti-C1q experiments. VM, LJK, and PS carried out all PK/PD ELISA assays. EA provided histological staining on postmortem brain tissue from human patients with TBI. JTP provided supervision and funding.

**Chapter 3** was written by Stephanie Holden. All research in this chapter represents ongoing and unpublished work. The work presented was done with help from Andrew H Chang, Frances S Cho, and Agnieszka Ciesielska in the Paz lab, and with our collaborators Changsheng Lin and Sheng Ding at the Gladstone Institutes, who provided the small molecule drugs. Henna Mohabbat and Chenyu Wang also contributed under the mentorship of Andrew Chang and Stephanie Holden.

**Chapter 4** is reproduced in its entirety from:

Rodriguez, G., Sarazin, M., Clemente, A., Holden, S., Paz, J.T., Delord, B., 2018. Conditional Bistability, a Generic Cellular Mnemonic Mechanism for Robust and Flexible Working Memory Computations. *J. Neurosci.* 38, 5209–5219.

GR, JTP, and BD conceptualized the project, and wrote and edited the manuscript. SSH and AC performed whole-cell patch-clamp electrophysiology recordings. GR and BD did all computational modeling.

**Chapter 5** was written by Stephanie Holden.

# **Chronic effects of traumatic brain injury on the corticothalamic circuit**

**Stephanie Holden**

## **Abstract**

Traumatic brain injury (TBI) affects 69 million people worldwide each year and is associated with many adverse health outcomes. But we still don't fully understand which cells or circuits in the brain are chronically disrupted by TBI, or how to prevent or treat these outcomes. TBI-related health outcomes likely reflect secondary injuries that arise over the long term as consequences of the initial impact. In Chapters 2 and 3, we investigate the secondary injury processes that develop in the corticothalamic circuit, using a mouse model of mild injury that only directly injures the cortex. In Chapter 2, we identify which intrinsic, synaptic, and bulk cortical properties in the peri-injured cortex and the functionally connected thalamus are chronically altered by TBI, using electrophysiological recordings approaches. We also explore the role of the C1q complement pathway in TBI, and we find that blocking C1q reduces inflammation and neuronal loss in the corticothalamic circuit. In Chapter 3, we test the chronic effects of a novel small molecule therapeutic that reprograms astrocyte transcriptional states on outcomes such as inflammation and seizure susceptibility after TBI. In Chapter 4, we explore the fundamental properties of working memory, a cognitive function that involves the prefrontal cortex. Working memory is one of many cognitive functions known to be disrupted in TBI but before we study this function in the context of disease, we first dive into the basic intrinsic properties of neurons that underlie working memory. Studying the cellular and circuit mechanisms of both basic cognitive functions such as working memory and chronic disease processes such as TBI will help to identify new targets and therapeutic treatments for TBI-related health outcomes.



## Table of Contents

<b>Chapter 1 : Introduction .....</b>	<b>1</b>
Figures .....	6
References .....	10
<b>Chapter 2 : Complement factor C1q mediates chronic neuron loss and inflammation post-brain injury .....</b>	<b>17</b>
Abstract .....	17
Introduction .....	18
Results .....	20
Discussion .....	25
Materials & Methods .....	29
Figures .....	37
References .....	55
<b>Chapter 3 : Investigating the therapeutic effects of small molecules on neuroinflammation and seizure susceptibility after traumatic brain injury .....</b>	<b>63</b>
Abstract .....	63
Introduction .....	64
Results .....	65
Discussion .....	68
Materials & Methods .....	70
Figures .....	73
References .....	80

<b>Chapter 4 : Conditional bistability, a generic cellular mnemonic mechanism for robust and flexible working memory computations.....</b>	<b>84</b>
Abstract.....	84
Introduction .....	85
Results .....	88
Discussion.....	95
Materials & Methods.....	101
Figures .....	107
References.....	113
<b>Chapter 5 : Conclusion &amp; Future Directions .....</b>	<b>121</b>
References.....	124

## List of Figures

### Chapter 1

Figure 1.1. Diagram of the corticothalamic circuit.....	6
Figure 1.2. Time course of inflammatory processes after traumatic brain injury. Adapted from Simon et al., 2017.....	7

### Chapter 2

Figure 2.1. The injured cortex and functionally connected thalamus show chronic inflammation and neuron loss three weeks after TBI.....	37
Figure 2.2. The nRT ipsilateral to the injured cortex shows neuron loss and altered IPSC and EPSC properties three weeks after TBI.....	38
Figure 2.3. Anti-C1q antibody reduces chronic inflammation and neuron loss three weeks after TBI.....	40
Figure 2.4. Chronically recorded TBI mice show altered power across different ECoG frequency bands. ....	41
Figure 2.5. Anti-C1q antibody has modest effects on ECoG spectral features in mice with TBI.....	43
Figure 2.S1. Postmortem brain tissue from a patient with TBI shows chronic inflammation eight days after TBI.....	45
Figure 2.S2. The injured cortex and functionally connected thalamus show chronic inflammation and neuron loss four months after TBI. ....	46
Figure 2.S3. C1q -/- mice show reduced inflammation and neuron loss three weeks after TBI.....	47

Figure 2.S4. Plasma and brain PK/PD show presence of free drug and reduced C1q in anti-C1q drug-treated sham and TBI mice.....48

Figure 2.S5. Mice with TBI have spontaneous seizure-like events in the theta to alpha frequency range that are time-locked with thalamic bursting. ....49

Figure 2.S6. Anti-C1q antibody has chronic disease-modifying effects on EcoG power in mice with TBI.....50

**Chapter 3**

Figure 3.1. Quantification of GFAP and NeuN fluorescence eight weeks after TBI..... 73

Figure 3.2. Quantification of vascular density eight weeks after TBI..... 74

Figure 3.3. Mice with TBI have higher PTZ-induced seizure susceptibility and reduced latency to myoclonic jerks three weeks after TBI..... 75

Figure 3.4. Two-week treatment of RA8 does not alter seizure susceptibility six weeks after TBI. .... 77

Figure 3.S1. RA8 reduces neuronal loss in VB via suppression of astroglial reactivation in a mouse model of post-stroke epilepsy. .... 78

Figure 3.S2. RA8 reduces long-term reactive astrogliosis in the peri-stroke cortex in a mouse model of post-stroke epilepsy. .... 79

**Chapter 4**

Figure 4.1. Conditional bistability is a hidden property in neurons endowed with a supra-threshold conductance in response to standard protocols applied “in vitro”..... 107

Figure 4.2. Existence and expression of conditional bistability “in vitro”. .... 108

Figure 4.3. Conditional bistability is a generic mnemonic property of neurons endowed with depolarizing spike-mediated mechanisms. .... 109

Figure 4.4. Conditional bistability confers robust event memory under strongly fluctuating synaptic inputs “in vivo” .....	110
Figure 4.5. Conditional bistability promotes irregular discharge under “in vivo” conditions.....	112

## List of Tables

### Chapter 1

Table 1.1. Strengths and weaknesses of commonly used animal models of TBI. Adapted from Xiong et al., 2013.....	8
Table 1.2. Major pathological features of animal models of TBI that are seen in human TBI. Adapted from Xiong et al., 2013 .....	9

### Chapter 2

Table 2.S1. Summary of intrinsic properties, EPSC, and IPSC data recorded from S1 cortex, VB, and nRT.....	52
Table 2.S2. Summary of epileptiform activity analysis in sham, TBI, control-treated TBI, and antibody-treated TBI mice. ....	54

## **Chapter 1 : Introduction**

### **Traumatic brain injury**

Traumatic brain injury (TBI) can be caused by any bump, blow, or jolt to the head that disrupts normal brain function, and affects about 69 million people worldwide each year (Dewan et al., 2018). Falls are the most common cause of TBI, particularly in older adults and young children. Other high-risk groups include military personnel and athletes, who may incur TBIs from vehicle collisions, sports injuries, and combat injuries (Broglia et al., 2017). TBI severity is commonly described as mild, moderate, or severe, based on a number of factors including duration of loss of consciousness and brain imaging results.

Severe TBIs can lead to life-long disability or death. In fact, TBIs contribute to about 30% of all injury-related deaths in the United States (Taylor et al., 2017). Severe TBI can affect all aspects of an individual's life, including relationships, the ability to work or study, doing household tasks, driving, or participating in other daily activities (Thurman et al., 1999). Concussions, on the other hand, are typically considered to be mild TBIs, and are characterized by little to no loss of consciousness or post-traumatic amnesia. Mild TBIs can still result in physical symptoms like headaches, dizziness, confusion, slurred speech, and difficulty with concentration, sleep, and sensory processing (Prince and Bruhns, 2017), but symptoms often resolve within a few days to weeks. However, one major challenge in understanding the long-term effects of mild TBIs is that epidemiological studies often gather data based on hospital admissions, but many people who suffer from mild TBI do not seek hospitalization.

TBI is also a risk factor for other diseases including stroke, epilepsies like Lennox-Gastaut Syndrome and post-traumatic epilepsy (Asadi-Pooya 2017, Kim et al., 2018), and for later development of neurodegenerative diseases and dementia (Wilson et al., 2017). Most of these symptoms and adverse health outcomes develop months or years after TBI and are likely caused

by indirect secondary injuries, which are long-term consequences of the initial impact (Simon et al., 2017). Because the primary injury is essentially irreversible, understanding the timing, mechanisms, and location of secondary injuries in the brain are crucial for preventing or treating disability following TBI.

Animal models of TBI are especially useful for studying the biomechanical, cellular, and molecular aspects of TBI that cannot be addressed in a clinical setting, as well as for developing novel therapeutic interventions (Bramlett et al., 2007, Chen et al., 2009, Ma et al., 2019, Marklund et al., 2012, Pierce et al., 1998, Shear et al., 2009, Xiong et al., 2014, Zhu et al., 2019). Specifically, rodents are often used for TBI research due to factors like cost, size, and standardized outcome measurements. The most common TBI models are controlled cortical impact (CCI), fluid percussion injury (FPI), weight drop injury, and blast injury (Carbonell et al., 1998, Smith et al., 2005, Xiong et al., 2014, Ma et al., 2019, Wang et al., 2011). Each model has its own strengths and weaknesses (**Table 1.1 adapted from Xiong et al., 2014**), but for our studies we selected the CCI model, which uses an electromagnetic device to impact the exposed dura through a craniotomy. The major advantage of CCI is its high reproducibility, because mechanical parameters including depth, dwell time, and speed of the impact are easily controlled, and because the craniotomy reduces variability that may be caused by skull thickness. CCI is also known to reproduce many pathophysiological and cognitive deficits observed in humans with TBI (**Table 1.2 adapted from Xiong et al., 2014**, Lee et al., 2019, Ma et al., 2019, Washington et al., 2012).

### **The cortico-thalamo-cortical circuit**

The cortex is often the site of primary injury because it sits directly beneath the skull, and is an integrated part of many larger circuits, including the cortico-thalamo-cortical loop. This loop is composed of reciprocally connected excitatory thalamocortical (TC) and corticothalamic (CT)



pathways. Glutamatergic TC neurons of the relay nuclei have reciprocal connections with (1) glutamatergic CT neurons in functionally related areas of the cortex, and (2) inhibitory GABAergic neurons in the thalamic reticular nucleus (nRT) (Houser et al., 1980). The nRT also receives glutamatergic projections from the cortex (Cruikshank et al., 2010; Destexhe et al., 1998, Paz et al., 2011) (**Figure 1.1**). Through these connections, the thalamus generates and propagates rhythmic activity to the cortex (Destexhe et al., 1998, Fernandez et al., 2018, Pinault and Deschênes, 1992, Rovó et al., 2014, Timofeev and Chauvette., 2011).

Cortical and TC neurons excite nRT neurons, leading to the inhibition of TC neurons (**Figure 1.1**). This is followed by post-inhibitory rebound bursts of action potentials in TC neurons (mediated by T-type  $\text{Ca}^{2+}$  channels) that, in turn, re-excite nRT neurons. This alternation of nRT and TC neuron bursting generates rhythmic activity that can be seen in electroencephalography (EEG) recordings of normal individuals during non-REM sleep (Huguenard and McCormick, 2007). These sleep spindles, among the best-described thalamocortical rhythms, are intermittent 10–15 Hz oscillations lasting one to three seconds (Beenhakker and Huguenard, 2009, Huguenard and McCormick, 2007, Timofeev and Steriade. 1996, Wang and Rinzel, 1993). Because TC neurons can then propagate this oscillatory activity to cortical neurons, spindle activity can be relatively generalized. For example, simultaneous recordings in the thalamus and cortex of cats revealed a high correlation between thalamic activity and cortical spindles (Andersen et al., 1967). Also, *in vitro* thalamic slice preparations can sustain robust spindle-like network activity (Huntsman et al., 1999, Jacobsen et al., 2001). These data support a role for the thalamus in generating and propagating rhythmic activity to the cortex to mediate network oscillations associated with normal functions (e.g., sleep).

Although it is not acutely injured in most mild TBI cases, the thalamus experiences secondary injury presumably induced via its connections with the damaged cerebral cortex (Antón-Bolaños et al., 2018; Auladell et al., 2000; Beenhakker and Huguenard, 2009; Blakemore and Molnár,

1990; Paz and Huguenard, 2015). Structural changes in the thalamus have been implicated in a number of long-term health outcomes after TBI, including fatigue and cognitive dysfunction (Grossman et al., 2012; Grossman and Inglese, 2016), and patients with TBI display secondary and chronic neurodegeneration and inflammation in thalamic nuclei (Ross and Ebner, 1990; Scott et al., 2015).

### **Inflammation in TBI**

Chronic neuroinflammation, which is characterized by the activation of glial cells, leukocyte recruitment, and upregulation and secretion of cytokines and chemokines, is a common feature of both primary and secondary injury stages (Morganti-Kossmann et al., 2001, Simon et al., 2017). However, most attempts to improve post-TBI cognitive outcomes with broad anti-inflammatory agents have failed (Russo and McGavern, 2016, Simon et al., 2017). This failure likely reflects the fact that different inflammatory pathways may play protective and pathogenic roles at different times (Orme et al., 2015, **Figure 1.2 adapted from Simon et al., 2017**).

In Chapters 2 and 3, I describe my work on the role of the thalamus in TBI. This work is based on the fundamental hypothesis that the thalamus is an important site of secondary injury because of its reciprocal connections with the cortex. During my thesis, I expanded upon TBI studies that have characterized pathology and hyperexcitability in the cortex. To understand how cortical injury could cause secondary injury in the thalamus, I optimized CCI parameters to directly injure only the cortex without affecting subcortical structures, then used electrophysiological approaches to investigate how cellular and synaptic properties across the entire cortico-thalamo-cortical circuit were altered by TBI. I also investigated whether one particular inflammatory pathway, the C1q complement pathway, is necessary for neuronal loss and chronic inflammation in TBI. Finally, I tested whether small molecule therapeutics could alter TBI pathophysiologies such as seizure susceptibility and neuroinflammation.

## **Persistent neural activity in working memory**

In addition to studying the mechanisms of cellular and circuit excitability in disease, we are also interested in fundamental principles that underlie neural excitability in normal cognition. The prefrontal cortex (PFC) plays an important role in higher cognitive functions including working memory, which involves both the short-term storage and the manipulation of information (Courtney et al., 1998, Funahashi 2017). Working memory is known to be disrupted in TBI (Hamm et al., 1996, McDowell et al., 1997), but we need to know the basic mechanisms of working memory before we can study it in the context of disease. In Chapter 4, I describe my use of whole-cell patch-clamp recordings and computational modeling to investigate the intrinsic properties of neurons that display persistent activity, which is a neural correlate of working memory.

## Figures

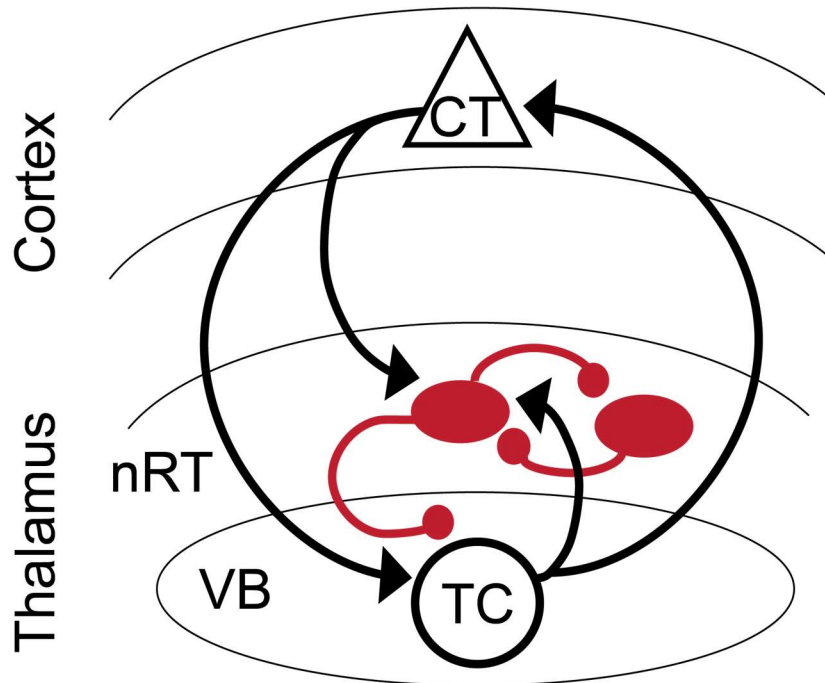


**Figure 1.1. Diagram of the corticothalamic circuit.**

Black shapes and arrows represent glutamatergic neurons and projections. Red shapes and connections represent GABAergic neurons and projections. CT = corticothalamic neurons, nRT = reticular thalamic nucleus, TC = thalamocortical neurons, VB = ventrobasal thalamus.

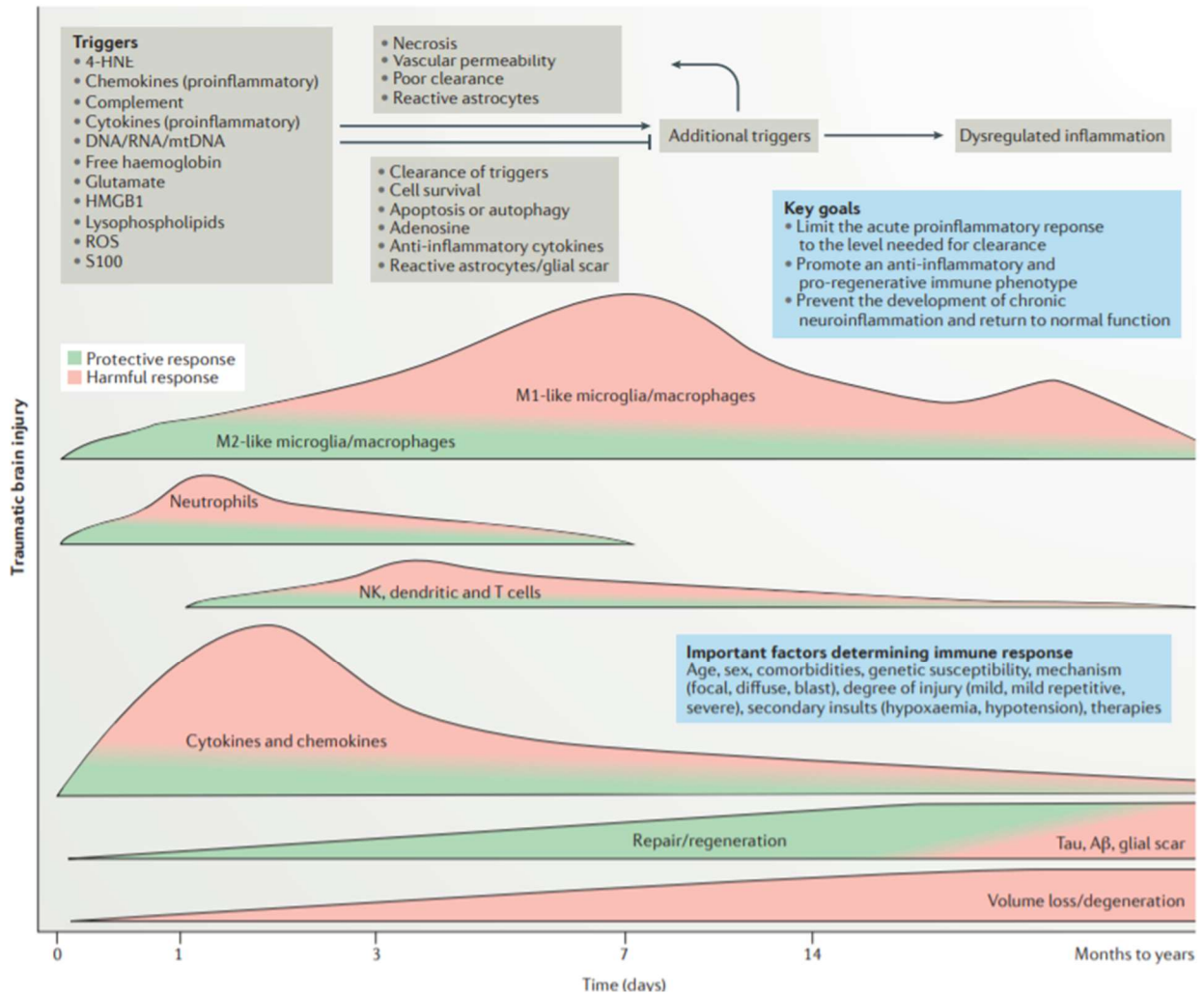


**Figure 1.2. Time course of inflammatory processes after traumatic brain injury. Adapted from Simon et al., 2017.**

**Table 1.1. Strengths and weaknesses of commonly used animal models of TBI. Adapted from Xiong et al., 2013.**

Table 1   Commonly used animal models of TBI					
Model	Type of injury	Strengths	Weaknesses	Species	Refs
<i>Weight-drop models</i>					
Feeney's	Mainly focal	Biomechanics of injury mechanism are similar to those seen in human TBI	Need for craniotomy; high mortality rate	Rat	86
Shohami's	Mainly focal	Device is easy to operate; neurological severity score can be used with model at 1 h post-injury to evaluate neurological impairment	Not highly reproducible	Rat, mouse	90,91
Marmarou's	Mainly diffuse	Biomechanics of injury mechanism are similar to those seen in human TBI; model is well characterized	Not highly reproducible; high mortality rate following injury without ventilation	Rat, mouse	26,95
Maryland's	Mainly diffuse	Biomechanics of injury mechanism are similar to those seen in human TBI	Needs further characterization	Rat	101
<i>Fluid percussion injury models</i>					
Middle	Mixed	Highly reproducible; allows fine tuning of injury severity	Need for craniotomy; high mortality rate	Cat, rabbit, rat, dog, sheep, swine	30,37,38,42,45
Lateral	Mixed	Highly reproducible; allows fine tuning of injury severity	Need for craniotomy; high mortality rate	Rat, mouse, swine	31,40,224
<i>Other models</i>					
Controlled cortical impact injury	Mainly focal	Highly reproducible; low mortality rate	Need for craniotomy	Ferret, mouse, rat, swine, monkey	24,25,56,58,59
Blast injury	Mainly diffuse	Biomechanics of injury mechanism are similar to those seen in military TBI	Needs standardization	Rat, mouse, swine	27, 94, 108
Repeated mild TBI	Mainly diffuse	Biomechanics of injury mechanism are similar to those seen in sport TBI	Needs further characterization	Rat, mouse, swine	104,126,132
Penetrating ballistic-like brain injury	Mainly focal	Biomechanics of injury mechanism are similar to those seen in human TBI	Needs standardization	Cat, rat	72,73,75

TBI, traumatic brain injury. The table is modified from REF. 225

**Table 1.2. Major pathological features of animal models of TBI that are seen in human TBI. Adapted from Xiong et al., 2013**

Table 2 | Major pathological features of animal models of TBI that are seen in human TBI

TBI model	Concussion	Contusion	Traumatic axonal injury	Haemorrhage	Skull fracture	Refs
Shohami's and Marmarou's weight-drop models	++	+	++	+	+/-	26,84,90,91,177
Feeney's weight-drop model	+	++	+	+	-	86
Maryland's model	+	-	++	+	-	101
Fluid percussion injury	+	++	+	+	-	8,20,36,44,129,130,139-146,159
Controlled cortical impact injury	+	++	+	++	-	24,25,50,56-59,63-71
Blast injury	++	+/-	++	+	+/-	27,105-107,109-119
Penetrating ballistic-like brain injury	+	++	+	++	+/-	72,74,76-83,85

TBI, traumatic brain injury. -, does not replicate the condition observed in humans; +/-, might replicate the condition observed in humans; +, replicates the human condition to some degree; ++, high fidelity to the human condition.

## References

- Antón-Bolaños, N., Espinosa, A., López-Bendito, G., 2018. Developmental interactions between thalamus and cortex: a true love reciprocal story. *Curr. Opin. Neurobiol.* 52, 33–41.
- Asadi-Pooya, A.A., 2018. Lennox-Gastaut syndrome: a comprehensive review. *Neurol Sci* 39, 403–414.
- Auladell, C., Pérez-Sust, P., Supèr, H., Soriano, E., 2000. The early development of thalamocortical and corticothalamic projections in the mouse. *Anat. Embryol.* 201, 169–179.
- Beenhakker, M.P., Huguenard, J.R., 2009. Neurons that fire together also conspire together: is normal sleep circuitry hijacked to generate epilepsy? *Neuron* 62, 612–632.
- Blakemore, C., Molnár, Z., 1990. Factors involved in the establishment of specific interconnections between thalamus and cerebral cortex. *Cold Spring Harb. Symp. Quant. Biol.* 55, 491–504.
- Bramlett, H.M., Dietrich, W.D., 2007. Progressive damage after brain and spinal cord injury: pathomechanisms and treatment strategies, in: Weber, J.T., Maas, A.I.R. (Eds.), *Progress in Brain Research, Neurotrauma: New Insights into Pathology and Treatment*. Elsevier, pp. 125–141.
- Broglio, S.P., McCrea, M., McAllister, T., Harezlak, J., Katz, B., Hack, D., Hainline, B., CARE Consortium Investigators, 2017. A National Study on the Effects of Concussion in Collegiate Athletes and US Military Service Academy Members: The NCAA-DoD Concussion Assessment,



Research and Education (CARE) Consortium Structure and Methods. *Sports Med* 47, 1437–1451.

Carbonell, W.S., Maris, D.O., McCall, T., Grady, M.S., 1998. Adaptation of the fluid percussion injury model to the mouse. *J. Neurotrauma* 15, 217–229.

Chen, Z., Tortella, F.C., Dave, J.R., Marshall, V.S., Clarke, D.L., Sing, G., Du, F., Lu, X.-C.M., 2009. Human Amnion-Derived Multipotent Progenitor Cell Treatment Alleviates Traumatic Brain Injury-Induced Axonal Degeneration. *Journal of Neurotrauma* 26, 1987–1997.

Courtney, S.M., Petit, L., Haxby, J.V., Ungerleider, L.G., 1998. The role of prefrontal cortex in working memory: examining the contents of consciousness. *Philos Trans R Soc Lond B Biol Sci* 353, 1819–1828.

Cruikshank, S.J., Urabe, H., Nurmikko, A.V., Connors, B.W., 2010. Pathway-specific feedforward circuits between thalamus and neocortex revealed by selective optical stimulation of axons. *Neuron* 65, 230–245.

Destexhe, A., Contreras, D., Steriade, M., 1998. Mechanisms underlying the synchronizing action of corticothalamic feedback through inhibition of thalamic relay cells. *J. Neurophysiol.* 79, 999–1016.

Dewan, M.C., Rattani, A., Gupta, S., Baticulon, R.E., Hung, Y.-C., Punchak, M., Agrawal, A., Adeleye, A.O., Shrimel, M.G., Rubiano, A.M., Rosenfeld, J.V., Park, K.B., 2018. Estimating the global incidence of traumatic brain injury. *J. Neurosurg.* 1–18.

Fernandez, L.M., Vantomme, G., Osorio-Forero, A., Cardis, R., Béard, E., Lüthi, A., 2018. Thalamic reticular control of local sleep in mouse sensory cortex. *Elife* 7.

Funahashi, S., 2017. Working Memory in the Prefrontal Cortex. *Brain Sci* 7.

Grossman, E.J., Ge, Y., Jensen, J.H., Babb, J.S., Miles, L., Reaume, J., Silver, J.M., Grossman, R.I., Inglese, M., 2012. Thalamus and cognitive impairment in mild traumatic brain injury: a diffusional kurtosis imaging study. *J. Neurotrauma* 29, 2318–2327.

Grossman, E.J., Inglese, M., 2016. The Role of Thalamic Damage in Mild Traumatic Brain Injury. *J. Neurotrauma* 33, 163–167.

Hamm, R.J., Temple, M.D., Pike, B.R., O'Dell, D.M., Buck, D.L., Lyeth, B.G., 1996. Working memory deficits following traumatic brain injury in the rat. *J. Neurotrauma* 13, 317–323.

Houser, C.R., Vaughn, J.E., Barber, R.P., Roberts, E., 1980. GABA neurons are the major cell type of the nucleus reticularis thalami. *Brain Res.* 200, 341–354.

Huguenard, J.R., McCormick, D.A., 2007. Thalamic synchrony and dynamic regulation of global forebrain oscillations. *Trends Neurosci.* 30, 350–356.

Huntsman, M.M., Porcello, D.M., Homanics, G.E., DeLorey, T.M., Huguenard, J.R., 1999. Reciprocal Inhibitory Connections and Network Synchrony in the Mammalian Thalamus. *Science* 283, 541–543.

- Jacobsen, R.B., Ulrich, D., Huguenard, J.R., 2001. GABA(B) and NMDA receptors contribute to spindle-like oscillations in rat thalamus in vitro. *J. Neurophysiol.* 86, 1365–1375.
- Kim, J.A., Boyle, E.J., Wu, A.C., Cole, A.J., Staley, K.J., Zafar, S., Cash, S.S., Westover, M.B., 2018. Epileptiform activity in traumatic brain injury predicts post-traumatic epilepsy. *Ann. Neurol.* 83, 858–862.
- Lee, S.-W., Jang, M.-S., Jeong, S.-H., Kim, H., 2019. Exploratory, cognitive, and depressive-like behaviors in adult and pediatric mice exposed to controlled cortical impact. *Clin Exp Emerg Med* 6, 125–137.
- Ma, X., Aravind, A., Pfister, B.J., Chandra, N., Haorah, J., 2019. Animal Models of Traumatic Brain Injury and Assessment of Injury Severity. *Mol. Neurobiol.* 56, 5332–5345.
- Marklund, N., Hillered, L., 2011. Animal modelling of traumatic brain injury in preclinical drug development: where do we go from here? *British Journal of Pharmacology* 164, 1207–1229.
- McDowell, S., Whyte, J., D'Esposito, M., 1997. Working memory impairments in traumatic brain injury: evidence from a dual-task paradigm. *Neuropsychologia* 35, 1341–1353.
- Morganti-Kossmann, M.C., Rancan, M., Otto, V.I., Stahel, P.F., Kossmann, T., 2001. Role of cerebral inflammation after traumatic brain injury: a revisited concept. *Shock* 16, 165–177.
- Orme, I.M., Robinson, R.T., Cooper, A.M., 2015. The balance between protective and pathogenic immune responses in the TB-infected lung. *Nat. Immunol.* 16, 57–63.

- Paz, J.T., Bryant, A.S., Peng, K., Fenno, L., Yizhar, O., Frankel, W.N., Deisseroth, K., Huguenard, J.R., 2011. A new mode of corticothalamic transmission revealed in the Gria4(-/-) model of absence epilepsy. *Nat. Neurosci.* 14, 1167–1173.
- Paz, J.T., Huguenard, J.R., 2015. Microcircuits and their interactions in epilepsy: is the focus out of focus? *Nat. Neurosci.* 18, 351–359.
- Pierce, J.E.S., Smith, D.H., Trojanowski, J.Q., McIntosh, T.K., 1998. Enduring cognitive, neurobehavioral and histopathological changes persist for up to one year following severe experimental brain injury in rats. *Neuroscience* 87, 359–369.
- Pinault, D., Deschênes, M., 1992. Voltage-dependent 40-Hz oscillations in rat reticular thalamic neurons in vivo. *Neuroscience* 51, 245–258.
- Prince, C., Bruhns, M.E., 2017. Evaluation and Treatment of Mild Traumatic Brain Injury: The Role of Neuropsychology. *Brain Sci* 7.
- Ross, D.T., Ebner, F.F., 1990. Thalamic retrograde degeneration following cortical injury: an excitotoxic process? *Neuroscience* 35, 525–550.
- Rovó, Z., Mátyás, F., Barthó, P., Slézia, A., Lecci, S., Pellegrini, C., Astori, S., Dávid, C., Hangya, B., Lüthi, A., Acsády, L., 2014. Phasic, nonsynaptic GABA-A receptor-mediated inhibition entrains thalamocortical oscillations. *J. Neurosci.* 34, 7137–7147.
- Russo, M.V., McGavern, D.B., 2016. Inflammatory neuroprotection following traumatic brain injury. *Science* 353, 783–785.

Scott, G., Hellyer, P.J., Ramlackhansingh, A.F., Brooks, D.J., Matthews, P.M., Sharp, D.J., 2015.

Thalamic inflammation after brain trauma is associated with thalamo-cortical white matter damage. *J Neuroinflammation* 12, 224.

Shear, D.A., Williams, A.J., Sharrow, K., Lu, X.-C.M., Tortella, F.C., 2009. Neuroprotective profile of

dextromethorphan in an experimental model of penetrating ballistic-like brain injury.

*Pharmacology Biochemistry and Behavior* 94, 56–62.

Simon, D.W., McGeachy, M.J., Bayir, H., Clark, R.S.B., Loane, D.J., Kochanek, P.M., 2017. The far-

reaching scope of neuroinflammation after traumatic brain injury. *Nat Rev Neurol* 13, 171–191.

Smith, D.H., Soares, H.D., Pierce, J.S., Perlman, K.G., Saatman, K.E., Meaney, D.F., Dixon, C.E.,

McINTOSH, T.K., 1995. A Model of Parasagittal Controlled Cortical Impact in the Mouse:

Cognitive and Histopathologic Effects. *Journal of Neurotrauma* 12, 169–178.

Taylor, C.A., Bell, J.M., Breiding, M.J., Xu, L., 2017. Traumatic Brain Injury-Related Emergency

Department Visits, Hospitalizations, and Deaths - United States, 2007 and 2013. *MMWR*

*Surveill Summ* 66, 1–16.

Thurman, D.J., Alverson, C., Dunn, K.A., Guerrero, J., Sniezek, J.E., 1999. Traumatic brain injury in

the United States: A public health perspective. *J Head Trauma Rehabil* 14, 602–615.

Timofeev, I., Chauvette, S., 2011. Thalamocortical oscillations: local control of EEG slow waves. *Curr*

*Top Med Chem* 11, 2457–2471.

- Timofeev, I., Steriade, M., 1996. Low-frequency rhythms in the thalamus of intact-cortex and decorticated cats. *J. Neurophysiol.* 76, 4152–4168.
- Wang, X.J., Rinzel, J., 1993. Spindle rhythmicity in the reticularis thalami nucleus: synchronization among mutually inhibitory neurons. *Neuroscience* 53, 899–904.
- Wang, Y., Wei, Y., Oguntayo, S., Wilkins, W., Arun, P., Valiyaveetil, M., Song, J., Long, J.B., Nambiar, M.P., 2011. Tightly coupled repetitive blast-induced traumatic brain injury: development and characterization in mice. *J. Neurotrauma* 28, 2171–2183.
- Washington, P.M., Forcelli, P.A., Wilkins, T., Zapple, D.N., Parsadonian, M., Burns, M.P., 2012. The Effect of Injury Severity on Behavior: A Phenotypic Study of Cognitive and Emotional Deficits after Mild, Moderate, and Severe Controlled Cortical Impact Injury in Mice. *Journal of Neurotrauma* 29, 2283–2296.
- Wilson, L., Stewart, W., Dams-O'Connor, K., Diaz-Arrastia, R., Horton, L., Menon, D.K., Polinder, S., 2017. The chronic and evolving neurological consequences of traumatic brain injury. *Lancet Neurol* 16, 813–825.
- Xiong, Y., Mahmood, A., Chopp, M., 2013. Animal models of traumatic brain injury. *Nat. Rev. Neurosci.* 14, 128–142.
- Zhu, B., Eom, J., Hunt, R.F., 2019. Transplanted interneurons improve memory precision after traumatic brain injury. *Nat Commun* 10, 5156.

## **Chapter 2 : Complement factor C1q mediates chronic neuron loss and inflammation post-brain injury**

### **Abstract**

While traumatic brain injury (TBI) acutely disrupts the cortex, most TBI-related disabilities reflect secondary injuries that accrue over time. The thalamus is a likely site of secondary damage because of its reciprocal connections with the cortex. Using a mouse model of cortical injury that does not directly damage subcortical structures, we found a chronic increase in C1q expression specifically in the corticothalamic circuit. Increased C1q expression co-localized with neuron loss and chronic inflammation, and correlated with altered cortical rhythms. Blocking C1q counteracted most of these outcomes, suggesting that C1q is a disease modifier in TBI. Since the corticothalamic circuit is important for sensory processing, attention, cognition, and sleep, all of which can be impaired by TBI, this circuit could be a new target for treating TBI-related disabilities.

## Introduction

Traumatic brain injury (TBI) affects about 69 million people worldwide every year (Dewan et al., 2018) and can lead to cognitive dysfunction, difficulty with sensory processing, sleep disruption, and the development of epilepsy. Most of these adverse health outcomes develop months or years after TBI and are caused by indirect secondary injuries that result in long-term consequences of the initial impact (Mckee and Daneshvar, 2015). Because the primary injury is essentially irreversible, understanding where, when, and how secondary injuries develop is crucial for preventing or treating disability following TBI.

The cortex is often the site of primary injury because it sits directly beneath the skull, and is an integrated part of many larger circuits, including the cortico-thalamo-cortical loop. This circuit is important for sensory processing, attention, cognition, and sleep, all of which can be impaired by TBI (Briggs and Usrey, 2008, Wimmer et al., 2015, Yingling and Skinner, 1976). The thalamus itself, though not acutely injured in most TBI cases, experiences secondary injury, presumably because of its long-range reciprocal connections with the cerebral cortex (Antón-Bolaños et al., 2018; Auladell et al., 2000; Beenhakker and Huguenard, 2009; Blakemore and Molnár, 1990; Paz and Huguenard, 2015). Structural changes in the thalamus have been implicated in a number of long-term TBI-related health outcomes, including fatigue and cognitive dysfunction (Grossman et al., 2012; Grossman and Inglese, 2016), and patients with TBI display secondary and chronic neurodegeneration and inflammation in thalamic nuclei (Ross and Ebner, 1990; Scott et al., 2015).

Chronic neuroinflammation is a common feature of secondary injury sites (Simon et al., 2017). But most attempts to improve post-TBI cognitive outcomes with broad anti-inflammatory agents have failed (Russo and McGavern, 2016; Simon et al., 2017), likely because there are many inflammatory pathways that play both protective and pathogenic roles at different times (Orme et al., 2015). A potential mediator of post-TBI inflammation and injury is the complement pathway,



which is activated in the peri-injury area of brain lesions in both humans and rodents (Bellander et al., 2001; Krukowski et al., 2018; You et al., 2007). Complement activation contributes to inflammation and neurotoxicity in central nervous system injury and is increased in human brains afflicted with injury, epilepsy, and Alzheimer's disease (Bellander et al., 2001; Hammad et al., 2018; Hong et al., 2016; Lui et al., 2016; Wyatt et al., 2017). Aberrant activation of C1q, the initiating molecule of the classical complement cascade, can trigger elimination of functioning synapses and contribute to the progression of neurodegenerative disease (Cho, 2019). On the other hand, C1q is involved in normal synapse pruning during development (Stevens et al., 2007) and the complement system plays an important part in brain homeostasis by clearing cellular debris and protecting the central nervous system from infection (Hammad et al., 2018).

Here, we investigated the role of classical complement protein C1q in post-TBI impairment of the corticothalamic circuit, with a particular emphasis on the timing and location of C1q expression. We used a mouse model of mild TBI, and monitored neurophysiological changes in the corticothalamic circuit via cellular electrophysiology and wireless cortical recordings in freely behaving mice up to four months post-TBI.

## Results

### Secondary C1q expression coincides with chronic inflammation, neurodegeneration, and synaptic dysfunction in the thalamus

To determine the secondary, long-term effects of TBI, we induced a mild cortical impact injury to the right primary somatosensory cortex (S1) of adult mice (**Figure 2.1A**), and assessed the impact on their brains three weeks later. This period corresponds to the latent phase in humans, when the brain is undergoing adaptive and maladaptive changes (Ding et al., 2016). We determined neuron count and gliotic inflammation in the corticothalamic circuit by immunofluorescent staining of coronal brain sections with markers of neurons (NeuN) and of glial inflammation (C1q, complement pathway; GFAP, astrocytes; Iba1, microglia/macrophages) (**Figure 2.1C-E**). Three weeks post-surgery, TBI mice had significantly higher GFAP, C1q, and Iba1 expression in the peri-TBI S1 cortex, the functionally connected ventrobasal thalamus (VB), and the reticular thalamic nucleus (nRT) than sham mice (**Figure 2.1B-E**). Inflammation occurred within 24 hours after injury in the cortex, while the functionally connected nRT and VB displayed glial changes around five days later (not shown), suggesting secondary thalamic inflammation. We also saw increased expression of similar inflammatory markers in thalamic tissue from human TBI patients, confirming that thalamic inflammation is a consequence of TBI in humans too (**Figure 2.S1**). We conclude that a chronic inflammatory process, secondary to the injury and characterized by C1q expression, occurs in the thalamus.

Glial inflammation was associated with significant neuronal loss in the thalamic region, particularly in the nRT (**Figure 2.1D-E, Figure 2.2A**), which receives the majority of its glutamatergic inputs from the cortex (Destexhe et al., 1998; Golshani et al., 2001). The nRT of TBI mice had significantly fewer neurons than sham mice, particularly in the region of the nRT that receives most of its excitatory inputs from the injured somatosensory cortex (Bourassa et al., 1995; Destexhe et al., 1998; Golshani et al., 2001; Lam and Sherman, 2011) (**Figure 2.2B-C**). This

result suggests that the inflammation, which may be initiated by retrograde axonal degeneration, follows the long-range, corticothalamic circuit, and marks its two ends: the injured cortex and the connected thalamus.

To test whether C1q might mark functional damage in this circuit, we performed whole-cell patch-clamp recordings in the cortex and thalamus in brain slices at chronic stages of TBI (three to six weeks). We recorded layer-5 pyramidal neurons and fast-spiking GABAergic interneurons in the peri-TBI S1 cortex, glutamatergic neurons in the VB, and GABAergic neurons in the nRT. The neurons' intrinsic membrane electrical properties and the spontaneous excitatory and inhibitory postsynaptic current (sEPSC and sIPSC) properties were similar between sham and TBI mice in both the peri-TBI cortex and the VB thalamus (see **Table 2.S1** for details). However, in the nRT, TBI led to a reduction in the frequency of sIPSCs (**Figure 2.2D-E**). Furthermore, nRT sEPSCs were smaller in amplitude, and trended toward a lower frequency (**Figure 2.2F-G**). Immunofluorescence staining for GFP in Thy1-GCaMP6f mice, a marker of neuronal calcium levels in corticothalamic neurons, revealed reduced corticothalamic fluorescence in the thalamus after TBI (**Figure 2.2H-I**), suggesting that this circuit is indeed impaired.

We conclude that the major long-term effect of TBI on corticothalamic circuits involves disruption of synaptic transmission in the nRT, which coincides with increased C1q expression, reduced cortical inputs, and local neuronal loss. In contrast, neurons in the peri-TBI cortex and the VB appear normal at chronic stages post-TBI (**Table 2.S1**), suggesting that inflammation - in particular, increased C1q expression - in these regions is not associated with long-term dysfunction in neuronal excitability or synaptic function.

### **Blocking C1q function reduces chronic glial inflammation and neuron loss**

Increased C1q expression persisted four months post-TBI (**Figure 2.S2A-S2B**). To test C1q's causal involvement in the inflammation and neuronal loss observed three weeks post-TBI, we used an antibody that specifically binds to C1q and blocks its downstream activity (Lansita et al., 2017). Mice were given i.p. injections of the C1q antibody or a mouse IgG1 isotype control 24

hours after TBI or sham surgery, followed by twice weekly treatments for three weeks (see methods for more details).

TBI mice treated with the anti-C1q antibody showed a strong reduction in inflammation and reduced neuronal loss (**Figure 2.3A-C**) relative to control-treated TBI mice, and on average had the same number of nRT neurons as antibody-treated sham mice (**Figure 2.3C**). TBI mice treated with the control still showed inflammation and neuron loss three weeks after TBI (**Figure 2.3**). As an alternative approach to the antibody treatment, we repeated the study using C1q  $-/-$  mice and found that TBI C1q  $-/-$  mice also exhibited reduced chronic inflammation and reduced neuron loss in the nRT (**Figure 2.S3**).

To confirm presence and effects of the anti-C1q antibody in the brain, we measured free drug, free and total C1q, C1s, and albumin levels in naïve, sham and TBI brains after two doses of control or antibody treatment (**Figure S4**). In plasma from the treated mice, free anti-C1q antibody was observed in both sham and TBI mice treated with the drug (**Figure S4A**). In agreement, we found that total C1q protein was undetectable in drug-treated animals using an assay that is not affected by free drug. These results suggest that drug-bound C1q is fully cleared from the circulation. Free anti-C1q antibody was observed in treated sham and TBI mice: 0.4-8.6 ug/ml in the ipsilateral side and 0.09-3.8 ug/ml in the contralateral side. The sham and TBI injuries led to a significant increase in ipsilateral C1q and small increase in contralateral C1q in untreated mice. In the anti-C1q treated sham and TBI mice, total C1q levels were significantly reduced in the ipsilateral side and showed trends of reduction in the contralateral side. Measurable levels of free anti-C1q antibody were observed, suggesting that C1q was fully saturated, but not fully cleared as in the periphery.

These outcomes indicate that C1q may lead to inflammation and neuron loss in TBI, and that blocking C1q reduces these deleterious effects.

### **TBI leads to long-term changes in cortical states and excitability in freely behaving mice**

We next investigated the longitudinal impact of mild TBI, using brain rhythms as a readout of corticothalamic circuit function *in vivo*. To this end, we implanted chronic wireless electrocorticographic (ECoG) devices into sham and TBI mice during the craniotomy/TBI induction surgery, returned mice to their home cages for chronic recording, and analyzed changes in ECoG power over time (**Figure 2.4A-H**). We observed a chronic increase in broadband power in TBI during both light epochs (**Figure 2.4C-H**) and dark epochs (data not shown).

Given that severe TBI has been shown to lead to epileptogenesis over time (Bolkvadze and Pitkänen, 2012; Bragin et al., 2016), we investigated whether mild TBI also resulted in epileptogenesis. We quantified different types of epileptic activities including epileptiform spikes, epileptic discharges, spike-and-wave discharges, and spontaneous focal or generalized seizures at 24 hours and three weeks post-TBI using previously reported classification (Bolkvadze and Pitkänen, 2012; Bragin et al., 2016). In the first 24 hours, 3 out of 16 TBI mice, but none of the 8 sham mice, showed generalized tonic-clonic seizures (GTCSs, **Table 2.S2**). None of the mice showed GTCSs at later time points (up to three weeks) (**Table 2.S2**). However, at three weeks post-TBI, we saw more epileptiform spikes in TBI mice (n=9) than in sham mice (n=5), suggesting an increase in excitability (**Table 2.S2**). Similarly, in another recording setup using simultaneous ECoG and multi-unit thalamic recordings, we observed that TBI mice have spontaneous epileptiform events that include synchronized thalamic bursting and increased normalized theta power, as early as one week and up to three weeks post-TBI (**Figure 2.S5**).

### **Anti-C1q antibody may have modest effects on chronic cortical states in mice with TBI**

To determine whether blocking C1q could rescue changes in cortical states, we treated mice with the anti-C1q antibody or isotype control for five weeks, starting 24 hours post-TBI, while maintaining ECoG recordings for up to 9-15 weeks post-TBI (**Figure 2.5A, Figure 2.S6**). While the ECoG spectral features were similar within the first week of anti-C1q antibody or control treatment (**Figure 2.5B-C, Figure 2.S6B**), analysis of the combined cohorts show that the anti-

C1q group trended toward reduced power across most frequency bands at three weeks (**Figure 2.5D-E, Figure 2.S6C**).

Notably, epileptiform activities were not affected by the anti-C1q antibody (**Table 2.S2**). Three weeks post-TBI, we saw no GTCSs and no differences in the frequency of epileptic events between control-treated and antibody-treated TBI mice (**Table 2.S2**).

## **Discussion**

In this study, we set out to understand the role of the C1q pathway in post-TBI secondary injury to the corticothalamic circuit in a mechanistically tractable and highly reproducible mouse model of cortical injury. This model allows us to identify factors such as therapeutic windows, inflammatory phenotypes, and degree of secondary damage, which have been postulated to be important for designing targeted approaches in the treatment of post-TBI outcomes (Simon et al., 2017).

Our study pioneers the use of electrophysiological approaches to study the entire somatosensory corticothalamic circuit after TBI. One powerful tool we employ is chronic ECoG recordings to study the progression of post-traumatic epileptogenesis and changes in cortical rhythms up to four months post TBI. Using electrophysiological approaches at the cellular and circuit levels, we show that TBI alters the synaptic properties of nRT neurons and is associated with increased C1q accumulation that might mediate pathological states in the corticothalamic circuit, including increased broadband activity.

### **The nRT as a locus of long-term, secondary impairments post-TBI**

We found two kinds of defects in the nRT: neuron loss, and alterations in synaptic properties. nRT neurons degenerated by three weeks after TBI, in agreement with previous observations from the human nRT (Ross et al., 1993), suggesting that even mild cortical injury can lead to neuronal loss in nRT. Potential causes for this neurodegeneration could be loss of cortical inputs causing excitotoxicity in nRT, which has been suggested to be a vulnerable brain region due to high density of axonal afferents from the cortex (Ross et al., 1993). We hypothesized that inflammation plays a major role in this process and that inhibiting inflammation would rescue these defects.

The loss of neurons in the nRT could explain some of the synaptic changes in this area. In particular, we found that three weeks post-TBI, the frequency of IPSCs was reduced in nRT neurons. In many microcircuits, reduced inhibition on GABAergic neurons results in a net increase

in inhibition. By contrast, loss of GABAergic inhibition in the nRT results in corticothalamic circuit hyperexcitability, and can even elicit epileptiform activity (Huntsman et al., 1999; Sohal and Huguenard, 2003). Indeed, intra-nRT GABAergic connections are important for coordinating inhibitory output to the excitatory thalamic nuclei and controlling oscillatory thalamic activity (Sohal et al., 2000), and their loss is deleterious to the corticothalamic circuit. We speculate that the death of GABAergic neurons in the nRT may contribute to reduced intra-nRT inhibition. This reduced inhibition could cause a loss of feed-forward GABAergic inhibition, which may contribute to increased seizure susceptibility, and increased likelihood of developing post-traumatic epileptic activities.

We also observed deficits in nRT EPSCs, in particular lower amplitude. This alteration is similar to the findings from a mouse model of epilepsy that lacks GluA4 AMPA receptors at the cortico-nRT glutamatergic synapse. This defect results in loss of feed-forward inhibition in the thalamus, and epileptic activities (Paz et al., 2011). We therefore propose that alterations to the nRT EPSCs also contribute to corticothalamic circuit hypersynchrony and seizures, but likely results from a loss of cortical glutamatergic inputs to the nRT after TBI, although loss of other afferents cannot be excluded.

Given that the changes we found in the corticothalamic circuit, and the nRT in particular, have been implicated in epileptic activities and cognitive deficits, our study pinpoints this circuit as a novel potential target for treating long-term TBI outcomes.

Unlike nRT neurons, cortical neurons, such as layer-5 pyramidal neurons and GABAergic fast-spiking interneurons, were not altered by mild TBI at chronic time points. These observations suggest the presence of homeostatic mechanisms that restore or reduce chronic hyperexcitability after TBI in the cortex. They also confirm that at least certain long-term outcomes of TBI must result from nRT dysfunction rather than simply from damage to the cortex. In this regard, it is interesting to see that while cortical neurons appear to have normal excitability and synaptic function at the chronic phase, the cortex shows increased broadband activity, particularly delta.



This observation is in agreement with previous magnetoencephalography studies in humans with mild TBI, EEG studies in humans with severe TBI, and EEG studies from rats with severe TBI, which observed increased delta activity at early time points post-TBI (Huang et al., 2009; Lee and Huang, 2014; Lu et al., 2011; Ronne-Engstrom and Winkler, 2006). In normal conditions, delta activity is associated with slow wave sleep, quiet wakefulness, and higher cognitive function (Church, 1975; Sachdev et al., 2015). In cases of injury, delta waves are associated with a white matter lesion (Ronne-Engstrom and Winkler, 2006).

Overall, our findings suggest that the major long-term impact of mild TBI is in the thalamic end of the cortico-thalamo-cortical loop.

### **C1q: good or bad? A question of timing**

We chose to test the importance of one specific inflammatory pathway, the classical complement pathway, using a pharmacological tool to block C1q in TBI mice. C1q has a well-documented role in normal brain function such as synaptic pruning during development (Stevens et al., 2007), as well as its involvement in several neurological diseases (Bellander et al., 2001; Hammad et al., 2018; Hong et al., 2016; Krukowski et al., 2018; Lui et al., 2016; Wyatt et al., 2017; You et al., 2007). In addition, we had observed that C1q expression was highly increased in the corticothalamic circuit for up to four months after TBI (**Figure 2.S2**).

Although our mild TBI mice did not develop chronic GTCSs to determine if blocking C1q had an anti-seizure effect, we did observe many other protective effects of the anti-C1q antibody, including reduced inflammation and neurodegeneration. Based on these observations and previous literature implicating differences between protective and harmful inflammatory cell types (Liddelow et al., 2017; Mills et al., 2000), we speculate that C1q plays both good and bad roles but at different stages of pathology. At the time of the injury, C1q plays a “beneficial” role, perhaps by aiding with the formation of the glial scar that limits the size of the injury within the primary site of the cortex (Lu et al., 2011; Wang et al., 2018). However, at the chronic phase, C1q increase

plays a maladaptive role in promoting chronic inflammation and secondary neurodegeneration in the nRT.

The cortex also exhibits an increase in C1q, but it does not appear to have a damaging role at this site, or may play a counterbalancing initial protective role since, unlike in the thalamus, the neuronal physiology is similar in the cortex of sham and TBI mice at chronic time points. Our findings suggest the existence of a time window during which the anti-C1q treatment might prevent secondary damage to the thalamus without impairing homeostatic recovery at the cortex.

In conclusion, our study pinpoints C1q as a potential disease modifier that could be targeted for treating devastating outcomes of TBI within a certain time window (in this study, beginning treatment 24 hours post-injury). C1q might also serve as a biomarker to help identify those individuals likely to develop long-term, secondary injuries. Our study also motivates further investigation of the molecular mechanism by which C1q causes neuronal death in nRT, beyond its well-known role in synaptic pruning in health and disease. In addition, by showing that the thalamus is chronically affected by TBI, we identify a potential cause for many TBI-related disabilities such as altered sensory processing, sleep disruption, and epilepsy, and a novel target for post-TBI treatments.

## **Materials & Methods**

### **Animals**

We performed all experiments per protocols approved by the Institutional Animal Care and Use Committee at the University of California, San Francisco and Gladstone Institutes. Precautions were taken to minimize stress and the number of animals used in each set of experiments. Mice were separately housed after surgical implants. Adult (P30-P180) male CD1 mice were used for most experiments. Adult male Thy1-GCaMP6f mice (Tg(Thy1-GCaMP6f)GP5.17Dkim ISMR\_JAX: 025393; C57BL/6 congenic) and C1q null mice (C1qa<sup>tm1Mjw</sup>, ISMR\_APB: 1494; C57BL/6 congenic) were used for specific experiments.

### **Controlled cortical impact**

We anesthetized mice with 2-5% isoflurane and placed them in a stereotaxic frame. We performed a 3 mm craniotomy over the right somatosensory cortex (S1) centered at -1 mm posterior from Bregma, +3 mm lateral from the midline. TBI was performed with a CCI device (Impact One Stereotaxic Impactor for CCI, Leica Microsystems) equipped with a metal piston using the following parameters: 3 mm tip diameter, 15° angle, depth 0.8 mm from the dura, velocity 3 m/s, and dwell time 100 ms. Sham animals received identical anesthesia and craniotomy, but the injury was not delivered.

### **Immunostaining and microscopy**

We anesthetized mice with a lethal dose of Fatal-Plus and perfused with 4% paraformaldehyde in 1X PBS. Serial coronal sections (30 µm thick) were cut on a Leica SM2000R sliding microtome. Sections were incubated with antibodies directed against C1q (1:700, rabbit, Abcam, ab182451, AB\_2732849), GFAP (1:1000, chicken, Abcam, ab4674, AB\_304558), GFP (1:500, chicken, Aves Labs, AB\_10000240), Iba1 (1:500, rabbit, Wako, 019-19741, AB\_839504), and NeuN (1:500, mouse, Millipore, MAB377, AB\_2298772) overnight at 4°C. After wash, we incubated sections with Alexa Fluor-conjugated secondary antibodies (1:300, Thermo Fisher Scientific, A-11029) for

two hours at room temperature. We mounted sections in an antifade medium (Vectashield) and imaged using a Bioevo BZ-9000 Keyence microscope at 10-20x. Confocal imaging was performed using a confocal laser scanning microscope (LSM880, Zeiss) equipped with a Plan Aplanachromat 10x/0.45 NA air or 63x/1.4 NA oil immersion objective lens. A multi-line Argon laser was used for 488 nm excitation of AlexaFluor488 and a HeNe laser was used for 561 nm excitation of AlexaFluor594.

### **Immunostaining of human tissue**

Formalin-fixed, paraffin-embedded tissue was sectioned at 6  $\mu\text{m}$  and mounted on organosilane-coated slides (SIGMA, St. Louis, MO). Representative sections of specimens were processed for hematoxylin/eosin, as well as for immunocytochemistry. Immunocytochemistry for C1q (1:200, rabbit polyclonal; DAKO, Denmark), was carried out on a paraffin-embedded tissue as previously described (Aronica et al., 2007; Schiering et al., 2014). Sections were incubated for one hour at room temperature followed by incubation at 4°C overnight with primary antibodies. Single-labeled immunocytochemistry was performed using Powervision method and 3,3'-diaminobenzidine as chromogen. Sections were counterstained with hematoxylin. An extensive neuropathological protocol was used (based upon the recommendations of the Brain-Net Europe consortium; *Acta Neuropathologica* 115(5):497-507 ·2008), including markers such as pTau (AT8),  $\beta$ -Amyloid, pTDP-43 and alpha-synuclein.

### **Slice preparation for electrophysiology**

We euthanized mice with 4% isoflurane, perfused with ice-cold sucrose cutting solution containing 234 mM sucrose, 11 mM glucose, 10 mM  $\text{MgSO}_4$ , 2.5 mM KCl, 1.25 mM  $\text{NaH}_2\text{PO}_4$ , 0.5 mM  $\text{CaCl}_2$ , and 26 mM  $\text{NaHCO}_3$ , equilibrated with 95%  $\text{O}_2$  and 5%  $\text{CO}_2$ , pH 7.4, and decapitated. We prepared 250- $\mu\text{m}$  thick horizontal slices for thalamic recordings, and coronal slices for neocortical recordings with a Leica VT1200 microtome (Leica Microsystems). Slices were incubated at 32°C for one hour and then at 24-26°C in artificial cerebrospinal fluid (ACSF) containing 126 mM NaCl, 10 mM glucose, 2.5 mM KCl, 2 mM  $\text{CaCl}_2$ , 1.25 mM  $\text{NaH}_2\text{PO}_4$ , 1 mM  $\text{MgSO}_4$ , and 26 mM  $\text{NaHCO}_3$ ,

and equilibrated with 95% O<sub>2</sub> and 5% CO<sub>2</sub>, pH 7.4. Thalamic slice preparations were performed as described (Clemente-Perez et al., 2017; Paz et al., 2011; Ritter-Makinson et al., 2019).

### **Patch-clamp electrophysiology**

Recordings were performed as previously described (Clemente-Perez et al., 2017; Paz et al., 2011; Ritter-Makinson et al., 2019). We visually identified S1, nRT, and VB neurons by differential contrast optics with an Olympus microscope and an infrared video camera. Recording electrodes made of borosilicate glass had a resistance of 2.5-4 MΩ when filled with intracellular solution. Access resistance was monitored in all the recordings, and cells were included for analysis only if the access resistance was <25 MΩ. Intrinsic and bursting properties and spontaneous excitatory postsynaptic currents (EPSCs) were recorded in the presence of picrotoxin (50 μM, Sigma) and the internal solution contained 120 mM potassium gluconate, 11 mM EGTA, 11 mM KCl, 10 mM HEPES, 1 mM CaCl<sub>2</sub>, and 1 mM MgCl<sub>2</sub>, pH adjusted to 7.4 with KOH (290 mOsm). We corrected the potentials for -15 mV liquid junction potential.

Spontaneous inhibitory postsynaptic currents (IPSCs) were recorded in the presence of kynurenic acid (2 mM, Sigma), and the internal solution contained 135 mM CsCl, 10 mM EGTA, 10 mM HEPES, 5 mM Qx-314 (lidocaine N-ethyl bromide), and 2 mM MgCl<sub>2</sub>, pH adjusted to 7.3 with CsOH (290 mOsm).

### **Surgical implantation of devices for simultaneous recording of ECoG and multi-unit activity (MUA)**

The devices for simultaneous ECoG, MUA recordings, and optical manipulations in freely behaving mice were all custom made in the Paz lab as described in (Clemente-Perez et al., 2017; Ritter-Makinson et al., 2019). In general, recordings were optimized for assessment of somatosensory subnetworks (S1, somatosensory VB thalamus, and somatosensory nRT).

We implanted cortical screws bilaterally over S1 (contralateral to injury: -0.5 mm posterior from Bregma, -3.25 mm lateral; ipsilateral: +1.0-1.4 mm anterior from Bregma, +2.5-3.0 mm lateral), centrally over PFC (+0.5 mm anterior from Bregma, 0 mm lateral), and in the right hemisphere

over V1 (-2.9 mm posterior from Bregma, +2.7 mm lateral). For MUA recordings in VB, we implanted electrodes at -1.65 mm posterior from Bregma, +1.75 mm lateral, with the tips of the optical fiber at 3.0 mm and two electrodes at 3.25 mm and 3.5 mm ventral to the cortical surface. For MUA recordings in nRT, we implanted electrodes at -1.4 mm posterior from Bregma, +2.1 mm lateral, with the tips of the optical fiber at 2.7 mm and two electrodes at 2.9 mm, and 3.0 mm ventral to the cortical surface, respectively.

### **In vivo electrophysiology and behavior**

Non-chronic MUA electrophysiological recordings in freely behaving mice were performed as described using custom-made optrode devices (Clemente-Perez et al., 2017; Ritter-Makinson et al., 2019). ECoG and thalamic LFP/MU signals were recorded using RZ5 (TDT) and sampled at 1221 Hz, with thalamic MUA signals sampled at 24 kHz. A video camera that was synchronized to the signal acquisition was used to continuously monitor the animals. We briefly anesthetized animals with 2% isoflurane at the start of each recording to connect for recording. Each recording trial lasted 15-60 min. To control for circadian rhythms, we housed our animals using a regular light/dark cycle, and performed recordings between roughly 9:00 am and 6:00 pm. All the recordings were performed during wakefulness. We validated the location of the optrodes by histology after euthanasia in mice that did not experience sudden death and whose brains we were able to recover and process.

### **Surgical implantation of devices for chronic ECoG recordings**

The wireless telemetry devices we used for chronic ECoG recordings were purchased from Data Sciences International (DSI). After performing controlled cortical impact surgery, we implanted cortical screws bilaterally over S1 as described above. The battery/transmitter device was placed under the skin over the right shoulder. We began recording mice as soon as they recovered from the surgery. Mice were singly housed in their home cages, which were placed over receivers that sent signals to an acquisition computer. ECoG signals were continuously recorded from up to eight mice simultaneously using Ponemah software (DSI), and sampled at 500 Hz.

## **Statistical analyses**

All numerical values are given as means and error bars are standard error of the mean (SEM) unless stated otherwise. Parametric and non-parametric tests were chosen as appropriate and were reported in figure legends. Data analysis was performed with MATLAB (SCR\_001622), GraphPad Prism 7/8 (SCR\_002798), ImageJ (SCR\_003070), Ponemah/NeuroScore (SCR\_017107), pClamp (SCR\_011323), and Spike2 (SCR\_000903).

## **Image analysis and cell quantification**

We selected regions of interest (ROIs) for S1, nRT, and VB from 10x Keyence microscope images opened in ImageJ (SCR\_003070). To ensure that each ROI covered the same area on the ipsilateral and contralateral sides of the injury site, the first ROIs were duplicated and repositioned over the opposite hemisphere. The image was then converted to 8-bit. The upper threshold was adjusted to the maximum value of 255, and the lower threshold was increased from 0 until the pixel appearance most closely matched the fluorescence staining from the original image. We used the same threshold boundaries for all sections with the same stain. An integrated density ratio was calculated for each brain region by dividing the ipsilateral integrated pixel density by the contralateral integrated pixel density. The integrated density ratios from three sections per animal were averaged to get a single average ratio per brain area for each animal.

nRT cell counts were performed on sections stained with NeuN. The nRT was outlined in ImageJ (SCR\_003070) and we performed a manual cell count of neuronal cell bodies using the manual counter plugin.

## **Analysis of electrophysiological properties**

The input resistance ( $R_{in}$ ) and membrane time constant ( $\tau_m$ ) were measured from the membrane hyperpolarizations in response to low intensity current steps (-20 to -60 pA). The reported rheobase averages and SEMs were calculated based on the current which first caused at least one action potential during the stimulus per recording. All data from Table 2.S1 were analyzed

using a Mann-Whitney test with  $\alpha = 0.05$  (\* $p < 0.05$ , \*\* $p < 0.01$ , \*\*\* $p < 0.001$ , \*\*\*\* $p < 0.0001$ ), using GraphPad Prism 7 (SCR\_002798).

Cumulative probability distributions were generated in MATLAB (SCR\_001622) from 11 sham nRT neurons and 9 TBI neurons, using 200 randomly selected events from each cell.

### **ECoG spectral and seizure analysis**

Spectrograms were generated for frequencies between 1 and 50 Hz using the short-time Fourier transform with 0.5 s Hamming windows and 98% overlap between segments. Spectrograms and cumulative distribution functions were generated in MATLAB. ECoG frequency bands were divided as follows: delta = 1-4 Hz, theta = 5-8 Hz, alpha = 9-12 Hz, sigma = 13-15 Hz, beta = 16-30 Hz, gamma = 31-50 Hz. Fast Fourier transforms were generated in MATLAB. Epileptic activities were analyzed manually within the time windows specified for each experiment. Epileptic discharges (EDs) were defined as clusters of interictal spiking events lasting five seconds or longer. Spike-and-wave discharges (SWDs) were defined as symmetrical 6-8 Hz spiking events lasting two seconds or longer. Generalized tonic-clonic seizures (GTCSs) were defined as spiking events lasting at least 30 seconds and present in both ECoG channels. Abnormal events were defined as any irregular spiking events that did not fit into any of the other categories.

### **Anti-C1q antibody**

The anti-C1q is antibody ANX-M1, and the control is a mouse isotype IgG1 antibody (Annexon Biosciences). All mice were treated at a concentration of 100 mg/kg, and previous studies have reported no toxicity in rodents. The antibody has been characterized as described in (Hong et al., 2016; Lansita et al., 2017; McGonigal et al., 2016). Mice were first treated 24 hours post-TBI, and continued receiving treatment every three days (four days post-TBI, seven days post-TBI, etc.) for three weeks, or until the experimental end point as noted in Figure 2.5.

### **Treatment paradigm and tissue lysis**

For the PK study, mice underwent sham or TBI surgery on Day 0, and were treated intraperitoneally with 100 mg/kg of anti-C1q antibody (M1) or isotype control on Day 1 and 4. Mice



were perfused with PBS on Day 5. Plasma and brains (ipsi- and contra- lateral sides) were collected and flash frozen. Brains (without olfactory bulb and cerebellum) were lysed in 1:10 w/v BupH™ Tris Buffered Saline (Thermo Scientific 28379) + protease inhibitor cocktail (Thermo Scientific A32963) by homogenizing with 7 mm steel bead in Qiagen TissueLyser for two minutes at 30 Hz. Lysates were then spun at 17,000 x g for 20 minutes. Supernatants were used for ELISA assays.

### **Pharmacokinetic (PK) and pharmacodynamic (PD) ELISA assays**

The levels of free anti-C1q drug M1 (PK), free C1q, total C1q, C1s and Albumin were measured using sandwich ELISAs. Black 96 well plates (Nunc 437111) were coated with 75 uL of respective capture protein/antibody: human C1q protein for PK (complement Tech), mouse monoclonal anti-C1q (Abcam, ab71940) for C1q-free, rabbit polyclonal anti-C1q (Dako, A0136) and rabbit polyclonal anti mouse C1s (LSBio, C483829) for C1s, in bicarbonate buffer (pH 9.4) overnight at 4°C. Next day, the plates were washed with dPBS pH 7.4 (Dulbecco's phosphate-buffered saline) and blocked with dPBS containing 3% bovine serum albumin (BSA). Standard curves were prepared with purified proteins in assay buffer (dPBS containing 0.3% BSA and 0.1% Tween20). Samples were prepared in the assay buffer at appropriate dilutions. The blocking buffer was removed from the plate by tapping. Standards and samples were added at 75 uL per well in duplicates and incubated with shaking at 300 rpm at room temperature for one hour for PK measurements. For complement assays, samples were incubated overnight at 4°C followed by 37°C for 30 minutes and then room temperature for one hour. Plates were then washed three times with dPBS containing 0.05% Tween20 and 75 uL of alkaline-phosphatase conjugated secondary antibodies (goat anti-mouse IgG for PK, M1 for C1q free, rabbit polyclonal anti-C1q for C1q total, rabbit polyclonal anti-C1s for C1s) were added to all wells. Plates were incubated at room temperature with shaking for one hour, washed three times with dPBS containing 0.05% Tween20 and developed using 75 uL of alkaline phosphatase substrate (Life Technologies, T2214). After 20 minutes at room temperature, plates were read using a luminometer. Albumin

assay was done using a matched antibody pair from Abcam (ab210890), followed by Avidin-AP secondary antibody for detection. Standards were fit using a 4PL logistic fit and concentration of unknowns determined. Analyte levels were corrected for dilution factors.

## Figures

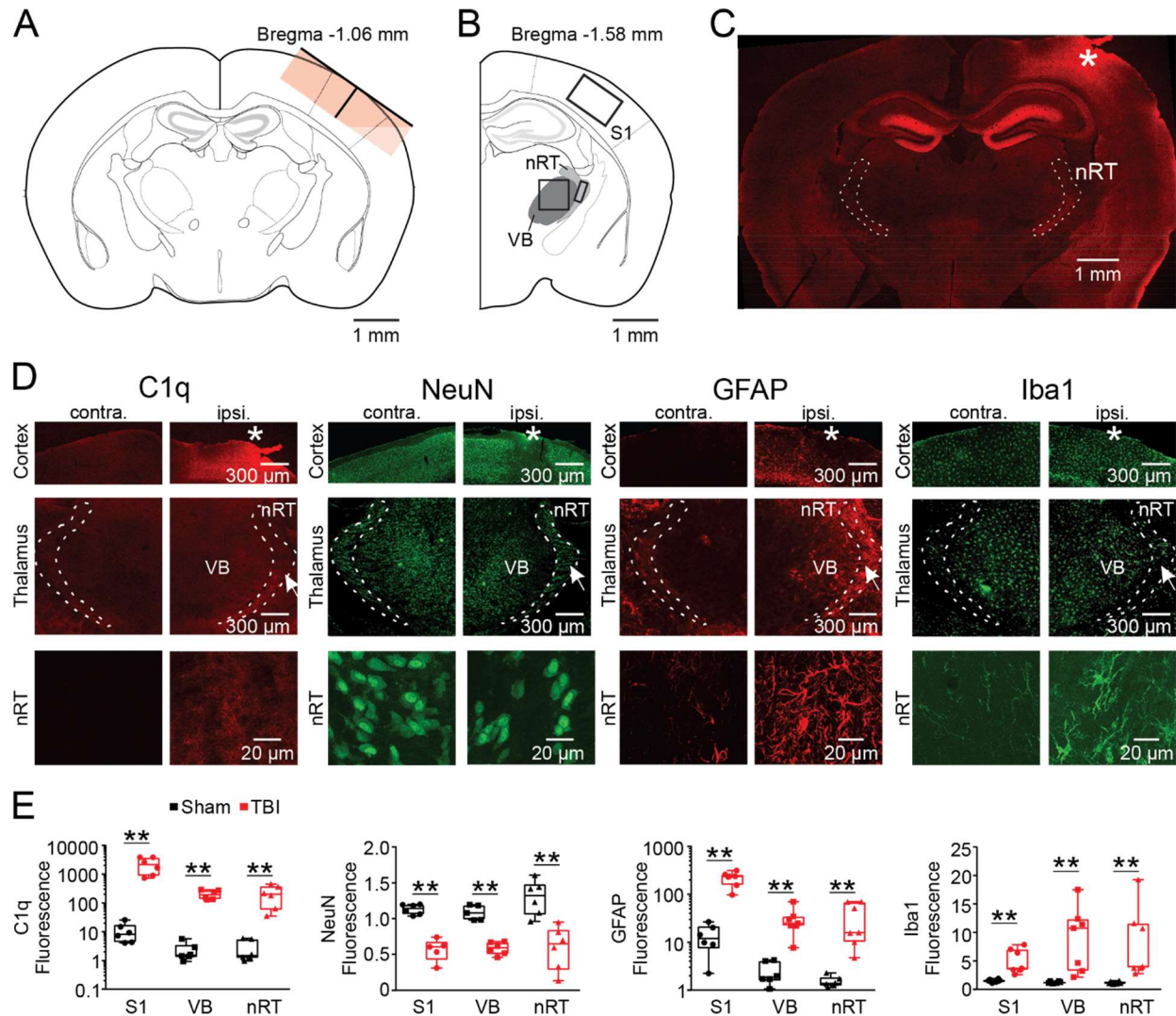


**Figure 2.1. The injured cortex and functionally connected thalamus show chronic inflammation and neuron loss three weeks after TBI.**

A, B) Schematic of a mouse brain coronal section showing the site and depth of the controlled cortical impact (A) and the location of the S1 cortex and nRT and VB thalamic regions (B). The impactor has a diameter of 3 mm and the impact was delivered at a depth of 0.8 mm to the right somatosensory cortex.

C) Representative coronal brain section from a TBI mouse stained for C1q. C1q expression in the hippocampus is typical of physiological conditions.

D) Close-up images of S1 (top), VB and nRT (middle), and confocal images of nRT (bottom) stained for C1q, neuronal marker NeuN, GFAP, a marker for astrocytes, and Iba1, a marker for microglia/macrophages. Injury site in the right S1 cortex is marked by an asterisk. Arrow in nRT indicates location of confocal image. Scale bars, 300  $\mu$ m (top/middle) and 20  $\mu$ m (bottom).

E) Quantification of fluorescence ratios between ipsilateral and contralateral regions in sham and TBI mice.

Data represent all points from min to max, with a Mann-Whitney test and  $\alpha = 0.05$  (\* $p < 0.05$ , \*\* $p < 0.01$ ). Analysis includes between five and seven mice per group ( $n =$  three sections per mouse, one image per region).

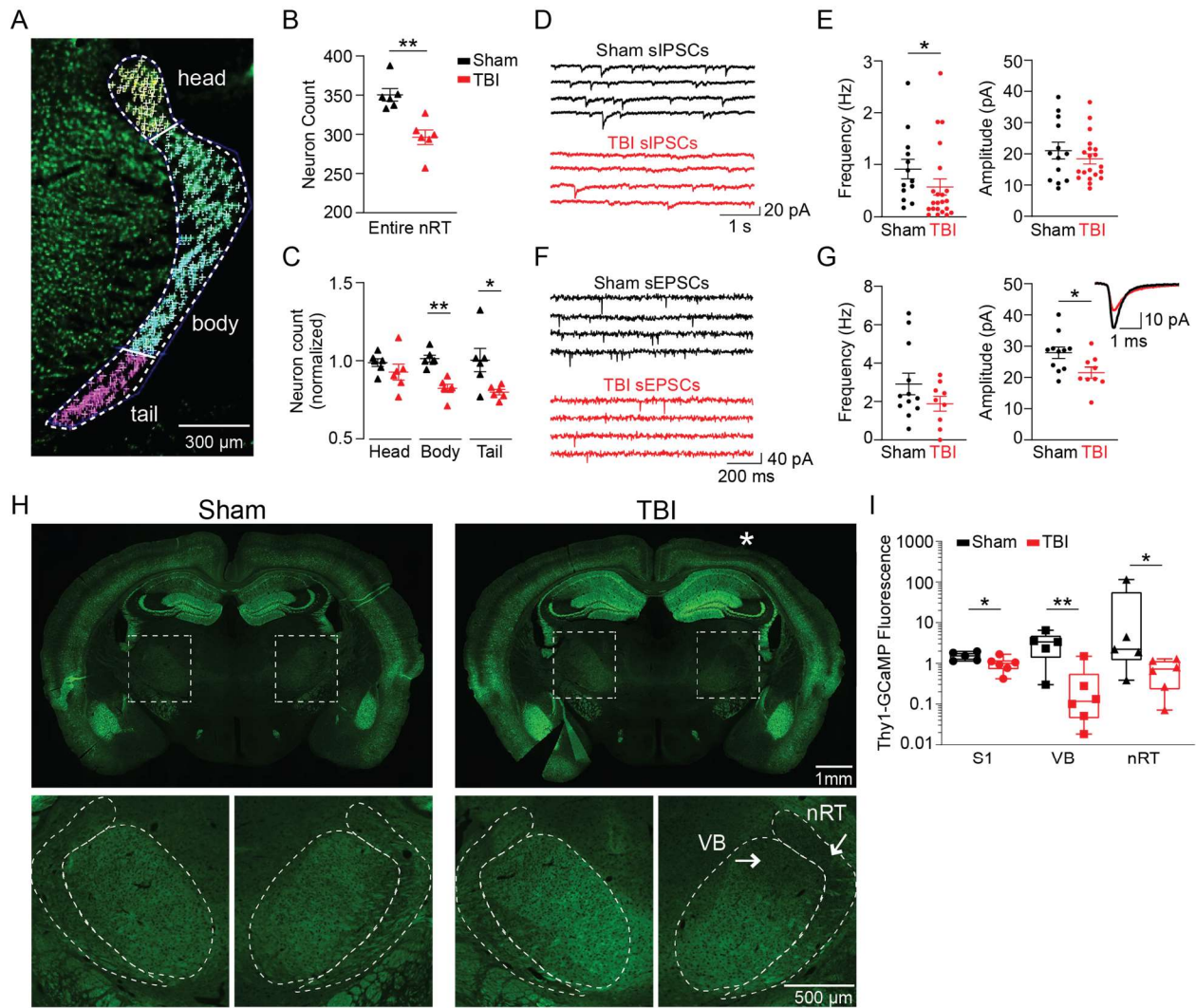


**Figure 2.2. The nRT ipsilateral to the injured cortex shows neuron loss and altered IPSC and EPSC properties three weeks after TBI.**

A-C) High-magnification coronal image of the nRT showing divisions into “head”, “body”, and “tail” (Clemente-Perez et al., 2017), and quantification of neuron counts across the entire ipsilateral nRT (B) or per subdivision, normalized to the median value from the sham group (C). Neuron count data represent mean  $\pm$  SEM, with a Mann-Whitney test and  $\alpha = 0.05$  (\* $p < 0.05$ , \*\* $p < 0.01$ ). Analysis includes six mice per group ( $n =$  three sections per mouse, averaged). D, E) Spontaneous IPSC recordings (D) from representative nRT neurons in sham and TBI mice, and frequency and amplitude distributions (E) in 13 posterior nRT neurons from four sham mice and 22 posterior nRT neurons from six TBI mice. IPSC data represent mean  $\pm$  SEM analyzed with a Mann-Whitney test and  $\alpha = 0.05$  (\* $p < 0.05$ ). F, G) Spontaneous EPSC recordings (F) from representative nRT neurons in sham and TBI mice, and frequency and amplitude distributions (G) in 11 posterior nRT neurons from six sham mice and nine posterior nRT neurons from seven TBI mice. Inset shows averaged EPSC traces from single nRT neurons from sham and TBI mice, plotted on the same scale. EPSC data represent mean  $\pm$  SEM analyzed with a Mann-Whitney test and  $\alpha = 0.05$  (\* $p < 0.05$ ).

H) Representative images of coronal brain sections from Thy1-GCaMP6f mice with sham surgery (left) and TBI (right) (injury site marked by asterisk). Bottom panels show projection terminals from the cortex to VB and nRT. Scale bars, 1 mm (top) and 500  $\mu$ m (bottom). Reduction in projection terminals from the cortex to VB and nRT (marked by arrows) were observed in n = six TBI mice.

I) Quantification of Thy1-GCaMP fluorescence ratios between ipsilateral and contralateral regions in sham and TBI mice.

Data represent all points from min to max, with a Mann-Whitney test and  $\alpha = 0.05$  (\*p < 0.05, \*\*p < 0.01). Analysis includes five sham mice and six TBI mice (n = three sections per mouse, one image per region).

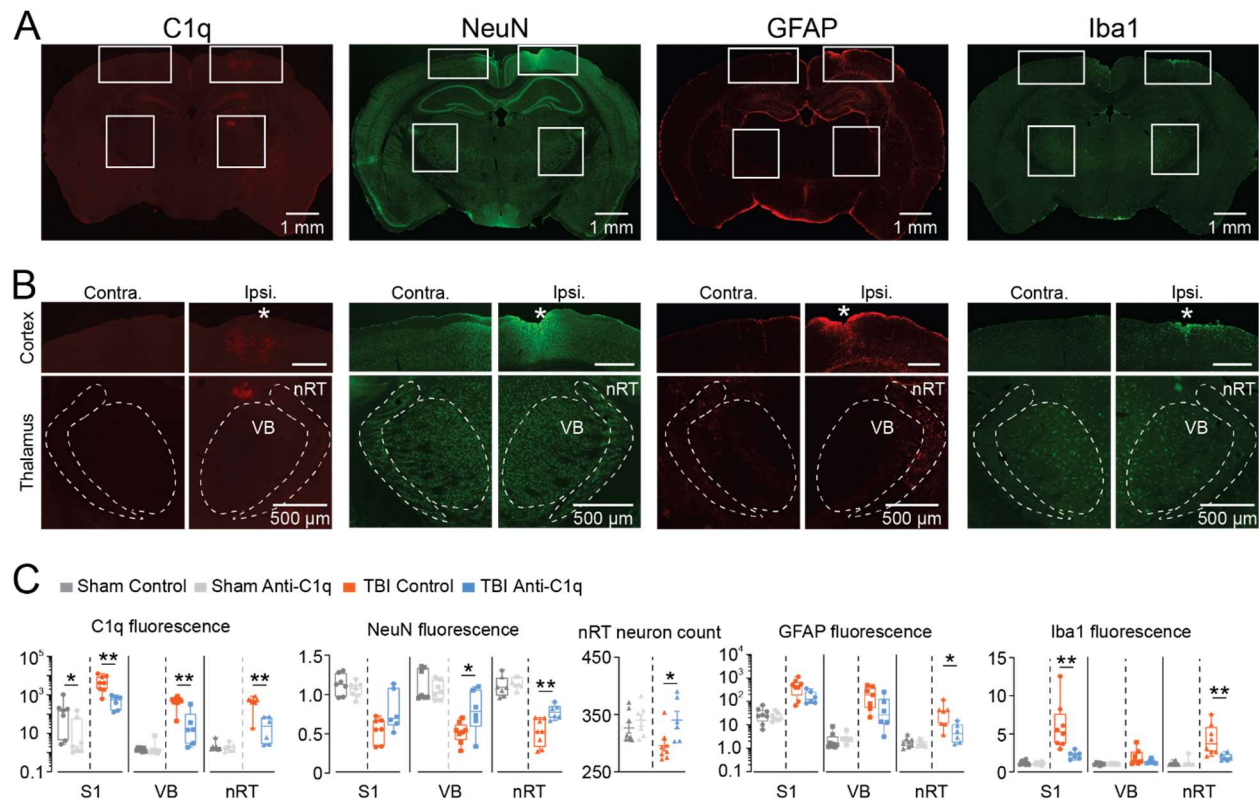


**Figure 2.3. Anti-C1q antibody reduces chronic inflammation and neuron loss three weeks after TBI.**

A, B) Representative coronal brain sections (A) and close-ups (B) of S1 (top), VB and nRT (bottom) from TBI mice treated with anti-C1q antibody and stained for C1q, NeuN, GFAP, and Iba1. Injury site in the right S1 cortex is marked by an asterisk. Scale bars, 1 mm (A), 500  $\mu$ m (B).

C) Quantification of nRT neuron counts and fluorescence ratios between ipsilateral and contralateral regions in control and antibody-treated sham and TBI mice.

Data represent all points from min to max, with a Mann-Whitney test and  $\alpha = 0.05$  (\* $p < 0.05$ , \*\* $p < 0.01$ ). Analysis includes between six and eight mice per group ( $n =$  three sections per mouse, one image per region).

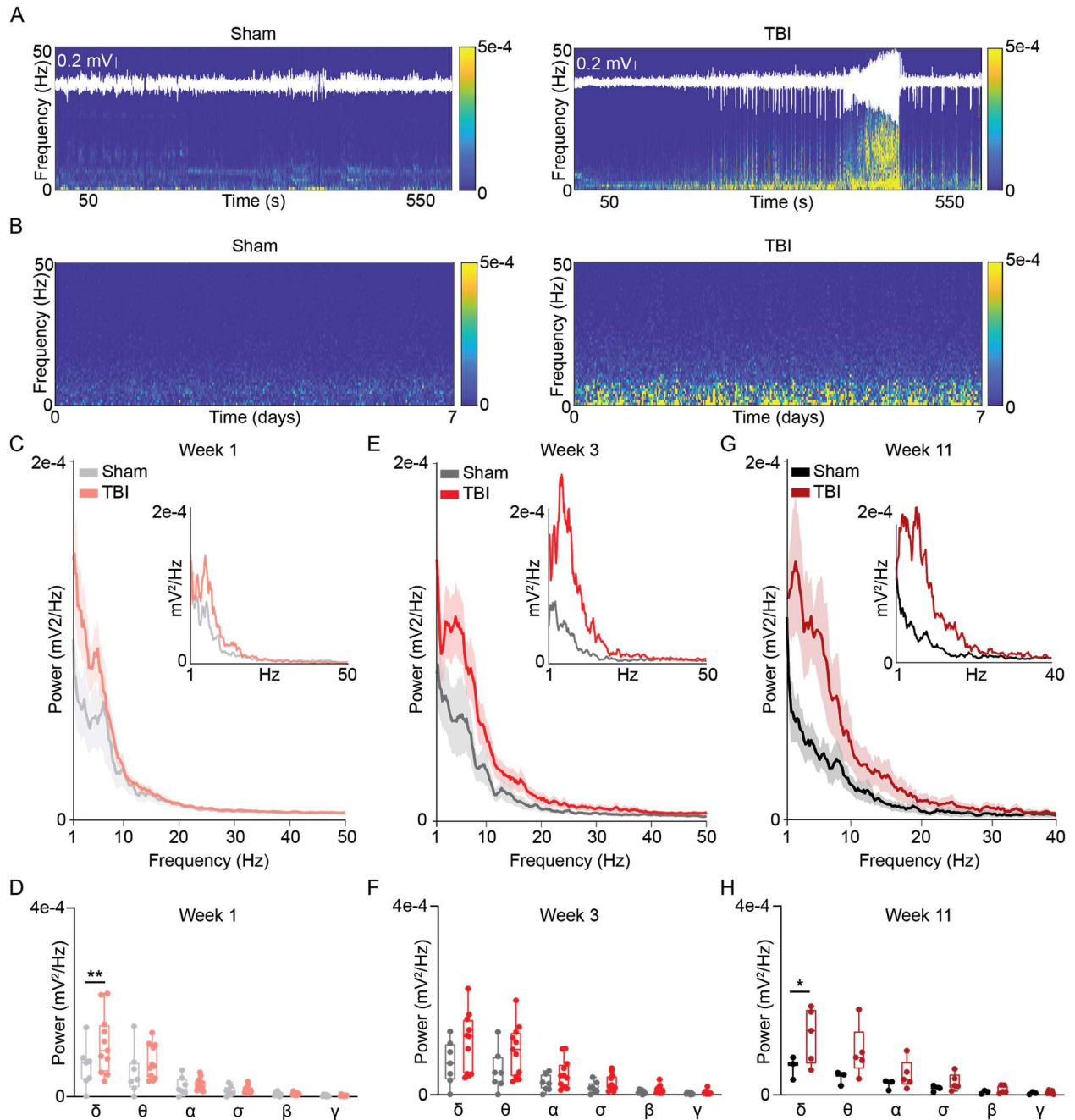


**Figure 2.4. Chronically recorded TBI mice show altered power across different ECoG frequency bands.**

A) Example 10-minute spectrograms from a sham mouse (left) and TBI mouse (right) taken from the same time point within the first 24 hours of TBI, overlaid with ECoG traces from ipsilateral S1. The TBI spectrogram shows an example of an electrographic seizure, while the sham spectrogram shows normal ECoG activity. Color bar represents power ( $\text{mV}^2/\text{Hz}$ ).

B) Example seven-day spectrograms from a sham mouse (left) and TBI mouse (right) showing power across different frequency bands two to three weeks post-TBI. Power bands are sampled every 30 minutes. Color bar represents power ( $\text{mV}^2/\text{Hz}$ ).

C) Power spectral density of ECoG activity from sham and TBI cohorts averaged across the first week post-TBI. Inset shows example power spectral density plots from a representative sham and TBI mouse. See methods for details.

D) Two-way ANOVAs of average power across frequency bands for the first week post-TBI. Each dot represents power for one mouse.

E) Same as C) but at three weeks post-TBI.

F) Same as D) but at three weeks post-TBI.

G) Same as C) but at 11 weeks post-TBI.

H) Same as D) but at 11 weeks post-TBI.

Data represent all mice recorded, analyzed with a two-way ANOVA (\* $p < 0.05$ , \*\* $p < 0.01$ ), even if they died or if the battery ran out before the experimental endpoint.  $n =$  eight sham mice, 16 TBI mice. One mouse died within two days post-TBI. The remaining mice were recorded for the first week post-TBI, then recorded for alternating weeks until eleven weeks post-TBI. Delta = 1-4 Hz, theta = 5-8 Hz, alpha = 9-12 Hz, sigma = 13-15 Hz, beta = 16-30 Hz, gamma = 31-50 Hz.



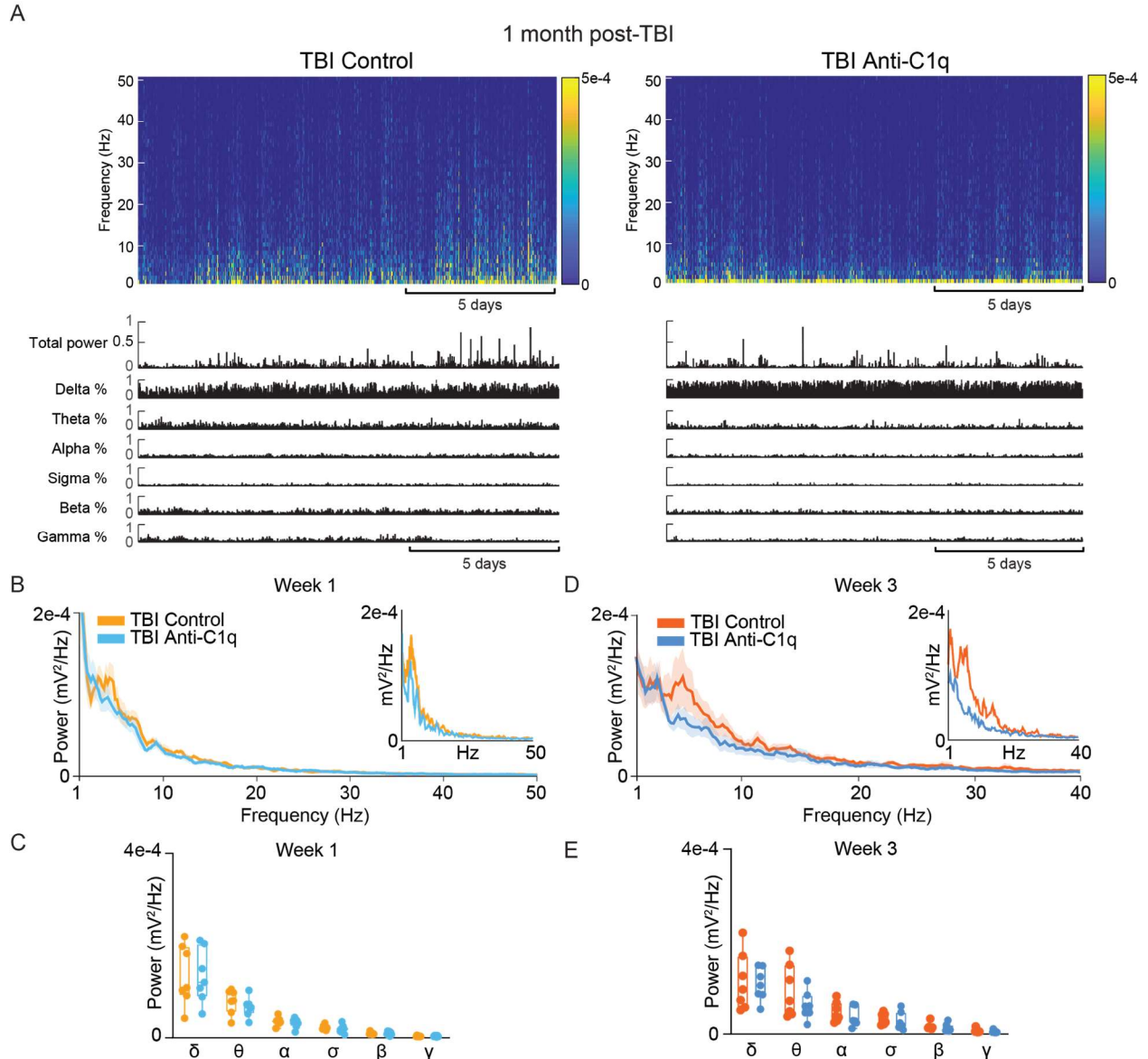


**Figure 2.5. Anti-C1q antibody has modest effects on ECoG spectral features in mice with TBI.**

A) Example spectrograms (top) and histograms (bottom) from a control-treated mouse (left) and antibody-treated mouse (right) showing power across different frequency bands one month post-TBI. Power bands are sampled every 30 minutes. Color bar represents power (mV<sup>2</sup>/Hz).

B) Power spectral density of ECoG activity from control-treated and antibody-treated TBI cohorts averaged across the first week post-TBI. Inset shows example power spectral density plots from a representative control-treated TBI mouse and an antibody-treated TBI mouse. See methods for details.

C) Two-way ANOVAs of average power across frequency bands for the first week post-TBI. Each dot represents power for one mouse.

D) Same as B) but at three weeks post-TBI.

E) Same as C) but at three weeks post-TBI.

Data represent all mice recorded, analyzed with a two-way ANOVA, even if they died before treatment ended. n = seven control-treated mice, seven antibody-treated mice. Delta = 1-4 Hz, theta = 5-8 Hz, alpha = 9-12 Hz, sigma = 13-15 Hz, beta = 16-30 Hz, gamma = 31-50 Hz.

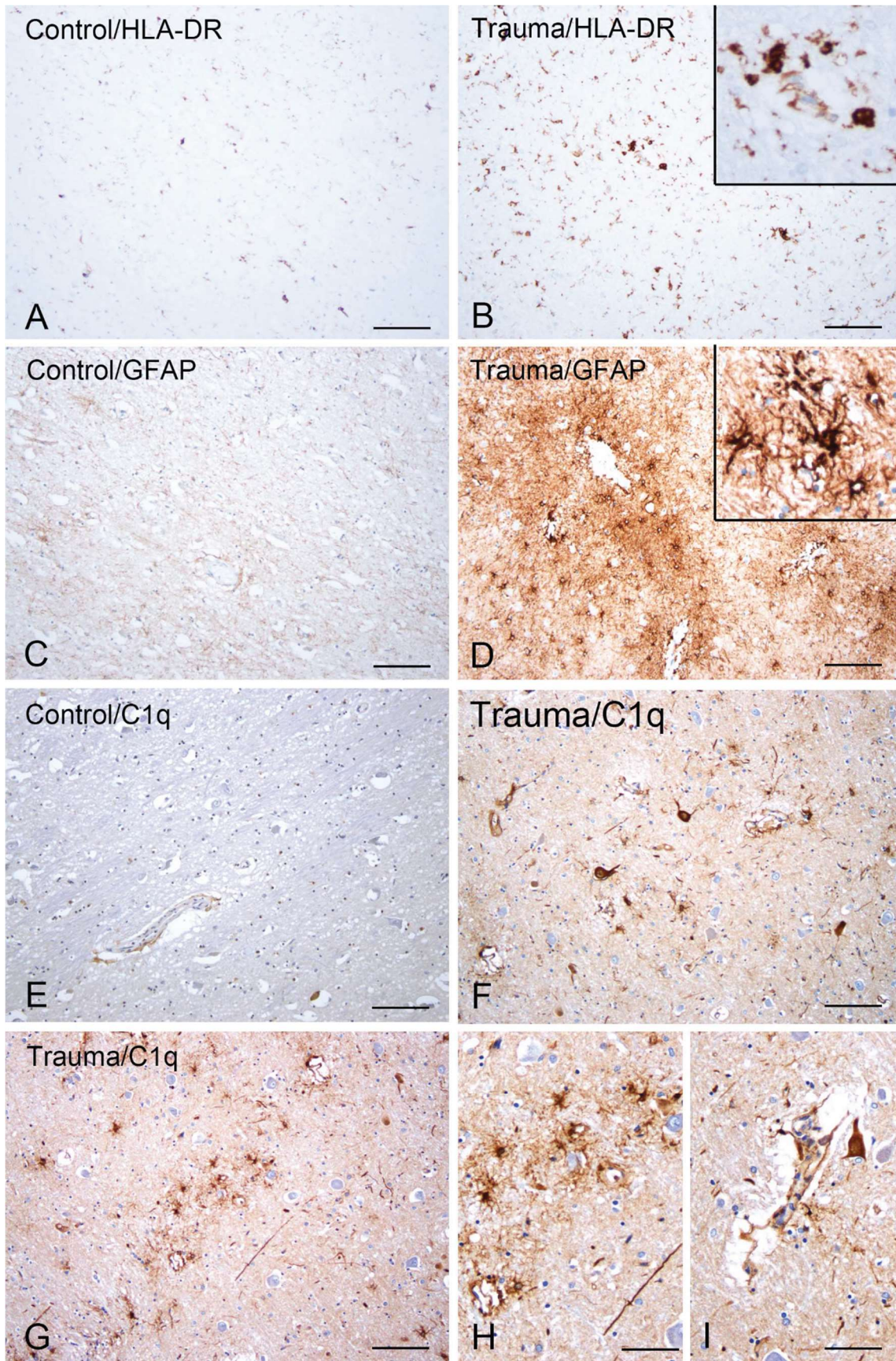


**Figure 2.S1. Postmortem brain tissue from a patient with TBI shows chronic inflammation eight days after TBI.**

A) Postmortem brain tissue from one control patient stained for HLA-DR, a marker for a MHC class II cell surface receptor that is expressed in microglia and macrophages. Case information: male, age 78. Scale bar, 1 cm.

B) Postmortem brain tissue from one TBI patient stained for HLA-DR. Case information: male, age 79; fall accident, Injury Severity (GCS): moderate, CT: cerebral edema; no epilepsy (post-TBI: eight days); no history of neurological diseases and without evidence of cognitive decline, based on the last clinical evaluation; no evidence of primary neurodegenerative pathology, evidence of trauma-induced diffuse axonal damage. Scale bar, 1 cm.

C) Same as (A) but stained for GFAP. Scale bar, 1 cm.

D) Same as (B) but stained for GFAP. Scale bar, 1 cm.

E) Same as (A) but stained for C1q. Scale bar, 1 cm.

F-I) Same as (B) but stained for C1q. Scale bars, 1 cm (F-G) and 40  $\mu$ m (H-I).

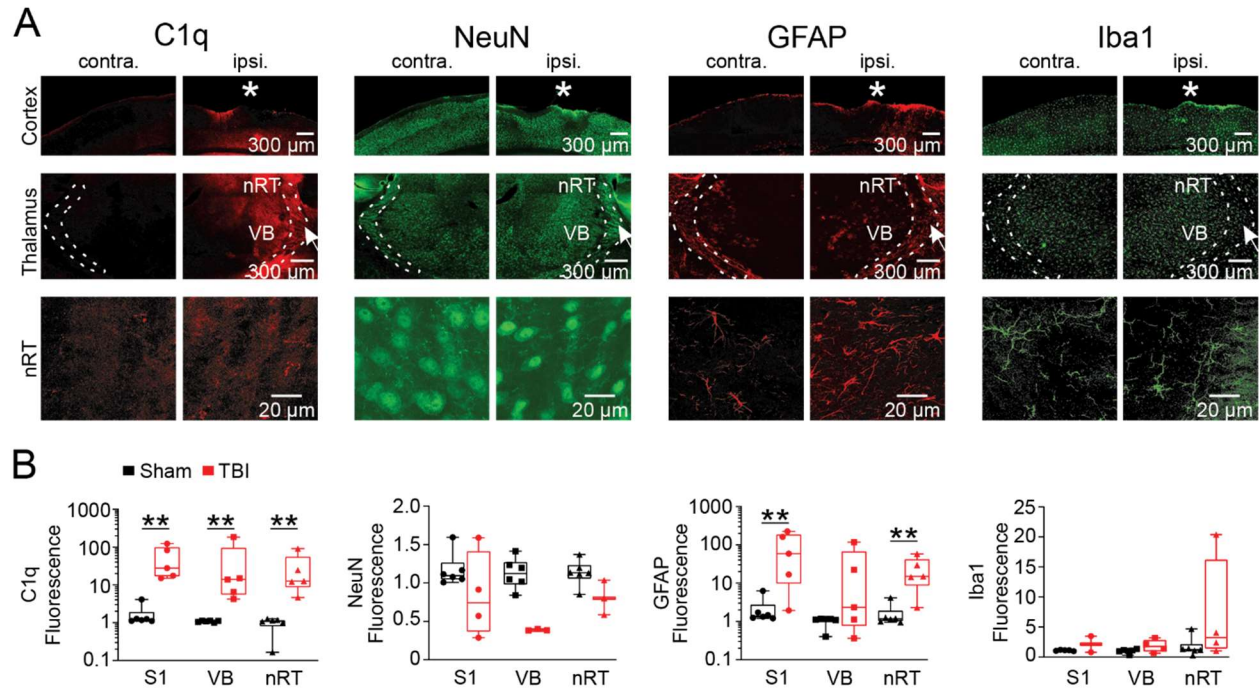


**Figure 2.S2. The injured cortex and functionally connected thalamus show chronic inflammation and neuron loss four months after TBI.**

A) Close-up images of S1 (top), VB and nRT (middle), and confocal images of nRT (bottom), stained for C1q, NeuN, GFAP, and Iba1. Injury site in the right S1 cortex is marked by an asterisk. Arrow in nRT indicates location of confocal image. Scale bars, 300  $\mu\text{m}$  (top/middle) and 20  $\mu\text{m}$  (bottom).

B) Quantification of fluorescence ratios between ipsilateral and contralateral regions in sham and TBI mice.

Data represent all points from min to max, with a Mann-Whitney test and  $\alpha = 0.05$  (\* $p < 0.05$ , \*\* $p < 0.01$ ). Analysis includes between four and six mice per group (n = one to three sections per mouse, one image per region).

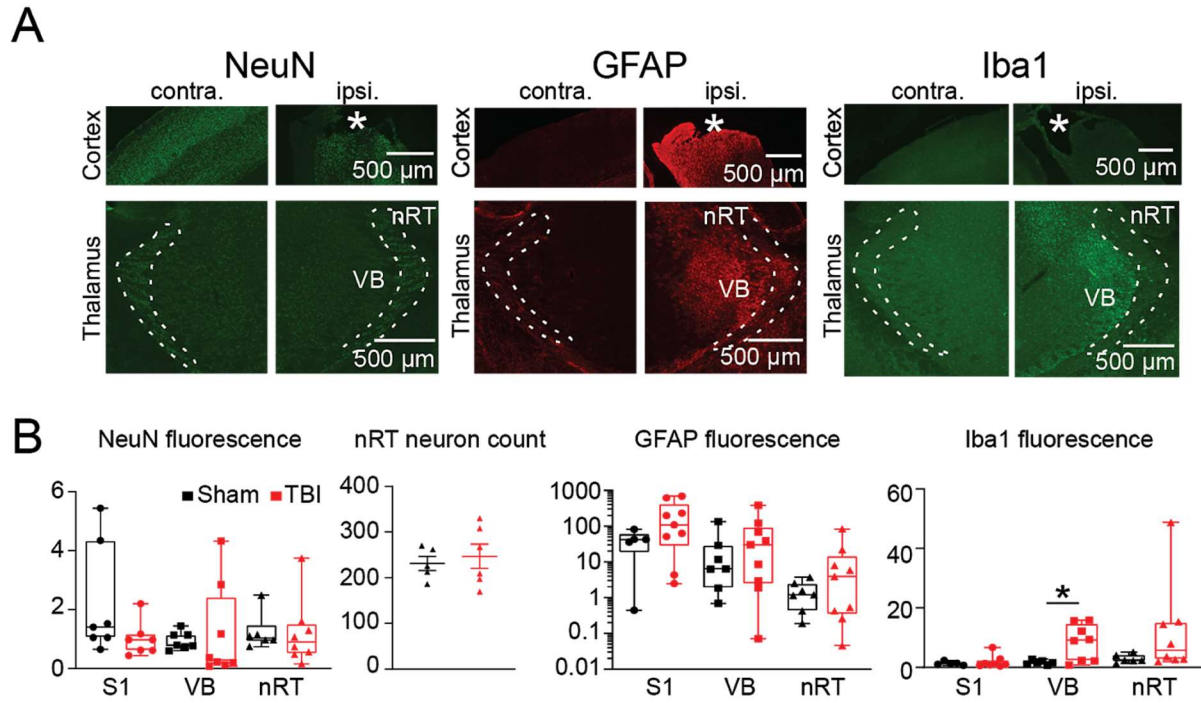


**Figure 2.S3. C1q<sup>-/-</sup> mice show reduced inflammation and neuron loss three weeks after TBI.**

A) Close-up images of S1 (top), VB and nRT (bottom) stained for NeuN, GFAP, and Iba1. Injury site in the right S1 cortex is marked by an asterisk. Scale bars, 500  $\mu$ m.

B) Quantification of fluorescence ratios between ipsilateral and contralateral regions in sham and TBI C1q<sup>-/-</sup> mice.

Data represent all points from min to max, with a Mann-Whitney test and  $\alpha = 0.05$  (\* $p < 0.05$ , \*\* $p < 0.01$ ). Analysis includes between four and six mice per group (n = one to three sections per mouse, one image per region).

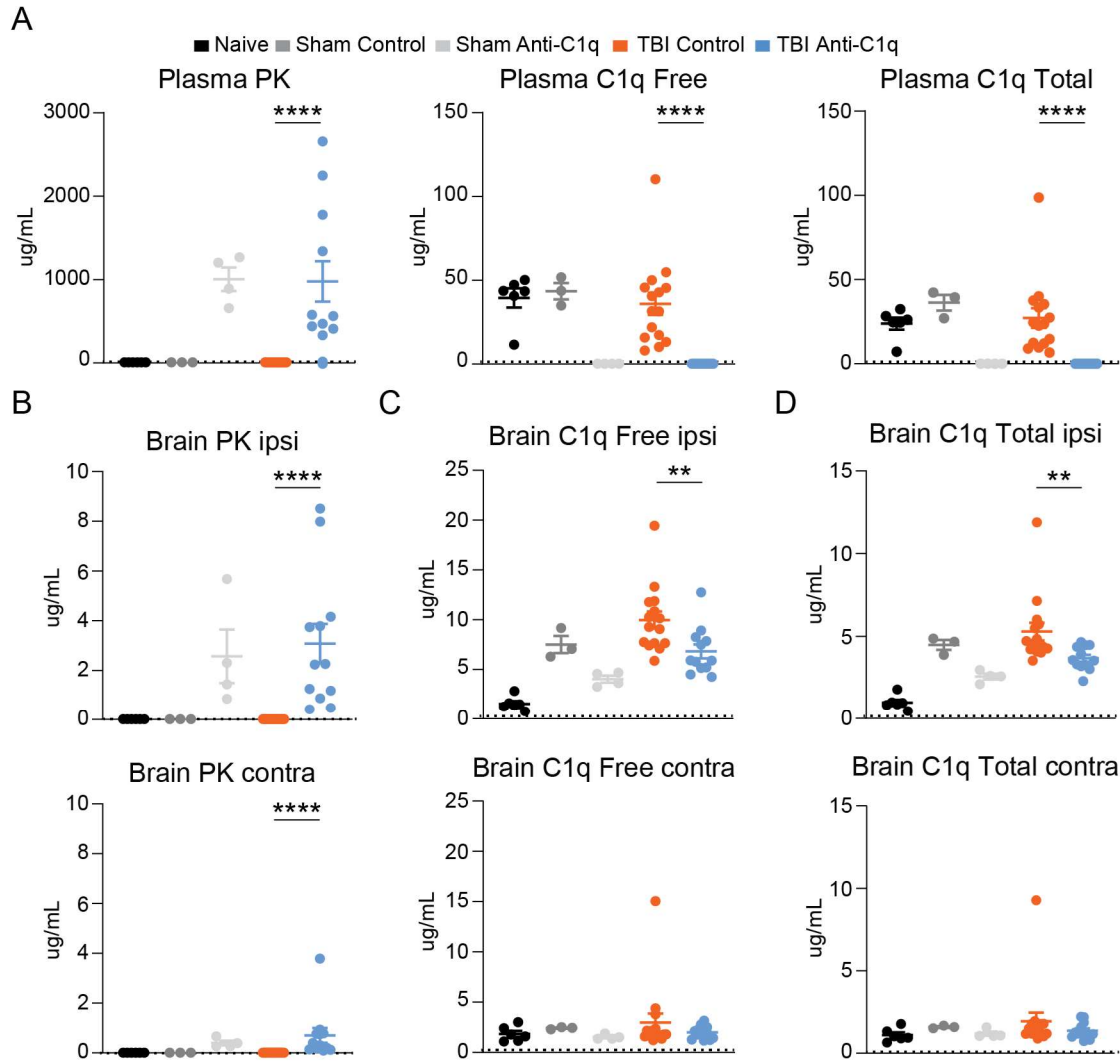


**Figure 2.S4. Plasma and brain PK/PD show presence of free drug and reduced C1q in anti-C1q drug-treated sham and TBI mice.**

A) Plasma levels of free drug, C1q-free, and C1q-total were measured using sandwich ELISAs after TBI and sham mice were treated with two doses of 100 mg/kg anti-C1q or isotype control antibodies. Dotted line shows lower limit of quantification.

B-F) Levels of free drug (B), C1q-free (C), and C1q-total (D) were measured in brain lysates in the ipsilateral (top) and contralateral (bottom) sides using sandwich ELISAs. Naïve mice were negative controls. Dotted line shows lower limit of quantification.

Data represent all points from min to max, with a Mann-Whitney test between TBI control and TBI anti-C1q, and  $\alpha = 0.05$  (\* $p < 0.05$ , \*\* $p < 0.01$ , \*\*\* $p < 0.001$ , \*\*\*\* $p < 0.0001$ ). Analysis includes between three and 15 mice per group.

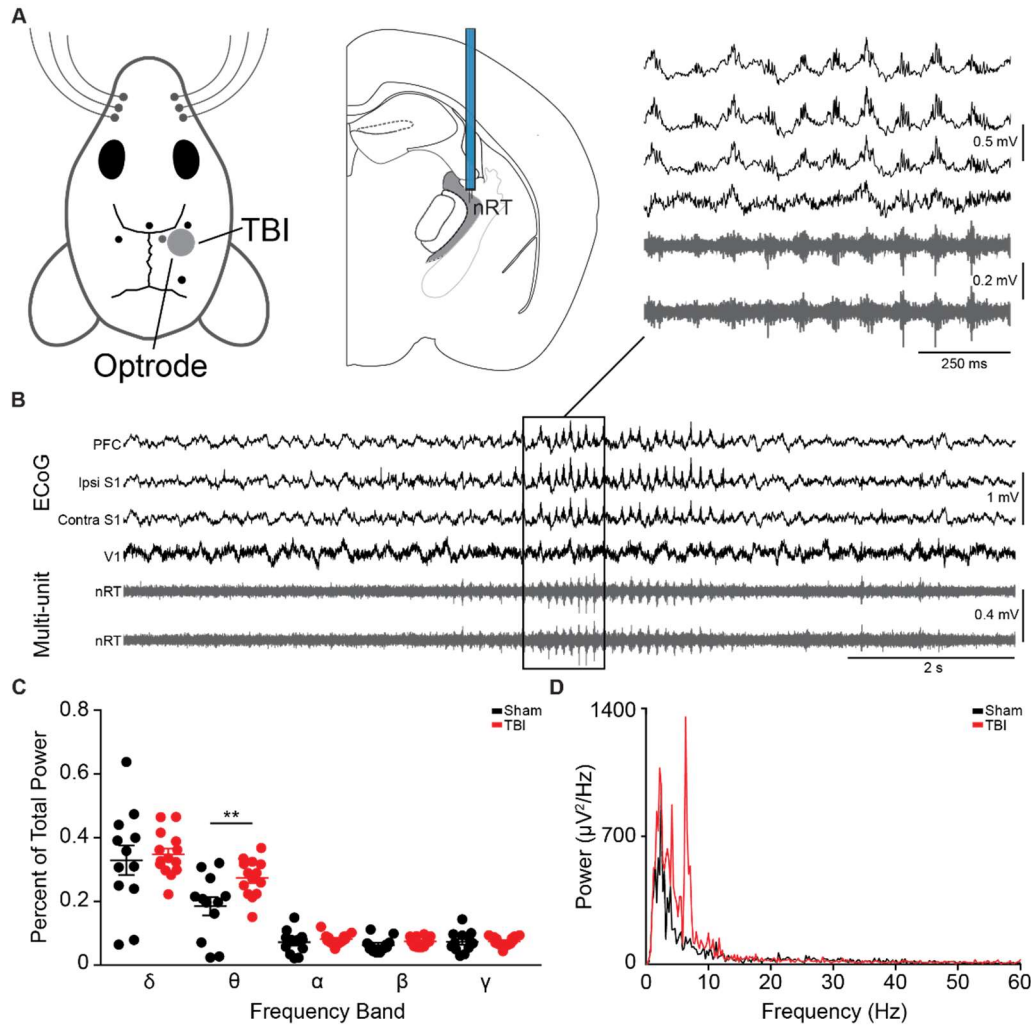


**Figure 2.S5. Mice with TBI have spontaneous seizure-like events in the theta to alpha frequency range that are time-locked with thalamic bursting.**

A) Diagram of recording locations for *in vivo* experiments. Left, ECoG recording sites and TBI location are shown on the mouse skull. Right, approximate location of tungsten depth electrodes implanted unilaterally in the nRT.

B) Representative ECoG traces from cortical recording sites and multi-unit traces from nRT showing a spontaneous seizure-like event.

C) Power spectral analysis showing the average power across different frequency bands in the first 15 minutes of baseline ECoG signal from the ipsilateral S1 cortex in sham and TBI mice.

D) Periodogram showing the power across frequencies taken from the first 15 minutes of baseline ECoG signal from the ipsilateral S1 cortex in a representative sham and TBI mouse.

Data represent mean  $\pm$  SEM analyzed with a Mann-Whitney test and  $\alpha = 0.05$  (\* $p < 0.05$ , \*\* $p < 0.01$ ). Analysis includes between 12 and 14 mice per group.

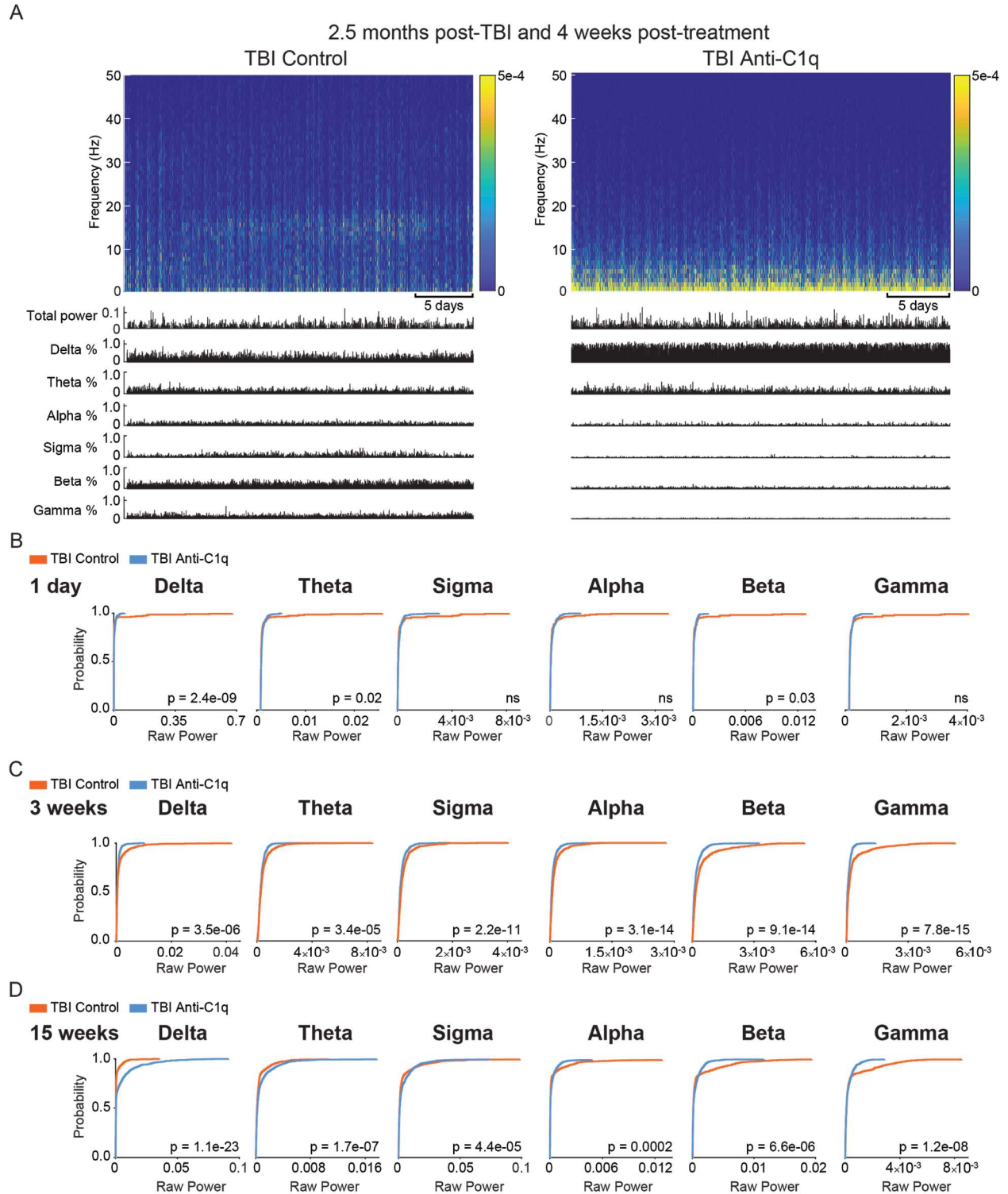


**Figure 2.S6. Anti-C1q antibody has chronic disease-modifying effects on EcoG power in mice with TBI.**

A) Example spectrograms (top) and histograms (bottom) from a control-treated mouse (left) and antibody-treated mouse (right) showing power across different frequency bands 2.5 months post-TBI, which was four weeks after the treatment ended. Power bands are sampled every 30 minutes.



B) Cumulative distribution functions for control-treated and antibody-treated cohorts sampled across different frequency bands in the first day post-TBI. We sampled 48 points from the first 24 hours within the start of each recording.

C) Same as B, but at three weeks post-TBI. We sampled 232 points between 15.25-20.1 days from the start of each recording.

D) Same as B, but at 9-15 weeks post-TBI. We sampled 296 points between 104.6 to 110 days from the start of each recording.

Data represent all mice recorded, even if they died before treatment ended. One control-treated mouse and one antibody-treated mouse died within three weeks post-TBI, two control-treated mice died within six weeks post-TBI, and the remaining mice were recorded for at least nine weeks post-TBI. At 24 hours,  $n =$  seven control-treated mice, seven antibody-treated mice. At three weeks,  $n =$  seven control-treated mice, seven antibody-treated mice. At 9-15 weeks  $n =$  six control-treated mice, four antibody-treated mice. Delta = 1-4 Hz, theta = 5-8 Hz, alpha = 9-12 Hz, sigma = 13-15 Hz, beta = 16-30 Hz, gamma = 31-50 Hz. ns =  $p > 0.05$ .

**Table 2.S1. Summary of intrinsic properties, EPSC, and IPSC data recorded from S1 cortex, VB, and nRT.** Mice were recorded between three and six weeks post-TBI, and recording conditions are described in the patch-clamp electrophysiology section of the methods. A Mann-Whitney test was performed for statistical analysis.

Intrinsic features	Cm (pF)	Vm (mV)	Rin (MOhm)	Tau (ms)	Rheobase (pA)	AP Thr. (mV)	AP Dur. (ms)	AP Amp. (mV)	cells	slices	mice
<b>L5 pyr.</b>											
<i>sham</i>	94 ± 9.5	-79 ± 2.2	388 ± 22	33 ± 2.0	55 ± 7.1	-55 ± 0.7	4.2 ± 0.2	71 ± 1.2	21	9	6
<i>TBI</i>	91 ± 9.7	-71 ± 2.4	421 ± 43	36 ± 4.8	54 ± 9.2	-51 ± 1.1	4.1 ± 0.3	60 ± 2.4	21	10	6
<i>MW p-value</i>	ns	0.03	ns	ns	ns	0.01	ns	0.0001			
<b>L5 FS</b>											
<i>sham</i>	58 ± 6.0	-70 ± 2.5	473 ± 71	33 ± 5.2	40 ± 8.8	-54 ± 0.4	1.7 ± 0.2	58 ± 2.4	9	6	6
<i>TBI</i>	54 ± 7.3	-72 ± 2.0	573 ± 91	27 ± 3.1	34 ± 5.7	-57 ± 1.2	1.7 ± 0.2	57 ± 2.2	14	9	6
<i>MW p-value</i>	ns	ns	ns	ns	ns	0.03	ns	ns			
<b>VB</b>											
<i>sham</i>	166 ± 18	-62 ± 1.2	198 ± 32	28 ± 3.2	158 ± 17	-50 ± 0.9	2.7 ± 0.2	51 ± 2.9	21-22	7	6
<i>TBI</i>	169 ± 12	-65 ± 1.2	200 ± 19	27 ± 2.6	170 ± 13	-51 ± 0.9	2.3 ± 0.1	49 ± 2.6	28-33	8	8
<i>MW p-value</i>	ns	ns	ns	ns	ns	ns	ns	ns			
<b>nRT</b>											
<i>sham</i>	91 ± 13	-74 ± 3.1	402 ± 58	27 ± 2.8	42 ± 5.5	-53 ± 1.3	1.3 ± 0.1	55 ± 2.2	10	7	5
<i>TBI</i>	82 ± 10	-60 ± 3.5	523 ± 114	44 ± 11	69 ± 26	-50 ± 1.5	1.4 ± 0.1	45 ± 3.2	9	6	5
<i>MW p-value</i>	ns	0.009	ns	ns	ns	ns	ns	0.03			

EPSCs	Frequency (Hz)	Charge (pA x ms)	Amplitude (pA)	Half-width (ms)	Rise time (ms)	Decay time (ms)	Tau (ms)	cells	slices	mice
<b>L5 pyr.</b>										
<i>sham</i>	0.2 ± 0.1	117 ± 7.5	25 ± 1.3	2.2 ± 0.2	1.1 ± 0.1	5.2 ± 0.4	4.0 ± 0.2	21	9	6
<i>TBI</i>	0.6 ± 0.2	107 ± 9.1	27 ± 2.4	2.1 ± 0.2	0.9 ± 0.1	5.5 ± 0.4	3.0 ± 0.2	16	10	6
<i>MW p-value</i>	ns	ns	ns	ns	ns	ns	0.01			
<b>L5 FS</b>										
<i>sham</i>	1.4 ± 0.5	56 ± 2.4	26 ± 0.8	1.0 ± 0.1	0.4 ± 0.02	3.0 ± 0.4	1.6 ± 0.1	8	6	6
<i>TBI</i>	1.2 ± 0.4	55 ± 6.3	29 ± 3.6	1.1 ± 0.2	0.4 ± 0.04	3.0 ± 0.6	1.5 ± 0.2	11	10	6
<i>MW p-value</i>	ns	ns	ns	ns	ns	ns	ns			
<b>VB</b>										
<i>sham</i>	0.9 ± 0.2	54 ± 4.4	22 ± 1.6	1.4 ± 0.2	0.4 ± 0.03	4.2 ± 0.7	1.9 ± 0.2	15	7	7
<i>TBI</i>	1.0 ± 0.4	50 ± 4.6	21 ± 1.6	1.2 ± 0.1	0.5 ± 0.1	3.6 ± 0.5	1.8 ± 0.2	13	8	7
<i>MW p-value</i>	ns	ns	ns	ns	ns	ns	ns			
<b>nRT</b>										
<i>sham</i>	2.9 ± 0.6	32 ± 2.3	28 ± 1.8	0.7 ± 0.1	0.3 ± 0.03	1.7 ± 0.2	0.7 ± 0.1	11	6	6
<i>TBI</i>	1.9 ± 0.4	30 ± 2.0	22 ± 1.8	0.9 ± 0.1	0.3 ± 0.1	2.3 ± 0.3	1.0 ± 0.2	9	7	7
<i>MW p-value</i>	ns	ns	0.04	ns	ns	ns	ns			

IPSCs	Frequency (Hz)	Charge (pA x ms)	Amplitude (pA)	Half-width (ms)	Rise time (ms)	Decay time (ms)	Tau (ms)	cells	slices	mice
<b>L5 pyr.</b>										
<i>sham</i>	1.2 ± 0.2	471 ± 49	39 ± 2.7	6.1 ± 0.3	1.1 ± 0.1	21.1 ± 1.0	10.0 ± 0.4	19	8	6
<i>TBI</i>	1.3 ± 0.3	397 ± 36	36 ± 2.7	5.6 ± 0.3	1.2 ± 0.1	18.0 ± 1.2	8.4 ± 0.4	16	6	6
<i>MW p-value</i>	ns	ns	ns	ns	ns	0.04	0.02			
<b>VB</b>										
<i>sham</i>	2.4 ± 0.8	884 ± 360	47 ± 5.6	5.4 ± 0.4	1.2 ± 0.1	20 ± 3.8	12 ± 4.7	10	6	5
<i>TBI</i>	1.9 ± 0.4	566 ± 127	42 ± 5.1	6.6 ± 0.8	1.1 ± 0.1	24 ± 6.6	10 ± 2.9	11	5	4
<i>MW p-value</i>	ns	ns	ns	ns	ns	ns	ns			
<b>nRT</b>										
<i>sham</i>	0.9 ± 0.2	836 ± 103	21 ± 2.7	16 ± 2.1	1.3 ± 0.1	69 ± 9.0	55 ± 6.0	13	5	4
<i>TBI</i>	0.6 ± 0.2	1144 ± 141	18 ± 1.6	30 ± 2.5	2.7 ± 0.4	79 ± 7.9	73 ± 3.5	22	9	6
<i>MW p-value</i>	0.02	ns	ns	0.0003	0.0002	ns	0.04			

**Table 2.S2. Summary of epileptiform activity analysis in sham, TBI, control-treated TBI, and antibody-treated TBI mice.** Mice were recorded continuously starting the day of the TBI up until several weeks post-TBI. Surgical and recording conditions are described in the methods section titled “Surgical implantation of devices for chronic ECoG recordings”. Analysis was performed on the first 24 hours post-TBI, and across a 48 hour window at three weeks post-TBI. A repeated measures mixed-effects ANOVA was performed for statistical analysis.

First 24 hours	Epileptiform spikes	Epileptiform discharges	Spike-and-wave discharges	Generalized tonic-clonic seizures	Acute post-injury mortality
<i>Sham</i>	8/8 (100%)	6/8 (75%)	0/8 (0%)	0/8 (0%)	0/8 (0%)
<i>TBI</i>	16/16 (100%)	13/16 (81%)	4/16 (25%)	3/16 (19%)	0/16 (0%)
<b>Drug study</b>					
<i>TBI Vehicle</i>	7/7 (100%)	5/7 (71%)	0/7 (0%)	2/7 (28%)	0/7 (0%)
<i>TBI anti-C1q</i>	7/7 (100%)	5/7 (71%)	0/7 (0%)	1/7 (14%)	0/7 (0%)

3 weeks	Epileptiform spikes	Epileptiform discharges	Spike-and-wave discharges	Generalized tonic-clonic seizures
<i>Sham</i>	7/7 (100%)	1/7 (14%)	0/7 (0%)	0/7 (0%)
<i>TBI</i>	11/11 (100%)	3/11 (27%)	1/11 (9%)	0/11 (0%)
<b>Drug study</b>				
<i>TBI Vehicle</i>	7/7 (100%)	2/7 (28%)	0/7 (0%)	0/7 (0%)
<i>TBI anti-C1q</i>	7/7 (100%)	3/7 (43%)	0/7 (0%)	0/7 (0%)

	Epileptiform spikes	Epileptiform discharges	Spike-and-wave discharges	Generalized tonic-clonic seizures	mice
<i>Sham – 24h</i>	234 ± 62	4 ± 2	0	0	8
<i>TBI – 24h</i>	452 ± 178	8 ± 6	1 ± 0.6	0.4 ± 0.2	16
<i>Sham – 3wk</i>	66 ± 38	0.7 ± 0.7	0	0	7
<i>TBI – 3wk</i>	292 ± 114	2 ± 1	0.09 ± 0.09	0	11
<i>Mixed-effects analysis</i>	ns	ns	ns	ns	
<b>Drug study</b>					
<i>TBI Vehicle – 24h</i>	278 ± 79	4 ± 1	0	0.6 ± 0.4	7
<i>TBI anti-C1q – 24h</i>	137 ± 55	1 ± 0.5	0	0.3 ± 0.3	7
<i>TBI Vehicle – 3wk</i>	300 ± 92	0.3 ± 0.2	0	0	7
<i>TBI anti-C1q – 3wk</i>	274 ± 50	1 ± 0.8	0	0	7
<i>Mixed-effects analysis</i>	ns	ns	ns	ns	

## References

- Antón-Bolaños, N., Espinosa, A., López-Bendito, G., 2018. Developmental interactions between thalamus and cortex: a true love reciprocal story. *Curr. Opin. Neurobiol.* 52, 33–41.
- Aronica, E., Boer, K., van Vliet, E.A., Redeker, S., Baayen, J.C., Spliet, W.G.M., van Rijen, P.C., Troost, D., da Silva, F.H.L., Wadman, W.J., Gorter, J.A., 2007. Complement activation in experimental and human temporal lobe epilepsy. *Neurobiol. Dis.* 26, 497–511.
- Auladell, C., Pérez-Sust, P., Supèr, H., Soriano, E., 2000. The early development of thalamocortical and corticothalamic projections in the mouse. *Anat. Embryol.* 201, 169–179.
- Beenhakker, M.P., Huguenard, J.R., 2009. Neurons that fire together also conspire together: is normal sleep circuitry hijacked to generate epilepsy? *Neuron* 62, 612–632.
- Bellander, B.M., Singhrao, S.K., Ohlsson, M., Mattsson, P., Svensson, M., 2001. Complement activation in the human brain after traumatic head injury. *J. Neurotrauma* 18, 1295–1311.
- Blakemore, C., Molnár, Z., 1990. Factors involved in the establishment of specific interconnections between thalamus and cerebral cortex. *Cold Spring Harb. Symp. Quant. Biol.* 55, 491–504.
- Bolkvadze, T., Pitkänen, A., 2012. Development of post-traumatic epilepsy after controlled cortical impact and lateral fluid-percussion-induced brain injury in the mouse. *J. Neurotrauma* 29, 789–812.

- Bourassa, J., Pinault, D., Deschênes, M., 1995. Corticothalamic projections from the cortical barrel field to the somatosensory thalamus in rats: a single-fibre study using biocytin as an anterograde tracer. *Eur. J. Neurosci.* 7, 19–30.
- Bragin, A., Li, L., Almajano, J., Alvarado-Rojas, C., Reid, A.Y., Staba, R.J., Engel, J., 2016. Pathologic electrographic changes after experimental traumatic brain injury. *Epilepsia* 57, 735–745.
- Briggs, F., Usrey, W.M., 2008. Emerging views of corticothalamic function. *Curr. Opin. Neurobiol.* 18, 403–407.
- Cho, K., 2019. Emerging Roles of Complement Protein C1q in Neurodegeneration. *Aging Dis* 10, 652–663.
- Church, M.W., 1975. Changes in frequency and amplitude of delta activity during sleep. *Electroencephalogr Clin Neurophysiol* 39, 1–7.
- Clemente-Perez, A., Makinson, S.R., Higashikubo, B., Brovarney, S., Cho, F.S., Urry, A., Holden, S.S., Wimer, M., Dávid, C., Fenno, L.E., Acsády, L., Deisseroth, K., Paz, J.T., 2017. Distinct Thalamic Reticular Cell Types Differentially Modulate Normal and Pathological Cortical Rhythms. *Cell Rep* 19, 2130–2142.
- Destexhe, A., Contreras, D., Steriade, M., 1998. Mechanisms underlying the synchronizing action of corticothalamic feedback through inhibition of thalamic relay cells. *J. Neurophysiol.* 79, 999–1016.

- Dewan, M.C., Rattani, A., Gupta, S., Baticulon, R.E., Hung, Y.-C., Panchak, M., Agrawal, A., Adeleye, A.O., Shrimel, M.G., Rubiano, A.M., Rosenfeld, J.V., Park, K.B., 2018. Estimating the global incidence of traumatic brain injury. *J. Neurosurg.* 1–18.
- Ding, K., Gupta, P.K., Diaz-Arrastia, R., 2016. Epilepsy after Traumatic Brain Injury, in: Laskowitz, D., Grant, G. (Eds.), *Translational Research in Traumatic Brain Injury*, *Frontiers in Neuroscience*. CRC Press/Taylor and Francis Group, Boca Raton (FL).
- Golshani, P., Liu, X.B., Jones, E.G., 2001. Differences in quantal amplitude reflect GluR4- subunit number at corticothalamic synapses on two populations of thalamic neurons. *Proc. Natl. Acad. Sci. U.S.A.* 98, 4172–4177.
- Grossman, E.J., Ge, Y., Jensen, J.H., Babb, J.S., Miles, L., Reaume, J., Silver, J.M., Grossman, R.I., Inglese, M., 2012. Thalamus and cognitive impairment in mild traumatic brain injury: a diffusional kurtosis imaging study. *J. Neurotrauma* 29, 2318–2327.
- Grossman, E.J., Inglese, M., 2016. The Role of Thalamic Damage in Mild Traumatic Brain Injury. *J. Neurotrauma* 33, 163–167.
- Hammad, A., Westacott, L., Zaben, M., 2018. The role of the complement system in traumatic brain injury: a review. *J Neuroinflammation* 15, 24.
- Hong, S., Beja-Glasser, V.F., Nfonoyim, B.M., Frouin, A., Li, S., Ramakrishnan, S., Merry, K.M., Shi, Q., Rosenthal, A., Barres, B.A., Lemere, C.A., Selkoe, D.J., Stevens, B., 2016. Complement and microglia mediate early synapse loss in Alzheimer mouse models. *Science* 352, 712–716.

Huang, M.-X., Theilmann, R.J., Robb, A., Angeles, A., Nichols, S., Drake, A., D'Andrea, J., Levy, M., Holland, M., Song, T., Ge, S., Hwang, E., Yoo, K., Cui, L., Baker, D.G., Trauner, D., Coimbra, R., Lee, R.R., 2009. Integrated imaging approach with MEG and DTI to detect mild traumatic brain injury in military and civilian patients. *J. Neurotrauma* 26, 1213–1226.

Huntsman, M.M., Porcello, D.M., Homanics, G.E., DeLorey, T.M., Huguenard, J.R., 1999. Reciprocal inhibitory connections and network synchrony in the mammalian thalamus. *Science* 283, 541–543.

Krukowski, K., Chou, A., Feng, X., Tiret, B., Paladini, M.-S., Riparip, L.-K., Chaumeil, M.M., Lemere, C., Rosi, S., 2018. Traumatic Brain Injury in Aged Mice Induces Chronic Microglia Activation, Synapse Loss, and Complement-Dependent Memory Deficits. *Int J Mol Sci* 19.

Lam, Y.-W., Sherman, S.M., 2011. Functional organization of the thalamic input to the thalamic reticular nucleus. *J. Neurosci.* 31, 6791–6799.

Lansita, J.A., Mease, K.M., Qiu, H., Yednock, T., Sankaranarayanan, S., Kramer, S., 2017. Nonclinical Development of ANX005: A Humanized Anti-C1q Antibody for Treatment of Autoimmune and Neurodegenerative Diseases. *Int. J. Toxicol.* 36, 449–462.

Lee, R.R., Huang, M., 2014. Magnetoencephalography in the diagnosis of concussion. *Prog Neurol Surg* 28, 94–111.

Liddelow, S.A., Guttenplan, K.A., Clarke, L.E., Bennett, F.C., Bohlen, C.J., Schirmer, L., Bennett, M.L., Münch, A.E., Chung, W.-S., Peterson, T.C., Wilton, D.K., Frouin, A., Napier, B.A., Panicker, N., Kumar, M., Buckwalter, M.S., Rowitch, D.H., Dawson, V.L., Dawson, T.M.,



- Stevens, B., Barres, B.A., 2017. Neurotoxic reactive astrocytes are induced by activated microglia. *Nature* 541, 481–487.
- Lu, D.C., Zador, Z., Yao, J., Fazlollahi, F., Manley, G.T., 2011. Aquaporin-4 Reduces Post-Traumatic Seizure Susceptibility by Promoting Astrocytic Glial Scar Formation in Mice. *J. Neurotrauma*.
- Lu, X.-C.M., Hartings, J.A., Si, Y., Balbir, A., Cao, Y., Tortella, F.C., 2011. Electrocortical pathology in a rat model of penetrating ballistic-like brain injury. *J. Neurotrauma* 28, 71–83.
- Lui, H., Zhang, J., Makinson, S.R., Cahill, M.K., Kelley, K.W., Huang, H.-Y., Shang, Y., Oldham, M.C., Martens, L.H., Gao, F., Coppola, G., Sloan, S.A., Hsieh, C.L., Kim, C.C., Bigio, E.H., Weintraub, S., Mesulam, M.-M., Rademakers, R., Mackenzie, I.R., Seeley, W.W., Karydas, A., Miller, B.L., Borroni, B., Ghidoni, R., Farese, R.V., Paz, J.T., Barres, B.A., Huang, E.J., 2016. Progranulin Deficiency Promotes Circuit-Specific Synaptic Pruning by Microglia via Complement Activation. *Cell* 165, 921–935.
- McGonigal, R., Cunningham, M.E., Yao, D., Barrie, J.A., Sankaranarayanan, S., Fewou, S.N., Furukawa, K., Yednock, T.A., Willison, H.J., 2016. C1q-targeted inhibition of the classical complement pathway prevents injury in a novel mouse model of acute motor axonal neuropathy. *Acta Neuropathol Commun* 4, 23.
- Mckee, A.C., Daneshvar, D.H., 2015. The neuropathology of traumatic brain injury. *Handb Clin Neurol* 127, 45–66.
- Mills, C.D., Kincaid, K., Alt, J.M., Heilman, M.J., Hill, A.M., 2000. M-1/M-2 macrophages and the Th1/Th2 paradigm. *J. Immunol.* 164, 6166–6173.

- Orme, I.M., Robinson, R.T., Cooper, A.M., 2015. The balance between protective and pathogenic immune responses in the TB-infected lung. *Nat. Immunol.* 16, 57–63.
- Paz, J.T., Bryant, A.S., Peng, K., Fenno, L., Yizhar, O., Frankel, W.N., Deisseroth, K., Huguenard, J.R., 2011. A new mode of corticothalamic transmission revealed in the *Gria4(-/-)* model of absence epilepsy. *Nat. Neurosci.* 14, 1167–1173.
- Paz, J.T., Huguenard, J.R., 2015. Microcircuits and their interactions in epilepsy: is the focus out of focus? *Nat. Neurosci.* 18, 351–359.
- Ritter-Makinson, S., Clemente-Perez, A., Higashikubo, B., Cho, F.S., Holden, S.S., Bennett, E., Chkhaidze, A., Eelkman Rooda, O.H.J., Cornet, M.-C., Hoebeek, F.E., Yamakawa, K., Cilio, M.R., Delord, B., Paz, J.T., 2019. Augmented Reticular Thalamic Bursting and Seizures in *Scn1a*-Dravet Syndrome. *Cell Rep* 26, 1071.
- Ronne-Engstrom, E., Winkler, T., 2006. Continuous EEG monitoring in patients with traumatic brain injury reveals a high incidence of epileptiform activity. *Acta Neurol. Scand.* 114, 47–53.
- Ross, D.T., Ebner, F.F., 1990. Thalamic retrograde degeneration following cortical injury: an excitotoxic process? *Neuroscience* 35, 525–550.
- Ross, D.T., Graham, D.I., Adams, J.H., 1993. Selective loss of neurons from the thalamic reticular nucleus following severe human head injury. *J. Neurotrauma* 10, 151–165.

- Russo, M.V., McGavern, D.B., 2016. Inflammatory neuroprotection following traumatic brain injury. *Science* 353, 783–785.
- Sachdev, R.N.S., Gaspard, N., Gerrard, J.L., Hirsch, L.J., Spencer, D.D., Zaveri, H.P., 2015. Delta rhythm in wakefulness: evidence from intracranial recordings in human beings. *J. Neurophysiol.* 114, 1248–1254.
- Schiering, I.A.M., de Haan, T.R., Niermeijer, J.-M.F., Koelman, J.H., Majoie, C.B.L.M., Reneman, L., Aronica, E., 2014. Correlation between clinical and histologic findings in the human neonatal hippocampus after perinatal asphyxia. *J. Neuropathol. Exp. Neurol.* 73, 324–334.
- Scott, G., Hellyer, P.J., Ramlackhansingh, A.F., Brooks, D.J., Matthews, P.M., Sharp, D.J., 2015. Thalamic inflammation after brain trauma is associated with thalamo-cortical white matter damage. *J Neuroinflammation* 12, 224.
- Simon, D.W., McGeachy, M.J., Bayir, H., Clark, R.S.B., Loane, D.J., Kochanek, P.M., 2017. The far-reaching scope of neuroinflammation after traumatic brain injury. *Nat Rev Neurol* 13, 171–191.
- Sohal, V.S., Huguenard, J.R., 2003. Inhibitory interconnections control burst pattern and emergent network synchrony in reticular thalamus. *J. Neurosci.* 23, 8978–8988.
- Sohal, V.S., Huntsman, M.M., Huguenard, J.R., 2000. Reciprocal inhibitory connections regulate the spatiotemporal properties of intrathalamic oscillations. *J. Neurosci.* 20, 1735–1745.
- Stevens, B., Allen, N.J., Vazquez, L.E., Howell, G.R., Christopherson, K.S., Nouri, N., Micheva, K.D., Mehalow, A.K., Huberman, A.D., Stafford, B., Sher, A., Litke, A.M., Lambris, J.D., Smith, S.J.,

John, S.W.M., Barres, B.A., 2007. The classical complement cascade mediates CNS synapse elimination. *Cell* 131, 1164–1178.

Wang, H., Song, G., Chuang, H., Chiu, C., Abdelmaksoud, A., Ye, Y., Zhao, L., 2018. Portrait of glial scar in neurological diseases. *Int J Immunopathol Pharmacol* 31, 2058738418801406.

Wimmer, R.D., Schmitt, L.I., Davidson, T.J., Nakajima, M., Deisseroth, K., Halassa, M.M., 2015. Thalamic control of sensory selection in divided attention. *Nature* 526, 705–709.

Wyatt, S.K., Witt, T., Barbaro, N.M., Cohen-Gadol, A.A., Brewster, A.L., 2017. Enhanced classical complement pathway activation and altered phagocytosis signaling molecules in human epilepsy. *Exp. Neurol.* 295, 184–193.

Yingling, C.D., Skinner, J.E., 1976. Selective regulation of thalamic sensory relay nuclei by nucleus reticularis thalami. *Electroencephalogr Clin Neurophysiol* 41, 476–482.

You, Z., Yang, J., Takahashi, K., Yager, P.H., Kim, H.-H., Qin, T., Stahl, G.L., Ezekowitz, R.A.B., Carroll, M.C., Whalen, M.J., 2007. Reduced tissue damage and improved recovery of motor function after traumatic brain injury in mice deficient in complement component C4. *J. Cereb. Blood Flow Metab.* 27, 1954–1964.

### **Chapter 3 : Investigating the therapeutic effects of small molecules on neuroinflammation and seizure susceptibility after traumatic brain injury**

#### **Abstract**

Astrocytes play a central role in supporting neuronal function and are also involved in the inflammatory response following traumatic brain injury (TBI). However, if astrocytes remain chronically inflamed, or reactive, they may become detrimental to neuronal survival. One potential approach to reduce the chronic reactivity of astrocytes is to reprogram them with small molecule therapeutics. Preliminary studies have identified a small molecule, RA8, that can reprogram astrocyte transcriptional states, and RA8 treatment of mice with stroke may have protective effects in the brain. Using a mouse model of cortical injury, we tested the potential therapeutic effects of RA8 in TBI outcomes such as neuroinflammation, neurovascular changes, and seizure susceptibility.

## Introduction

Astrocytes are critical for maintaining neuronal function, ionic balance, glial signaling, and blood brain barrier (BBB) integrity (Chen and Swanson, 2003; Karve et al., 2016). Astrocytes are known to become “reactive” as part of the inflammatory response to trauma such as a traumatic brain injury (TBI), for example by changing morphology and gene expression (Burda et al., 2016, Karve et al., 2016) or forming a glial scar to separate out damaged and healthy tissue (Sofroniew, 2009). This response can be protective when astrocytes produce factors to support regeneration (Kim et al., 2010; Madathil et al., 2013), but chronically persistent reactive astrocytes can be pathological if they continue to produce pro-inflammatory cytokines and chemokines and cause further BBB disruption (Blecharz-Lang et al. 2018, Carpentier et al., 2005, Liddelow et al., 2017). Thus, it could be useful to reprogram astrocytes into different, non-reactive states post-TBI. Several groups have demonstrated that glial cells can be reprogrammed into neurons or other states (Mattugini et al., 2019; Zhang et al., 2015).

The Ding lab, our collaborators at the Gladstone Institutes, discovered a small molecule, RA8, that can reprogram both human and mouse astrocytic transcriptional states. RA8 was initially identified through a high-throughput screen as a molecule that reprograms astrocyte-restricted neural precursors toward a neural fate by modulating RNA splicing via action on the ribonucleoprotein H. Our preliminary studies have shown that in mice recovering from stroke, RA8 treatment reduces astrogliosis and neuronal loss (**Figure 3.S1, Figure 3.S2**) and decreases seizure susceptibility. Given these positive outcomes in stroke, we decided to also test the potential therapeutic effects of RA8 treatment in TBI, as these two types of trauma have overlapping pathophysiology (Bramlett and Dietrich, 2004). Specifically, we wanted to know whether RA8 treatment could reduce reactive astrocytes or neuronal loss, change vascular density, or reduce seizure susceptibility in TBI mice.

## Results

### **RA8 treatment does not chronically reduce GFAP expression but could be protective of neuronal loss**

To determine if RA8 treatment could reduce chronic inflammation or neuronal loss after TBI, we induced a mild cortical impact injury to the right primary somatosensory cortex (S1) of adult mice, treated mice daily for two weeks with an i.p. injection of RA8 or vehicle starting 24 hours post-TBI, and assessed the impact on their brains eight weeks later. We performed immunofluorescent staining of coronal brain sections with markers of neurons (NeuN) and astrocytes (GFAP) (**Figure 3.1**), and analyzed expression in the peri-TBI S1 cortex and the functionally connected ventrobasal thalamus (VB), and reticular nucleus (nRT). At eight weeks post-TBI, vehicle-treated TBI mice had significantly higher GFAP expression in VB and nRT than sham mice (**Figure 3.1C**). RA8-treated TBI mice also had significantly higher GFAP expression in VB and nRT than sham mice, at the same level as vehicle-treated TBI mice, suggesting that the two-week RA8 treatment did not have lasting effects on GFAP expression in astrocytes, but it does not rule out the possibility that RA8 could have transiently reduced GFAP levels during the treatment, or could have altered other aspects of astrocyte transcriptional state or function.

At eight weeks post-TBI, we did not observe any differences in NeuN fluorescence in the cortex or thalamus between sham, vehicle-treated, or RA8-treated TBI mice (**Figure 3.1**). It is unclear why we do not observe reduced NeuN expression, as we would expect neuronal loss to persist, but it's possible that the staining quality was affected by how long the perfused brains remained in sucrose before staining (see methods for details). We also performed immunofluorescent staining for CD31, a marker of endothelial cells (Simmons et al., 1990, Lertkiatmongkol et al., 2016), to investigate whether vessel density was altered by TBI or RA8 treatment. Previous studies using various TBI models in rodents have observed vascular changes in the cortex and thalamus, particularly increased thalamic vessel density (Glushakov et al., 2018, Hayward et al.,

2010). At eight weeks, we did not observe any major differences in the vessel density ratio between sham, vehicle-treated, and RA8-treated TBI mice. These results suggest that vascular changes in the thalamus may take place at later time points after TBI, which would align with studies that looked between three and nine months (Glushakov et al., 2018, Hayward et al., 2010). Vascular density changes occur secondarily from BBB disruption, which is observed early on around the injury site (Chodobski et al., 2011).

### **Mice with TBI have increased seizure susceptibility**

We assessed susceptibility to electrographic and behavioral seizures from sham and TBI mice three weeks post-TBI (**Figure 3.3**). For this purpose, we used the pentylenetetrazol (PTZ, 45 mg/kg, i.p.) challenge, which is a well-established approach for measuring seizure susceptibility (Bolkvadze and Pitkänen, 2012). We found that TBI mice were more likely to show generalized tonic-clonic seizures than sham mice (**Figures 3.3B and 3.3D**). We also observed that TBI mice had a shorter latency to the first myoclonic jerk than sham mice (**Figures 3.3C and 3.3E**), but no change in the latency to the convulsive seizure (**Figures 3.3C and 3.3F**), indicating that TBI increases susceptibility for generalized tonic-clonic seizures and reduces the latency to early seizure stages. These results suggest that mild TBI induces network hyperexcitability similar to what has been shown previously in more severe TBI (Bolkvadze and Pitkänen, 2012).

### **RA8 treatment does not greatly alter seizure susceptibility**

We next wanted to know whether RA8 treatment could reduce seizure susceptibility in TBI mice (**Figure 3.4**). We once again used a PTZ challenge (35 mg/kg, i.p.) in sham, vehicle-treated TBI mice, and RA8-treated TBI mice. The dose was adjusted in this cohort because a larger dose of 45 mg/kg PTZ caused seizures in almost 50% of the sham mice. Six weeks post-TBI, we found that vehicle-treated TBI mice were more likely to show generalized tonic-clonic seizures than sham mice, but the two-week RA8 treatment did not significantly reduce the number of TBI mice that had a seizure (**Figure 3.4B**). We also did not observe major differences in latency to the first



myoclonic or the convulsive seizure between any of the groups (**Figures 3.4C-E**). We conclude that a short-term RA8 treatment does not alter later susceptibility to PTZ-induced seizures.

## Discussion

In this study, we investigated whether treatment with a small molecule, RA8, could alter TBI pathophysiologies including neuroinflammation and seizure susceptibility. Because RA8 can reprogram astrocyte transcriptional states, we hypothesized that treating TBI mice with this small molecule might have beneficial effects on astrocyte-related outcomes such as inflammation and neurovascular disruption.

Even though RA8 did not reduce GFAP expression in our fluorescence analysis, the treatment could have converted some astrocytes, perhaps those that are not expressing GFAP, into a neural fate. There are many other astrocyte markers that could also be altered by RA8, which should be investigated further. Although we did not see decreased NeuN fluorescence in vehicle-treated TBI mice as we expected, other analyses such as neuron counts might reveal more subtle differences that we could not observe with fluorescence analysis alone. Neuron loss analyzed by fluorescence alone may be underestimated if there is associated loss of brain structure volume, because the density of remaining neurons is preserved. Furthermore, treatment timing may play an important role in the outcomes we observed. To maximize the data we could get from a single pilot study cohort, mice were treated for two weeks, tested twice for seizure susceptibility at three and six weeks post-TBI, then perfused at eight weeks post-TBI for immunohistochemical staining. One major strength of this approach is the ability to look at correlations between factors such as lesion size, inflammation, and seizure susceptibility within individual mice. A disadvantage is having limits on the timing of various experimental endpoints. For example, future studies could determine if RA8 has a more transient effect on inflammation or neuron loss after TBI by performing histology during or shortly after RA8 treatment.

Seizure susceptibility is one of many approaches to test the excitability of the brain. It is useful because it can be used to test excitability in cohorts that do not necessarily show spontaneous epileptic seizures, but there are a few alternatives to PTZ, including pro-convulsant drugs like

kainic acid. Even if spontaneous seizures are present, they can be difficult to capture because they occur randomly and infrequently. However, seizure susceptibility does not always identify which individuals are or will become epileptic (Bolkvadze and Pitkanen, 2012). Even though RA8 treatment did not affect seizure susceptibility in TBI mice six weeks post-TBI (which was four weeks after the treatment ended), it is possible that the treatment could reduce seizure susceptibility during the treatment period, reduce hyperexcitability in other susceptibility assays, or it could reduce other types of spontaneous epileptiform activities which we could not test within the time frame of the study. We did see a trend toward increased latency to different seizure stages in RA8-treated TBI mice, but further experiments will need to be conducted to understand the full therapeutic effects of RA8 in TBI.

Overall, there is great potential and a wealth of research in animal models investigating small molecule therapeutic treatments for TBI and post-TBI outcomes (Chou et al., 2017, Hoane et al., 2009, Knobloch and Faden 2002, Singleton et al., 2010). Small molecule treatments are less invasive and easier to produce or distribute than alternative interventions being explored for TBI therapy, such as stem cell transplants. One major challenge of clinical trials for TBI treatments is finding an intervention that can target multiple factors contributing to neurodegeneration or loss of cognitive function across different time points after injury. It is likely that a combination of small molecule treatments will be the most successful in mitigating or preventing adverse health outcomes after TBI.

## **Materials & Methods**

### **Animals**

We performed all experiments per protocols approved by the Institutional Animal Care and Use Committee at the University of California, San Francisco and Gladstone Institutes. Precautions were taken to minimize stress and the number of animals used in each set of experiments. Mice were separately housed after surgical implants. Adult (P30-P180) male CD1 mice were used for all experiments.

### **Controlled cortical impact**

We anesthetized mice with 2-5% isoflurane and placed them in a stereotaxic frame. We performed a 3 mm craniotomy over the right somatosensory cortex (S1) centered at -1 mm posterior from Bregma, +3 mm lateral from the midline (**Figure 2.1A**). TBI was performed with a CCI device (Impact One Stereotaxic Impactor for CCI, Leica Microsystems) equipped with a metal piston using the following parameters: 3 mm tip diameter, 15° angle, depth 0.8 mm from the dura, velocity 3 m/s, and dwell time 100 ms. Sham animals received identical anesthesia and craniotomy, but the injury was not delivered.

### **Immunostaining and microscopy**

We anesthetized mice with a lethal dose of Fatal-Plus and perfused with 4% paraformaldehyde in 1X PBS. Serial coronal sections (30 µm thick) were cut on a Leica SM2000R sliding microtome. Sections were incubated with antibodies directed against GFAP (1:1000, chicken, Abcam, ab4674, AB\_304558), NeuN (1:500, mouse, Millipore, MAB377, AB\_2298772), and CD31 (1:125, rat, BD Pharmingen, 550274) overnight at 4°C. After wash, we incubated sections with Alexa Fluor-conjugated secondary antibodies (1:300, Thermo Fisher Scientific, A-11029) for two hours at room temperature. We mounted sections in an antifade medium (Vectashield) and imaged using a Bioevo BZ-9000 Keyence microscope at 10-20x.

### ***In vivo* electrophysiology and behavior**

Non-chronic electrophysiological recordings in freely behaving mice were performed as described using custom-made ECoG devices (Clemente-Perez et al., 2017; Ritter-Makinson et al., 2019). ECoG was recorded using RZ5 (TDT) and sampled at 1221 Hz. A video camera that was synchronized to the signal acquisition was used to continuously monitor the animals. We briefly anesthetized animals with 2% isoflurane at the start of each recording to connect for recording. Each recording trial lasted 15-60 min. To control for circadian rhythms, we housed our animals using a regular light/dark cycle, and performed recordings between roughly 9:00 am and 6:00 pm. All the recordings were performed during wakefulness. We validated the location of the electrodes by histology after euthanasia in mice that did not experience sudden death and whose brains we were able to recover and process.

### **Statistical analyses**

All numerical values are given as means and error bars are standard error of the mean (SEM) unless stated otherwise. Parametric and non-parametric tests were chosen as appropriate and were reported in figure legends. Data analysis was performed with MATLAB (SCR\_001622), GraphPad Prism 7/8 (SCR\_002798), ImageJ (SCR\_003070), and Spike2 (SCR\_000903).

### **Image analysis and cell quantification**

We selected regions of interest (ROIs) for S1, nRT, and VB from 10x Keyence microscope images opened in ImageJ (SCR\_003070). To ensure that each ROI covered the same area on the ipsilateral and contralateral sides of the injury site, the first ROIs were duplicated and repositioned over the opposite hemisphere. The image was then converted to 8-bit. The upper threshold was adjusted to the maximum value of 255, and the lower threshold was increased from 0 until the pixel appearance most closely matched the fluorescence staining from the original image. We used the same threshold boundaries for all sections with the same stain. An integrated density ratio was calculated for each brain region by dividing the ipsilateral integrated pixel density by the

contralateral integrated pixel density. The integrated density ratios from three sections per animal were averaged to get a single average ratio per brain area for each animal.

### **RA8 treatment**

RA8 was prepared in a stock of 30% polyethylene glycol 300 (PEG300) in PBS. To avoid affecting cortical lesion size, RA8 treatment began 24 hours after TBI, when mice received daily intraperitoneal injections of 40 mg/kg RA8 or vehicle (30% PEG300 in PBS) for two weeks.

## Figures

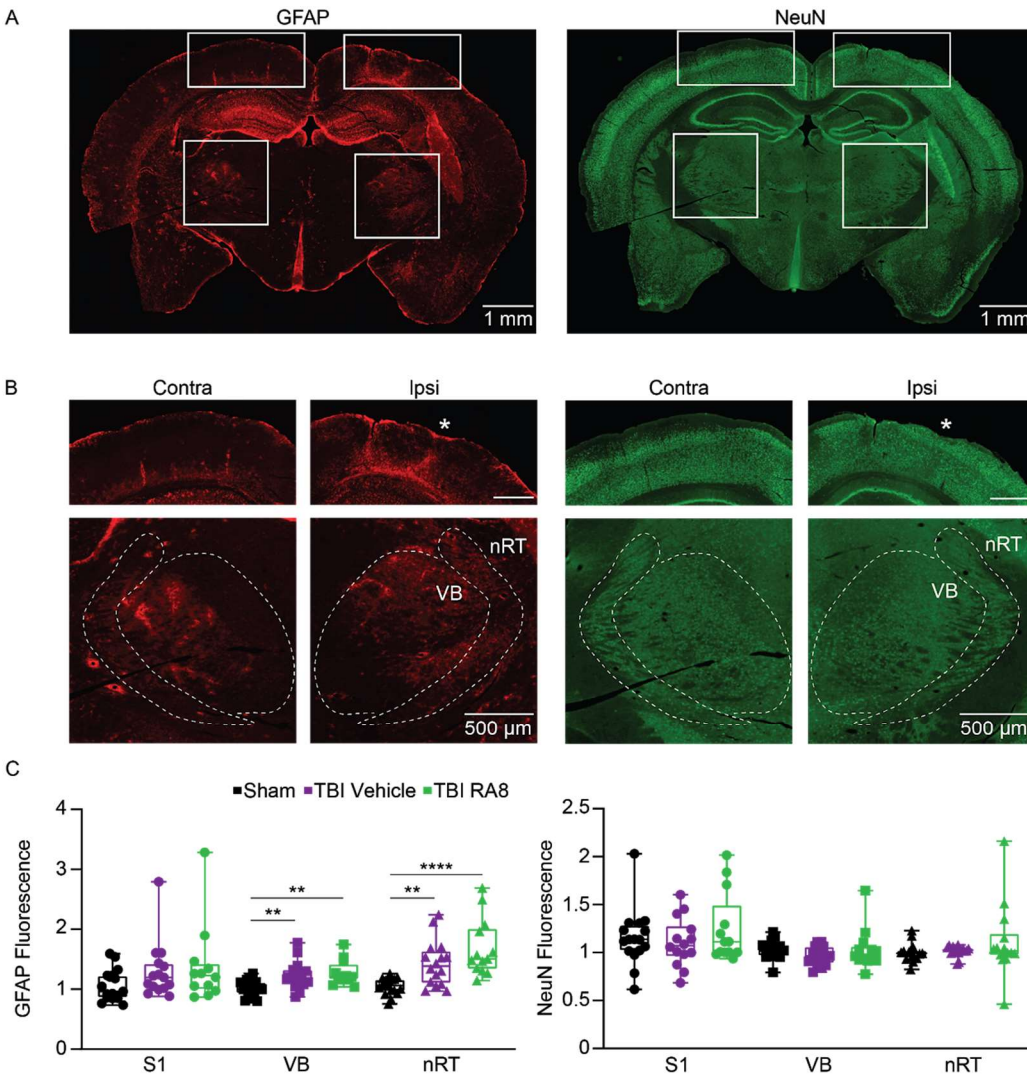


**Figure 3.1. Quantification of GFAP and NeuN fluorescence eight weeks after TBI.**

A, B) Representative coronal brain sections (A) and close-up images (B) of S1 (top), VB and nRT (bottom) stained for GFAP, a marker for astrocytes, and neuronal marker NeuN. Injury site in the right S1 cortex is marked by an asterisk. Scale bars, 1 mm (A), 500  $\mu$ m (B).

C) Quantification of fluorescence ratios between ipsilateral and contralateral regions in sham mice, vehicle-treated TBI mice, and RA8-treated TBI mice.

Data represent all points from min to max, with a Kruskal-Wallis test with multiple comparisons and  $\alpha = 0.05$  (\* $p < 0.05$ , \*\* $p < 0.01$ ). Analysis includes between 13 and 16 mice per group ( $n =$  three sections per mouse, one image per region).

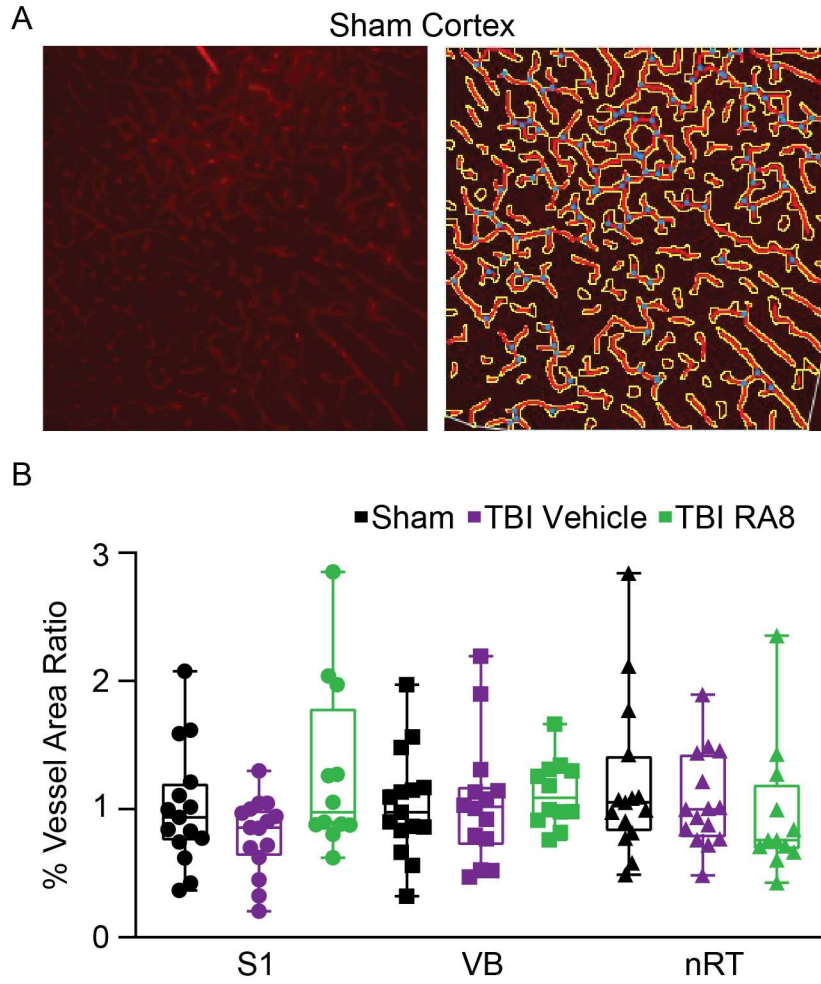


**Figure 3.2. Quantification of vascular density eight weeks after TBI.**

A) Representative close up of a section of the cortex from a sham mouse stained for CD31, a marker for endothelial cells (left) and analyzed for vessel density (right).

B) Quantification of vessel density ratios between ipsilateral and contralateral regions in sham mice, vehicle-treated TBI mice, and RA8-treated TBI mice.



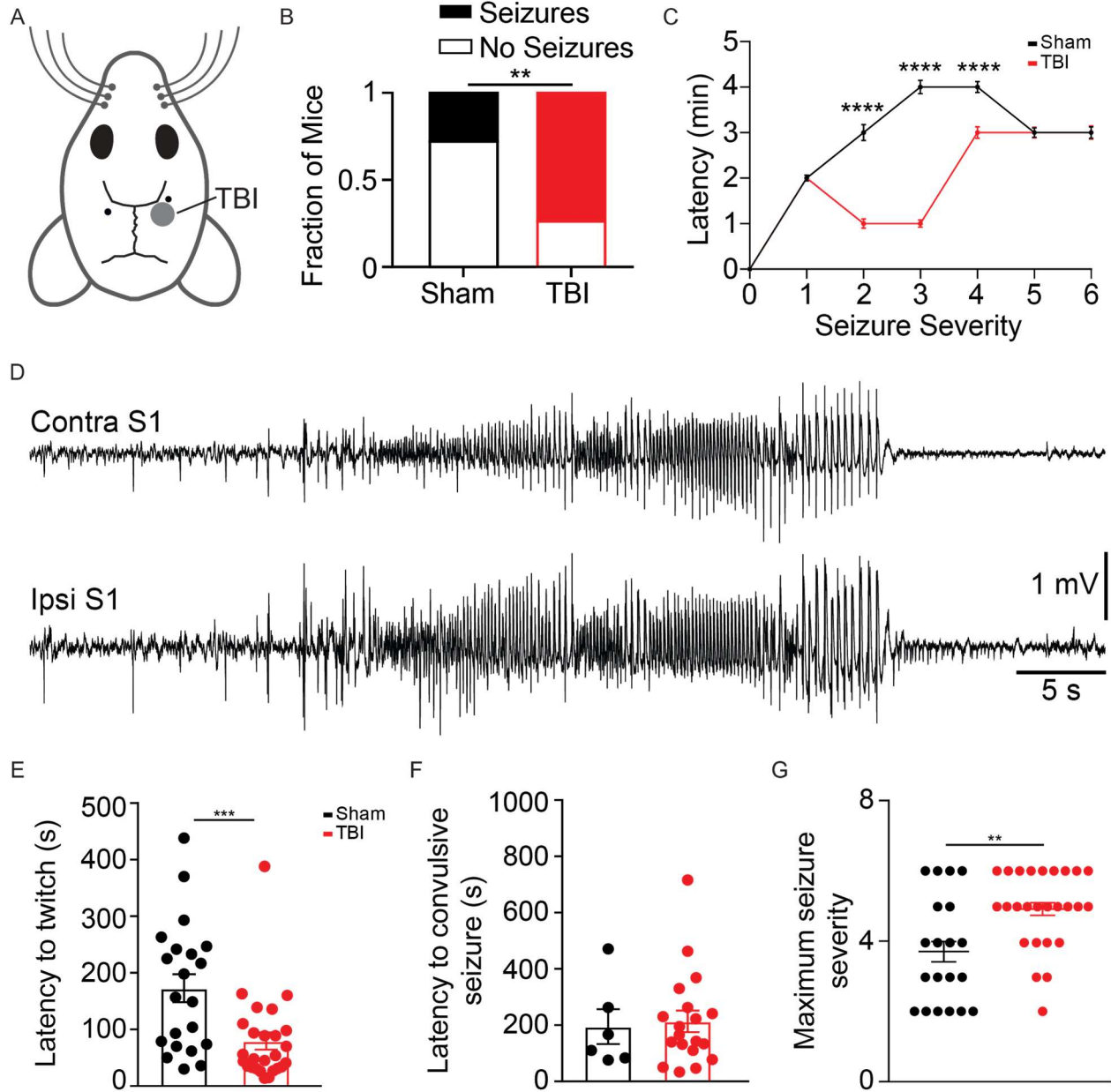


**Figure 3.3. Mice with TBI have higher PTZ-induced seizure susceptibility and reduced latency to myoclonic jerks three weeks after TBI.**

A) Diagram of recording locations for *in vivo* seizure susceptibility experiments. ECoG recording sites and TBI location are shown on the mouse skull.

B) Quantification of the proportion of 21 sham and 26 TBI mice that had a generalized tonic-clonic seizure induced by PTZ. Seizure outcome data represent the proportion of mice that did or did not have seizures, analyzed with a chi-square test (\*\* $p < 0.01$ ).

C) Latency to reach each stage of seizure severity after PTZ administration. PTZ-induced seizures between stages 2-4 occurred more rapidly in TBI mice than sham mice, analyzed with multiple t-tests (\*\*\*\* $p < 0.0001$ ).

D) Representative ECoG trace from a TBI mouse that had a PTZ-induced seizure.

E) Quantification of the latency to the first twitch/myoclonic jerk, as determined by video-EECoG recordings.

F) Quantification of the latency to the convulsive seizure, as determined by video-EECoG recordings.

G) Quantification of the maximum seizure severity reached after PTZ administration, analyzed with a Mann-Whitney test (\*\*p < 0.01).

Latency data represent mean  $\pm$  SEM analyzed with a Mann-Whitney test and  $\alpha = 0.05$  (\*\*p < 0.001). Analysis includes between six and 26 mice per group.

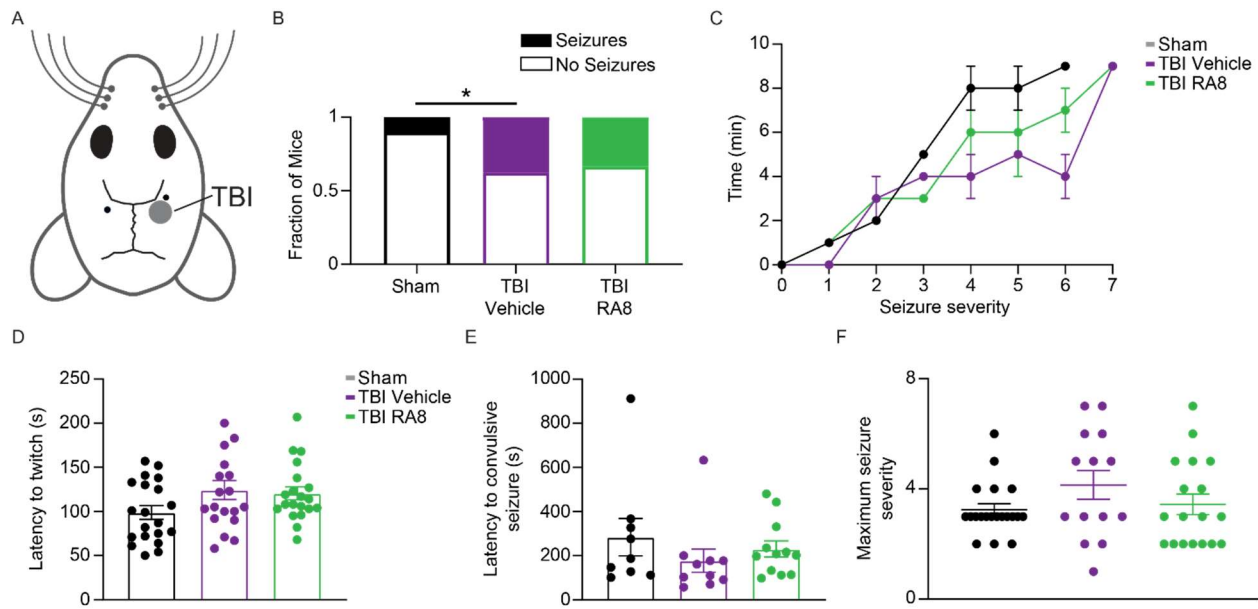


**Figure 3.4. Two-week treatment of RA8 does not alter seizure susceptibility six weeks after TBI.**

A) Diagram of recording locations for *in vivo* seizure susceptibility experiments. ECoG recording sites and TBI location are shown on the mouse skull.

B) Quantification of the proportion of 20 sham mice, 16 vehicle-treated TBI mice, and 18 RA8-treated TBI mice that had a generalized tonic-clonic seizure induced by 35 mg/kg PTZ. Seizure outcome data represent the proportion of mice that did or did not have seizures, analyzed with a chi-square test (\* $p < 0.05$ ).

C) Latency to reach each stage of seizure severity after PTZ administration.

D) Quantification of the latency to the first twitch/myoclonic jerk, as determined by video-ECoG recordings.

E) Quantification of the latency to the convulsive seizure, as determined by video-ECoG recordings.

F) Quantification of the maximum seizure severity reached after PTZ administration. Latency and seizure severity data represent mean  $\pm$  SEM analyzed with a Kruskal-Wallis test with multiple comparisons and  $\alpha = 0.05$ . Analysis includes between nine and 20 mice per group.

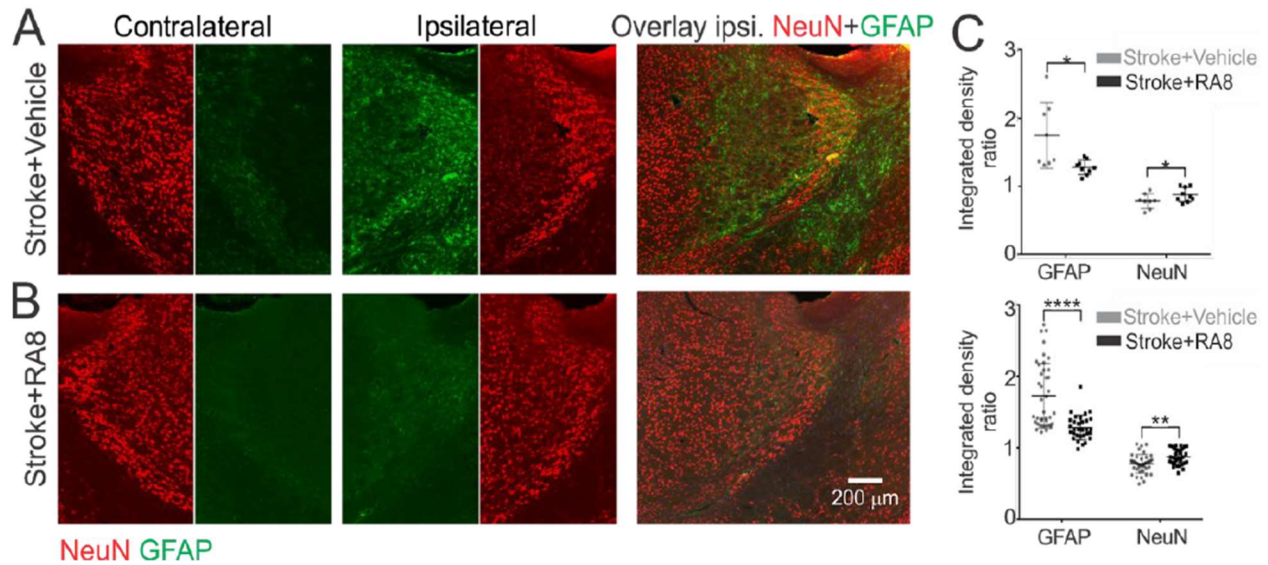


**Figure 3.S1. RA8 reduces neuronal loss in VB via suppression of astroglial reactivation in a mouse model of post-stroke epilepsy.**

A, B) NeuN and GFAP labeling in coronal thalamic sections from mice two weeks after cortical photothrombotic stroke with vehicle (A) or RA8 (B) i.p. treatment.

C) Quantification of integrated fluorescence density ratios (ipsilateral/contralateral) from eight vehicle-treated stroke mice and nine RA8-treated stroke mice (top) and from all brain sections (bottom).

Data were analyzed with a t-test (\* $p < 0.05$ , \*\* $p < 0.01$ , \*\*\* $p < 0.001$ , \*\*\*\* $p < 0.0001$ ). Analysis includes between eight and nine mice per group ( $n =$  three sections per mouse, one image per region).

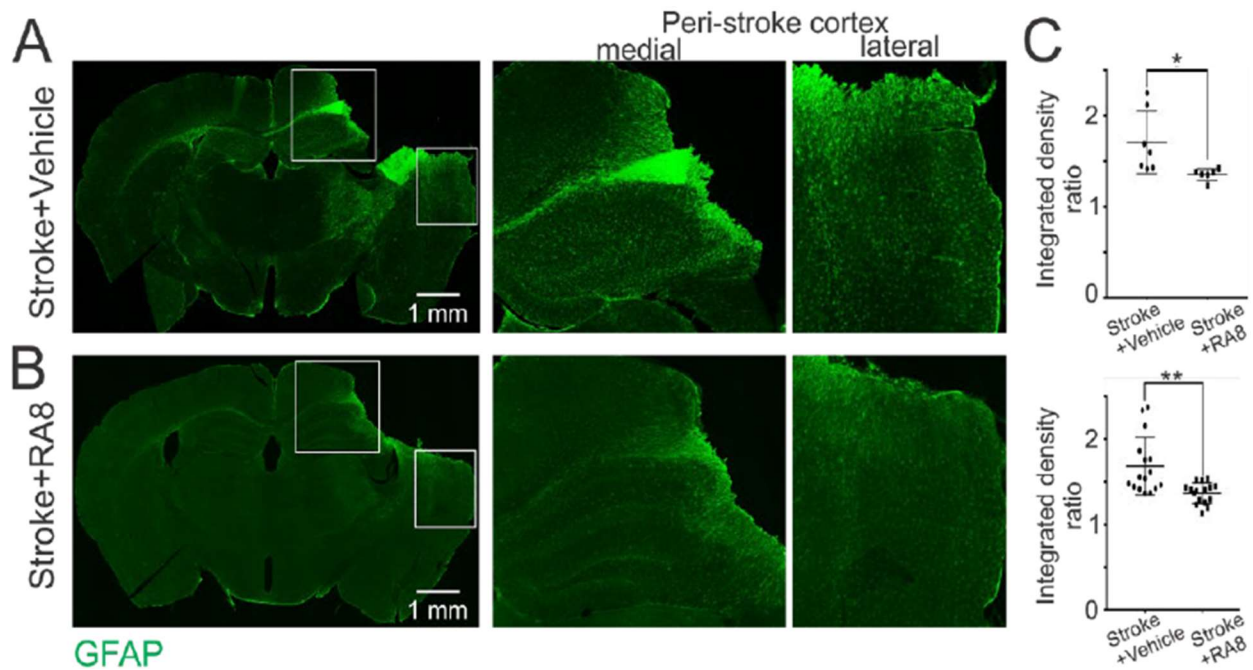


**Figure 3.S2. RA8 reduces long-term reactive astrogliosis in the peri-stroke cortex in a mouse model of post-stroke epilepsy.**

A, B) GFAP labeling in coronal brain sections from mice two weeks after cortical photothrombotic stroke and treatment with vehicle (A) or RA8 (B) i.p. treatment.

C) Quantification of GFAP integrated fluorescence density ratios (ipsilateral/contralateral) from seven vehicle-treated stroke mice and five RA8-treated stroke mice (top) and from all brain sections (bottom).

Data were analyzed with a t-test (\*p < 0.05, \*\*p < 0.01). Analysis includes between five and seven mice per group (n = three sections per mouse, one image per region).

## References

- Blecharz-Lang, K.G., Wagner, J., Fries, A., Nieminen-Kelhä, M., Rösner, J., Schneider, U.C., Vajkoczy, P., 2018. Interleukin 6-Mediated Endothelial Barrier Disturbances Can Be Attenuated by Blockade of the IL6 Receptor Expressed in Brain Microvascular Endothelial Cells. *Transl Stroke Res* 9, 631–642.
- Bolkvadze, T., Pitkänen, A., 2012. Development of post-traumatic epilepsy after controlled cortical impact and lateral fluid-percussion-induced brain injury in the mouse. *J. Neurotrauma* 29, 789–812.
- Bramlett, H.M., Dietrich, W.D., 2004. Pathophysiology of Cerebral Ischemia and Brain Trauma: Similarities and Differences. *J Cereb Blood Flow Metab* 24, 133–150.
- Burda, J.E., Bernstein, A.M., Sofroniew, M.V., 2016. Astrocyte roles in traumatic brain injury. *Exp. Neurol.* 275 Pt 3, 305–315.
- Carpentier, P.A., Begolka, W.S., Olson, J.K., Elhofy, A., Karpus, W.J., Miller, S.D., 2005. Differential activation of astrocytes by innate and adaptive immune stimuli. *Glia* 49, 360–374.
- Chen, Y., Swanson, R.A., 2003. Astrocytes and brain injury. *J. Cereb. Blood Flow Metab.* 23, 137–149.
- Chodobski, A., Zink, B.J., Szmydynger-Chodobska, J., 2011. Blood-brain barrier pathophysiology in traumatic brain injury. *Transl Stroke Res* 2, 492–516.

- Chou, A., Krukowski, K., Jopson, T., Zhu, P.J., Costa-Mattioli, M., Walter, P., Rosi, S., 2017. Inhibition of the integrated stress response reverses cognitive deficits after traumatic brain injury. *Proc. Natl. Acad. Sci. U.S.A.* 114, E6420–E6426.
- Clemente-Perez, A., Makinson, S.R., Higashikubo, B., Brovarney, S., Cho, F.S., Urry, A., Holden, S.S., Wimer, M., Dávid, C., Fenno, L.E., Acsády, L., Deisseroth, K., Paz, J.T., 2017. Distinct Thalamic Reticular Cell Types Differentially Modulate Normal and Pathological Cortical Rhythms. *Cell Rep* 19, 2130–2142.
- Glushakov, A.O., Glushakova, O.Y., Korol, T.Y., Acosta, S.A., Borlongan, C.V., Valadka, A.B., Hayes, R.L., Glushakov, A.V., 2018. Chronic Upregulation of Cleaved-Caspase-3 Associated with Chronic Myelin Pathology and Microvascular Reorganization in the Thalamus after Traumatic Brain Injury in Rats. *Int J Mol Sci* 19.
- Hayward, N.M.E.A., Immonen, R., Tuunanen, P.I., Nnode-Ekane, X.E., Gröhn, O., Pitkänen, A., 2010. Association of chronic vascular changes with functional outcome after traumatic brain injury in rats. *J. Neurotrauma* 27, 2203–2219.
- Hoane, M.R., Kaufman, N., Vitek, M.P., McKenna, S.E., 2009. COG1410 improves cognitive performance and reduces cortical neuronal loss in the traumatically injured brain. *J. Neurotrauma* 26, 121–129.
- Karve, I.P., Taylor, J.M., Crack, P.J., 2016. The contribution of astrocytes and microglia to traumatic brain injury. *Br J Pharmacol* 173, 692–702.

- Kim, J.-H., Min, K.-J., Seol, W., Jou, I., Joe, E.-H., 2010. Astrocytes in injury states rapidly produce anti-inflammatory factors and attenuate microglial inflammatory responses. *J. Neurochem.* 115, 1161–1171.
- Knobloch, S.M., Faden, A.I., 2002. Administration of either anti-intercellular adhesion molecule-1 or a nonspecific control antibody improves recovery after traumatic brain injury in the rat. *J. Neurotrauma* 19, 1039–1050.
- Lertkiatmongkol, P., Liao, D., Mei, H., Hu, Y., Newman, P.J., 2016. Endothelial functions of PECAM-1 (CD31). *Curr Opin Hematol* 23, 253–259.
- Liddel, S.A., Guttenplan, K.A., Clarke, L.E., Bennett, F.C., Bohlen, C.J., Schirmer, L., Bennett, M.L., Münch, A.E., Chung, W.-S., Peterson, T.C., Wilton, D.K., Frouin, A., Napier, B.A., Panicker, N., Kumar, M., Buckwalter, M.S., Rowitch, D.H., Dawson, V.L., Dawson, T.M., Stevens, B., Barres, B.A., 2017. Neurotoxic reactive astrocytes are induced by activated microglia. *Nature* 541, 481–487.
- Madathil, S.K., Carlson, S.W., Brelsfoard, J.M., Ye, P., D'Ercole, A.J., Saatman, K.E., 2013. Astrocyte-Specific Overexpression of Insulin-Like Growth Factor-1 Protects Hippocampal Neurons and Reduces Behavioral Deficits following Traumatic Brain Injury in Mice. *PLoS ONE* 8, e67204.
- Mattugini, N., Bocchi, R., Scheuss, V., Russo, G.L., Torper, O., Lao, C.L., Götz, M., 2019. Inducing Different Neuronal Subtypes from Astrocytes in the Injured Mouse Cerebral Cortex. *Neuron* 103, 1086-1095.e5.



Ritter-Makinson, S., Clemente-Perez, A., Higashikubo, B., Cho, F.S., Holden, S.S., Bennett, E., Chkhaidze, A., Eelkman Rooda, O.H.J., Cornet, M.-C., Hoebeek, F.E., Yamakawa, K., Cilio, M.R., Delord, B., Paz, J.T., 2019. Augmented Reticular Thalamic Bursting and Seizures in Scn1a-Dravet Syndrome. *Cell Rep* 26, 54-64.e6.

Simmons, D.L., Walker, C., Power, C., Pigott, R., 1990. Molecular cloning of CD31, a putative intercellular adhesion molecule closely related to carcinoembryonic antigen. *J. Exp. Med.* 171, 2147–2152.

Singleton, R.H., Yan, H.Q., Fellows-Mayle, W., Dixon, C.E., 2010. Resveratrol attenuates behavioral impairments and reduces cortical and hippocampal loss in a rat controlled cortical impact model of traumatic brain injury. *J. Neurotrauma* 27, 1091–1099.

Sofroniew, M.V., 2009. Molecular dissection of reactive astrogliosis and glial scar formation. *Trends Neurosci* 32, 638–647.

Zhang, L., Yin, J.-C., Yeh, H., Ma, N.-X., Lee, G., Chen, X.A., Wang, Y., Lin, L., Chen, L., Jin, P., Wu, G.-Y., Chen, G., 2015. Small Molecules Efficiently Reprogram Human Astroglial Cells into Functional Neurons. *Cell Stem Cell* 17, 735–747.

## **Chapter 4 : Conditional bistability, a generic cellular mnemonic mechanism for robust and flexible working memory computations**

### **Abstract**

Persistent neural activity, the substrate of working memory, is thought to emerge from synaptic reverberation within recurrent networks. However, reverberation models do not robustly explain the fundamental dynamics of persistent activity, including high-spiking irregularity, large intertrial variability, and state transitions. While cellular bistability may contribute to persistent activity, its rigidity appears incompatible with persistent activity's labile characteristics. Here, we unravel in a cellular model a form of spike-mediated conditional bistability that is robust and generic, and that provides a rich repertoire of mnemonic computations. Under asynchronous synaptic inputs of the awakened state, conditional bistability generates spiking/bursting episodes, accounting for the irregularity, variability, and state transitions characterizing persistent activity. This mechanism has likely been overlooked because of the subthreshold input it requires, and we predict how to assess it experimentally. Our results suggest a reexamination of the role of intrinsic properties of neurons in the collective network dynamics responsible for flexible working memory.

## Introduction

Working memory (WM), the ability to maintain and manipulate information within seconds, is essential to cardinal brain functions. Persistent neural activity represents a major neural correlate of WM, especially in the prefrontal cortex (PFC). The theory postulates that once triggered, persistent activity self-sustains through spiking reverberation in recurrent networks (Wang, 2001; Compte, 2006). Cortical architectures may provide sufficiently positive and nonlinear feedback for network dynamics to converge toward persistent activity (attractor dynamics; Cossart et al., 2003; MacLean et al., 2005). However, network reverberation as a unique causal origin remains controversial because it fails to robustly account for fundamental aspects of persistent activity such as the higher irregularity of spiking during the delay period of WM tasks, the large intertrial variability of the discharge and its temporal structure under quasi-stationary states, and the ability to encode parametric information (Seidemann et al., 1996; Koulakov et al., 2002; Compte et al., 2003; Goldman et al., 2003; Shafi et al., 2007; Barbieri and Brunel, 2008).

As a non-mutually exclusive alternative, intrinsic properties of neurons may underlie persistent activity, in addition to synaptic mechanisms, for object (Compte, 2006), spatial (Camperi and Wang, 1998), and parametric (Koulakov et al., 2002; Goldman et al., 2003) WM, and the interaction of WM with long-term memory (Egorov et al., 2002; Larimer and Strowbridge, 2010). The intrinsic bistability of neurons (i.e., the coexistence of stable states of quiescence and self-sustained spiking) is central to this proposal because it allows memorizing transient inputs in individual neurons (Booth and Rinzel, 1995; Delord et al., 1996, 1997; Marder and Calabrese, 1996; Shouval and Gavornik, 2011). Bistability is ubiquitous in peripheral (Lee and Heckman, 1998; Perrier and Tresch, 2005), subcortical (Rekling and Feldman, 1997; Kawasaki et al., 1999), and cortical (Krnjević et al., 1971; Schwindt et al., 1988; Silva et al., 1991; Tahvildari et al.,

2007; Zhang and Séguéla, 2010) structures, and in the PFC (Haj-Dahmane and Andrade, 1997; Dembrow et al., 2010; Gee et al., 2012; Thuault et al., 2013).

This hypothesis has been criticized because intrinsic bistability is generally strongly stereotyped *in vitro*: it does not depend on the level of background depolarization [absolute bistability (AB)], requires long on- and off-stimuli (seconds), strong levels of pharmacological manipulations (e.g., neuromodulation), and displays extremely long (tens of seconds), high-frequency, highly regular discharges with partially inactivated spikes (Haj-Dahmane and Andrade, 1997; Egorov et al., 2002; Tahvildari et al., 2007; Zhang and Séguéla, 2010; Gee et al., 2012). These rigid features contrast with the flexibility of WM-related computational processes and persistent activity [e.g., high intertrial variability (Shafi et al., 2007) and irregular spiking (Compte et al., 2003)].

However, non-stereotyped, conditional forms of bistability, where self-sustained spiking depends on background depolarization, have been found in the cortex (Silva et al., 1991; Tahvildari et al., 2007) and other structures (Bourque, 1986; Rekling and Feldman, 1997; Lee and Heckman, 1998; Kawasaki et al., 1999; Perrier and Tresch, 2005). Conditional bistability (CB) has been observed in layer V (L5) PFC pyramidal neurons (Thuault et al., 2013), which is not surprising, since bistability is underlain in these neurons by two spike-mediated (i.e., suprathreshold) currents—the high-threshold L-type calcium (CaL) and the calcium-activated nonspecific cationic (CAN) current (Haj-Dahmane and Andrade, 1997; Gee et al., 2012; Thuault et al., 2013)—that correlate with CB in many other neuronal types (Bourque, 1986; Silva et al., 1991; Rekling and Feldman, 1997; Lee and Heckman, 1998; Kawasaki et al., 1999; Perrier and Tresch, 2005; Tahvildari et al., 2007). A spike-mediated form of AB was previously studied (Shouval and Gavornik, 2011), but spike-mediated CB remains unexplored hitherto. Yet, its mechanism may depart from more classical spiking-independent forms of bistability relying on dendritic calcium (Hounsgaard and Kiehn, 1993; Booth and Rinzel, 1995), NMDA (Milojkovic et al., 2005; Major et al., 2008; Larimer and Strowbridge, 2010), or subthreshold currents (Delord et al.,

1996, 1997; Washburn et al., 2000; Genet and Delord, 2002; Loewenstein et al., 2005; Carrillo-Reid et al., 2009; Genet et al., 2010).

Here, we explore the computational and mnemonic consequences of spike-dependent CB in a model of a L5 PFC pyramidal neurons.

## Results

### Mimicking synaptic inputs during WM

Our main goal was to determine whether depolarizing spike-mediated currents can maintain the memory of an event at the level of the discharge of an individual neuron, while producing realistic spiking patterns, as observed during WM. To that end, we designed a realistic isopotential model of a L5 pyramidal PFC neuron endowed with high-threshold CaL ( $I_{CaL}$ ), calcium-activated nonspecific cationic ( $I_{CAN}$ ), afterhyperpolarization potassium ( $I_{AHP}$ ), action potential and leak currents, and intracellular calcium ( $[Ca^{2+}]$ ) linear dynamics (see Materials and Methods). In the model,  $I_{CaL}$  and  $I_{CAN}$  are spike-mediated because  $I_{CaL}$  activates at membrane potentials above the spike threshold and is the unique source of intracellular calcium activating  $I_{CAN}$ , as found in PFC neurons exhibiting spike-mediated bistability (Haj-Dahmane and Andrade, 1997). Parameters were set such that  $I_{CAN}$  was the sole spike-mediated charge carrier between these two currents (Haj-Dahmane and Andrade, 1997).

To test whether spike-mediated currents contribute to persistent activity in the model, we used two stimulation protocols. The event protocol, classically used to assess bistability, consisted of a single, short (0.2 s) suprathreshold current pulse mimicking the arrival of an input (e.g., perceptive or motor) event. In the event/delay protocol, the event was followed by a longer (1 s) subthreshold depolarizing current mimicking background activity from the PFC network to the neuron during the delay of a WM task. This input may correspond to persistent activity reverberating within local PFC recurrent connections to maintain information about the event or to ongoing inputs related to motivational, attentional, anticipatory, or executive aspects of WM processes.

### Conditional bistability is invisible with classical protocols

At low levels of the maximal CAN conductance ( $g_{CAN}$ ), the neuron discharged only during the event (**Figure 4.1a1**, event protocol), even when the event was followed by a background

subthreshold delay current (**Figure 4.1a2**, event/delay protocol). A bifurcation analysis as a function of the  $I_{inj}$  indicated that the neuron was monostable (M): it admitted either a stable fixed point corresponding to the resting potential (**Figure 4.1a3**, green solid curve) or, above the spiking threshold  $\theta_{ON}$ , to a stable limit cycle corresponding to rhythmic spiking (**Figure 4.1a3**, red solid curves).

At large  $g_{CAN}$  values, the event induced a self-sustained discharge that outlasted the triggering event, providing a cellular form of memory, with both protocols (**Figure 4.1b1**, 4.1b2). Mechanistically, self-sustained spiking arose from the positive feedback among spiking, CaL activation, increased  $[Ca^{2+}]$ , and CAN activation (**Figure 4.1b1**, red arrows), which did not operate at low  $g_{CAN}$  levels (compare with **Figure 4.1a1**). Here, the neuron was bistable: the resting potential coexisted with rhythmic spiking in a bistability domain situated between  $\theta_{ON}$ , the threshold for initiating spiking, and  $\theta_{OFF}$ , the threshold for terminating spiking (**Figure 4.1b3**, lavender domain). The bistability domain included  $I_{inj} = 0 \mu A \cdot cm^{-2}$  ( $\theta_{OFF} < 0 < \theta_{ON}$ ), so that cellular memory did not require any background subthreshold input. Hence, the spike-mediated bistability was absolute, as observed in a previous model (Shouval and Gavornik, 2011) and in PFC neurons under pharmacological manipulations (Dembrow et al., 2010; Gee et al., 2012). Therefore, persistent activity outlasted the delay period (**Figure 4.1b2**, star; i.e., memory was infinite), unless a specific inhibitory input terminated it.

At intermediate  $g_{CAN}$  levels, we observed that bistability was conditional: spiking during the delay depended on the level of subthreshold depolarization, as found in several neural structures and in the PFC (Bourque, 1986; Silva et al., 1991; Rekling and Feldman, 1997; Lee and Heckman, 1998; Kawasaki et al., 1999; Perrier and Tresch, 2005; Tahvildari et al., 2007; Thuault et al., 2013). After the event, spiking stopped in the event protocol (**Figure 4.1c1**) but persisted during the entire delay in the event/delay protocol (**Figure 4.1c2**) even though the background delay current ( $I_{inj-delay}$ ) was subthreshold (i.e., below  $\theta_{ON}$ ; **Figure 4.1c3**, black arrow). This was possible because  $I_{inj-delay}$  was above  $\theta_{OFF}$  (i.e., in the bistability domain;  $0 < \theta_{OFF} < \theta_{ON}$ ; **Figure 4.1c3**). The

background current was needed under CB, by contrast to AB, because the spike-mediated positive feedback was not sufficient to support autonomous self-sustained spiking at moderate  $g_{CAN}$  levels. This explains why persistent activity terminated at the end of the delay when  $I_{inj}$  values returned to zero, below  $\theta_{OFF}$  and the bistability domain (**Figure 4.1c2**, void symbol), being followed by an ADP (**Figure 4.1c2**, black arrow), as found in PFC neurons expressing spike-mediated currents and/or bistability (Haj-Dahmane and Andrade, 1997; Dembrow et al., 2010; Gee et al., 2012). Thus, under CB, the duration of cellular memory adapted to the duration of network memory (i.e., reverberation), alleviating the requirement for a dedicated inhibitory stimulus to terminate persistent activity. Note also that triggering spiking-dependent bistability did not require long stimulations, because of the moderate time constant of  $I_{CAN}$  ( $\sim 100$  ms; see Materials and Methods), as found in PFC neurons (Haj-Dahmane and Andrade, 1997).

### **CB induced by the event/delay protocol is robust**

To assess the robustness of CB mnemonic properties, we parametrically explored the model's response to the event/delay protocol (**Figure 4.2a**) as a function of  $I_{inj-delay}$  and  $g_{CAN}$ , which is important because the response reflects the regulation history of spike-mediated excitability and dictates the possible existence of CB (**Figure 4.1**). We found that CB existed in a large range of  $g_{CAN}$  values (**Figure 4.2a**, CB domain). Moreover, the ranges of CB and AB domains were much wider than M domains, indicating the prevalence of mnemonic properties with spike-mediated excitability in the model. We also found that cellular memory expressed differentially, depending on delay stimulation conditions. In the  $g_{CAN}$  range of CB, there was no firing during the delay at the lowest  $I_{inj-delay}$  values (i.e., discharge was memoryless; **Figure 4.2a**, yellow domain and trace). In contrast, delay firing was slowly decaying in a significant  $I_{inj-delay}$  range below  $\theta_{OFF}$ , underlying a transient memory (**Figure 4.2a**, orange), whereas above  $\theta_{OFF}$  a stable conditional memory was observed (compare **Figure 4.2a**, lavender, 4.1c). In addition, we observed a stable absolute memory (i.e., sustained activity without self-termination) in the range of AB



(compare **Figure 4.2a**, purple, **4.1b**). Under CB, memory typically lasted hundreds of milliseconds when transient (**Figure 4.2b**) and firing frequency was generally moderate (<50 Hz), in contrast to AB (**Figure 4.2c**). These results indicated that spike-mediated CB is robust, multiform, with long durations and low frequencies, which is consistent with persistent activity in the PFC during WM tasks (Compte, 2006). Moreover, parametrically, CB lies between M and AB, which have both largely been observed (Haj-Dahmane and Andrade, 1997; Dembrow et al., 2010; Gee et al., 2012). This suggests that CB, although observed occasionally in the PFC (Thuault et al., 2013), may have been mostly overlooked because the event/delay protocol, which is mandatory to reveal it, is almost never used in intracellular recordings.

### **CB generically emerges from spike-mediated excitability**

We wondered whether CB mnemonic properties were generic in essence, or specific to the model considered. Spike-mediated biophysical determinants—CaL and CAN current gating variables and the intracellular calcium  $[Ca^{2+}]$ —share a common dynamical trait. Their spike-triggered activation operates faster, compared with their relaxation time scale, during the ISI. This asymmetry produces interspike traces that form a memory after each spike, favoring the firing of the following spike and, in turn, self-sustained spiking. We tested whether the dynamic asymmetry of these determinants was essential to cellular memory. We found that considering fixed (i.e., voltage- or calcium-independent) time constants to suppress the dynamic asymmetry of the CaL, the CAN, or both currents had no effect on cellular memory (compare **Figure 4.3a-c**, **4.2a**), indicating that  $[Ca^{2+}]$  dynamic asymmetry was sufficient to support cellular memory. We also found that, in the absence of both calcium dynamics and the CAN current, CaL asymmetry alone was both sufficient (**Figure 4.3d**) and necessary (**Figure 4.3e**). Therefore, while cellular memory required the asymmetry between activation/relaxation time constants of a least one determinant, it was independent of its exact nature. This demonstrated that dynamic asymmetry was generic in underlying the positive feedback of spike-mediated CB. Remarkably, we found that CB

coexisted with marked ADP amplitudes ( $\sim 2.5$  to 15 mV) after spiking (**Figure 4.3f**, above horizontal lines), contrasting with the smaller ADP of monostable neurons ( $< 2.5$  mV).

### **CB mnemonic properties under *in vivo* conditions**

*In vivo*, PFC neurons continuously receive asynchronous synaptic inputs inducing strong membrane-potential fluctuations. These fluctuations may disrupt conditional memory, which relies on a minimal subthreshold depolarization. Thus, we assessed cellular memory with stochastic synaptic excitatory (AMPA) and inhibitory (GABA<sub>A</sub>) inputs driving fluctuations as found *in vivo* in the PFC (i.e., several millivolts; Fellous et al., 2003). Here, we tested the response of the neuron to the protocols considered *in vitro* and to a delay protocol (i.e., devoid of event). The latter was used as a control, since stochasticity may induce spiking during the subthreshold delay input. We found that at  $g_{CAN}$  levels providing CB *in vitro*, the neuron responded *in vivo* to the event/delay protocol with a persistent activity (**Figure 4.4a**, right) that was absent after the event protocol (left) and initially weaker during the delay protocol (middle). As a general rule, activity included episodes during which spikes clustered in bursts and spike-mediated currents were significantly activated (**Figure 4.4a**, lavender). During bursting episodes, the positive feedback characterizing CB ensured self-sustained spiking, which was irregular and terminated because of synaptic fluctuations. Bursting episodes alternated with non-bursting episodes essentially characterized by single spiking at lower frequency and smaller spike-mediated current activation (**Figure 4.4a**, yellow; i.e., during which the positive feedback was disengaged). A raster plot across trials (**Figure 4.4b**) illustrates stronger activity, a larger bursting propensity, and important variability in the temporal structure of the discharge during the event/delay protocol.

While firing slowly increased during the delay protocol (**Figure 4.4c**, fuschia) and rapidly decayed after the event protocol (**Figure 4.4c**, light blue), it persisted longer during the delay in the event/delay protocol (**Figure 4.4c**, lavender;  $T_{memory} \sim 900$  ms), with a frequency exceeding the sum of firing frequencies triggered by event or delay inputs alone (**Figure 4.4c**, salmon). Thus, persistent activity is an emergent property arising from nonlinear interactions between spike-

mediated currents and the delay background input. Persistent activity with  $T_{\text{memory}}$  in the range of hundreds of milliseconds to seconds (i.e., consistent with WM) was robustly evoked for a large domain of event input parameters (**Figure 4.4d**) and a thinner domain of the delay input parameters (**Figure 4.4e**). Large  $T_{\text{memory}}$  values were observed when the event was stronger than the delay (**Figure 4.4d**, right part of the map), with persistent activity decaying during the delay (**Figure 4.4c**, lavender).

Mechanistically, the excitation provoked by the event favored the rapid engagement of the positive feedback during the delay, as reflected by the strong synchronization of the onset of the first bursting episode across trials (**Figure 4.4f**). This first episode displayed a larger recruitment of spike-mediated currents (**Figure 4.4g**) and an increased duration (**Figure 4.4h**) and frequency (**Figure 4.4i**), compared with the following bursting episodes. As a result, the probability of being in a bursting episode (i.e., at a higher firing frequency) remained high at the beginning of the delay and progressively decreased toward its steady state (**Figure 4.4j**), accounting for the decreasing pattern of firing frequency (**Figure 4.4c**, lavender). Note that the instantaneous firing frequency remained globally constant within episodes (i.e., the discharge was quasi-stationary; **Figure 4.4k**).

### **CB promotes irregular discharge under *in vivo* conditions**

In WM tasks, spiking irregularity is larger during the delay than during stimulus presentation (i.e., event; Compte et al., 2003), with a higher coefficient of variation (CV) of ISIs over 1 and a  $CV_2$  (a version of CV based on successive ISIs) of  $\sim 1$ , which has been difficult to reproduce robustly in theoretical models (Barbieri and Brunel, 2008). In our model, irregularity was generally higher during the delay, compared with the event (**Figure 4.5a, b**, dots above first bisector), independently of whether neurons were M (**Figure 4.5a, b**, no  $I_{\text{CAN}}$ , black dots) or CB (**Figure 4.5a, b**, colored dots). Indeed, at a given similar firing mean frequency, the longer delay (2.5 s) allowed longer ISIs that could not occur during the shorter event (0.5 s). Thus, during the event, the sampling of the ISI distribution was truncated at low frequencies, and the apparent ISI variance

was therefore decreased, compared with the delay. This effect was moderate for M neurons (**Figure 4.5a, b**, black dots), but it dramatically increased for CB neurons firing at low frequency (<15 Hz; **Figure 4.5a, b**, colored dots), since, in the latter neurons, alternations of bursting episodes (with smaller ISIs) and non-bursting episodes (with larger ISIs) strongly increased the variance of the ISI distribution during the delay. At such low-frequency firing, the CV was largely >1 and the  $CV_2$  was  $\sim 1$ , as found during WM delays (Compte et al., 2003). Moreover,  $CV/CV_2$  culminated for inputs leading to intermediate memory time constants in the range of  $\sim 400$ – $600$  ms (**Figure 4.5c, d**) and transition frequencies between episodes at  $\sim 1$  Hz (color code). In these conditions, both the CV and  $CV_2$  were significantly larger during the delay (**Figure 4.5e, f**, thick black trace), compared with the event (**Figure 4.5e, f**, thin black trace). Remarkably, consistent with data (Compte et al., 2003), the CV distribution during the delay was broadened, compared with that during the event, which did not occur for the  $CV_2$ .

To fully confirm the genuine effect of depolarizing spike-mediated currents on spiking irregularity, we compared  $CV/CV_2$  with and without CB (1) upon stationary stimuli to avoid the interference of frequency time variations due to the protocol and (2) at identical mean firing frequencies to avoid the nontrivial effects of frequency on these measures (Compte et al., 2003). In these conditions, where computing these observables admits its plain significance, we found that, compared with M neurons (**Figure 4.5g**, black), the CV was systematically superior in CB neurons (**Figure 4.5g**, lavender) < 20 Hz and was >1 below 10 Hz. In CB neurons, the  $CV_2$  was also superior below 2 Hz, situated at  $\sim 1$ , whereas it was essentially similar to M neurons >2 Hz (**Figure 4.5h**). Thus, although the mean local irregularity measured by the  $CV_2$  was the same on average (because local increases of frequency regularity within bursting episodes compensated for the local frequency irregularities at transitions between bursting and non-bursting episodes), we found that the global irregularity of the discharge (measured by the CV; i.e., the normalized ISI SD) was increased in CB neurons due to the presence of spike-mediated currents.

## Discussion

Here, we show that spike-mediated CaL and CAN currents of L5 pyramidal PFC neurons (Haj-Dahmane and Andrade, 1997; Gee et al., 2012; Thuault et al., 2013) support CB. Moreover, our study suggests that CB is prevalent for several reasons. First, CB relies on suprathreshold mechanisms that are ubiquitous in pyramidal PFC neurons and operate robustly, independent of biophysical details, which are generic. Second, CB parametrically situates between M and AB regimes, both extensively observed in the PFC and other areas (Krnjević et al., 1971; Schwindt et al., 1988; Yang et al., 1996; Haj-Dahmane and Andrade, 1997; Dembrow et al., 2010; Zhang and Séguéla, 2010; Gee et al., 2012). AB is often observed under strong neuromodulatory manipulation that upregulates depolarizing spike-triggered conductances, yielding unrealistic stereotyped discharges inconsistent with WM firing patterns (Compte et al., 2003; Shafi et al., 2007). This suggests that neuromodulation regulates conductances below the range for AB in behaving animals. Below AB, the probability of being in CB is largely predominant (a much wider range than M; **Figure 4.2a**). Moreover, minimal neuromodulation is crucial for optimal PFC computations (Wang et al., 2007), whereas M lies at the lowest neuromodulation (conductance) levels. Thus, CB is likely encountered in PFC pyramidal neurons under physiological neuromodulatory levels. Third, we show that ADP represents a generic marker distinguishing CB from M neurons. ADPs are ubiquitous across L5 PFC pyramidal types (Yang et al., 1996; Haj-Dahmane and Andrade, 1997) and share specific common features with CB neurons (>5 mV; durations up to ~100 ms, occurrence even at low frequencies, CAN/calcium dependence; Yang et al., 1996; Haj-Dahmane and Andrade, 1997; Boudewijns et al., 2013), suggesting that PFC neurons displaying ADP are conditionally bistable. Hence, CB was observed without artificial pharmacological activation in L5 PFC pyramidal neurons with prominent ADPs (Thuault et al., 2013). Altogether, these lines of evidence indicate that CB likely constitutes a prevalent property in PFC L5 pyramidal neurons in physiological conditions during WM tasks.

So, why has CB remained scarce in the PFC? CB requires a triggering suprathreshold input followed by a subthreshold input (or applied upon a depolarized subthreshold holding potential). Therefore, CB neurons are undetectable using the classic protocol ubiquitously used, which consists of a single suprathreshold input applied from the resting potential. Consequently, neurons can be categorized as M (**Figure 4.1c1**), while actually displaying genuine CB (**Figure 4.1c2**). Such misclassification should be frequent given the much larger CB domain (compared with M), and systematically applying event/delay protocols should unravel CB in a significant fraction of neurons. Remarkably, event/delay protocols are meaningful physiologically, mimicking the temporal profile of inputs during WM: a strong behaviorally relevant (e.g., perceptive) signal followed by a lower background input during the delay (e.g., reverberating persistent activity or WM-related feedforward inputs).

Information maintenance in CB neurons relies on the asymmetry between fast buildup/activation and slower relaxation/deactivation dynamics of spike-activated mechanisms. This asymmetry maintains spike-to-spike excitability through the positive feedback between depolarization and suprathreshold activation. Noticeably, the slow CAN deactivation time constant of  $\sim 100$  ms (Haj-Dahmane and Andrade, 1997) allows the maintenance of self-sustained activity down to  $\sim 10$  Hz. Slower CAN in the PFC (Sidiropoulou et al., 2009) may support lower frequencies, at some expense (see below). Under asynchronous inputs, CB generates bursting/non-bursting episodes. Bursting episodes can be triggered by—and form a memory of—incoming events, when a background input follows the event. Statistically, this persistent activity fades at the second timescale across trials, consistent with WM, reflecting the stochastic disruption of bursting episodes due to synaptic fluctuations. By contrast, firing frequency is steady within bursting episodes, so that information maintenance is constant within individual trials for the duration of the first bursting episode.

Overall, the spike-mediated mechanism we unravel is robust to the exact nature and parameter values of the model and displays a much higher resistance to transient episodes of inhibition,

compared with subthreshold-based bistabilities (Washburn et al., 2000; Loewenstein et al., 2005; Carrillo-Reid et al., 2009). Sensitivity to inhibitory interference was used to discard the possible role of intrinsic bistability in maintaining persistent activity (Sanchez-Vives and McCormick, 2000; McCormick et al., 2003). Our results indicate that this reasoning does not apply to spike-mediated mechanisms, because they preserve resistance to inhibition, as does synaptic reverberation.

Previously described bistabilities are rigid, requiring strong/long stimuli to be turned on/off and producing long, high-frequency discharges primarily independent of the background input (Haj-Dahmane and Andrade, 1997; Egorov et al., 2002; Tahvildari et al., 2007; Zhang and Séguéla, 2010; Gee et al., 2012) By contrast, CB exhibits a rich repertoire of computational operations. It expresses as a memoryless discharge or subserve transient or stable conditional memory, depending on input parameters. Moreover, mnemonic activities can be initiated by short events because of the moderate CAN activation time constant (Haj-Dahmane and Andrade, 1997). Furthermore, the duration and frequency of mnemonic discharges are controlled by the delay input at low frequencies. Finally, under *in vivo*-like inputs, this diversity expresses as bursting/non-bursting episodes with variable frequencies and durations, resulting in a large variability of the discharge structure across trials, as found during WM (Shafi et al., 2007).

In response to asynchronous inputs, CB increases discharge irregularity, because smaller ISIs during bursting episodes and larger ISIs during non-bursting episodes increase the ISI distribution variance. The  $CV/CV_2$  are highest at low firing frequencies i.e., under excitation/inhibition balance, two factors increasing irregularity; Compte et al., 2003. In such conditions, the CV is  $>1$  and  $CV_2 \sim 1$  in CB neurons during the delay, being higher than during the event, as in WM (Compte et al., 2003), properties previous models are unable to account for robustly (Barbieri and Brunel, 2008). This effect happens in CB neurons, because bursting/non-bursting episodes can alternate during delays of several seconds, but not during shorter events (0.2 s).

Besides, while CB clearly increases the CV, its effect on the  $CV_2$  is mild. This results because whereas frequency changes at the transitions of episodes increase  $CV_2$ , the more regular discharge within bursting episodes decreases it. Synaptic inputs are not stationary *in vivo* (Shafi et al., 2007; Ostojic, 2014), which could explain the slightly higher  $CV/CV_2$  observed experimentally (Compte et al., 2003), compared with the situation reported here. This could also explain the larger difference in  $CV_2$  values between the delay and the event (Compte et al., 2003), as changes in the synaptic input rates have more time during the delay to exert their effect on successive ISIs and thus on the  $CV_2$ .

Interestingly, the overall increase in irregularity in CB neurons required an AHP current, which balanced the CAN current in the model (CAN alone decreased irregularity; data not shown). Finally, our conclusion that bursting/non-bursting alternations underlie irregularity is additionally supported by the finding that very slow CAN currents—driving very long bursts without alternations—decrease the CV (Sidiropoulou et al., 2009).

What roles may CB play at the network scale during maintenance? Here, CB requires a subthreshold constant background input from the network to memorize a transient event. However, inputs are not stationary in PFC networks and cellular CB should affect, in turn, network dynamics. Therefore, interactions between local cellular CB and global network recurrence may provide a rich repertoire of dynamics.

Hence, following an event, bursting in CB neurons may be sustained by the prolonged synaptic feedback due to bursting in other CB neurons. Such synergistic CB bursting recruitment may determine the extent to which activity is amplified and prolonged, possibly resulting in decaying, stable, or ramping temporal firing patterns of WM (Shafi et al., 2007). Synergy between CB neurons may also provide a realistic biophysical basis for WM of parametric information, which requires bistable elements to emerge robustly (Koulakov et al., 2002; Goldman et al., 2003). Such collective dynamics are plausible because CB is gradual in essence, by contrast to AB. WM-



related drives during the delay and the regulation state of synaptic strengths and spike-mediated excitability should be fundamental in setting the gradual synergetic recruitment of CB neurons. Within a recurrent network, CB neurons can discharge during the delay even when they have not received the event input, because of the subthreshold recurrent input provided by other neurons of the network actively maintaining the memory of that event (**Figure 4.4c**, fuschia curve). This could be problematic if presynaptic and postsynaptic neurons belong to different populations encoding distinct memories (i.e., Hebbian assemblies), as memory would “bleed over” across populations (i.e., memory interference). This problem may arise even with monostable postsynaptic neurons, although CB neurons would discharge at higher rates for a similar recurrent delay input, enhancing interference. However, different mechanisms have been imagined that may circumscribe interference between memory representations [e.g., mutual (Miller and Wang, 2006) or global (Brunel and Wang, 2001) inhibition between assemblies]. Besides, enhanced “bleeding” due to CB could also improve pattern completion within Hebbian assemblies, because the easier recruitment of CB neurons not activated by the event (because of incomplete input pattern presentation) would facilitate complete memory retrieval through associative synaptic reverberation.

Besides, during WM delays, PFC networks encounter transitions between stable collective states of quasi-stationary firing at the second timescale, reflecting mental states during the exploration of computational solutions, as cognitive processes wander from stimulus encoding to decision-making and action (Seidemann et al., 1996; Cossart et al., 2003). Bursting/non-bursting episodes in CB neurons share similar quasi-stationary firing and generate maximal irregularity at this timescale. We suggest that CB may promote the emergence of stable collective states and the complexity of PFC neuronal operations, providing a basis for exploring computational solutions during WM. Intrinsic plasticity and neuromodulation would represent strategic processes to regulate spike-mediated mechanisms for the emergence of adapted WM-related cognitive processes.

While CB relies on a weak spike-mediated positive feedback, it is precisely this “weakness” that underpins the computational richness and flexibility it brings, compared with what was previously thought. We suggest that the traditional view should be overcome in favor of a reconciling perspective whereby synaptic reverberation and conditional bistability concur with the emergence of the highly flexible persistent activity required for elaborating adaptive WM-related cognitive processes and intelligent behavior.

## Materials & Methods

### Design of the standard model

We consider an isopotential L5 PFC pyramidal neuron model that follows the Hodgkin–Huxley formalism. The neuron model is endowed with the leak ( $I_L$ ) and action potential (AP) currents ( $I_{Na}$ ,  $I_K$ ) and a synaptic ( $I_{Syn}$ , “*in vivo* condition”) or an injected ( $I_{Inj}$ , “*in vitro* condition”) input current. Depending on the hypothesis tested, the model also comprises one or more calcium- and/or voltage-dependent suprathreshold currents, generically denoted  $I_{ion}$ . These currents can be depolarizing ( $I_{CaL}$ ,  $I_{CAN}$ ) or hyperpolarizing [afterhyperpolarization potential potassium current ( $I_{AHP}$ )]. The standard version of the model comprises the following three currents:  $I_{ion} = I_{CaL} + I_{CAN} + I_{AHP}$ , with parameters described in the Parameter section (see below). The membrane potential evolves according to the following:

$$C \frac{dV}{dt} = -(I_L + I_{Na} + I_K + I_{ion} + I_{Syn}) + I_{Inj}. \quad (1)$$

### Leak current $I_L$ and action potential currents $I_{Na}$ and $I_K$

The leak current is written as follows:

$$I_L = g_L(V - V_L), \quad (2)$$

and AP currents are taken from a previous model we devised to reproduce spike currents of excitatory regular-spiking neocortical neurons (Naudé et al., 2012).

### High-threshold calcium current ( $I_{AHP}$ )

The CaL current is derived from Delord et al. (1997) and follows as:

$$I_{CaL} = \bar{g}_{CaL} x_{CaL}^2 (V - V_{CaL}), \quad (3)$$

where the activation  $x_{CaL}$  follows first-order kinetics:

$$\frac{dx_{CaL}}{dt} = \frac{x_{CaL}^\infty(V) - x_{CaL}}{\tau_{CaL}(V)}, \quad (4)$$

with a voltage-dependent time constant:

$$\tau_{CaL}(V) = 10^{\alpha_{CaL} + \beta_{CaL} V}, \quad (5)$$

with  $\alpha_{CaL}$  and  $\beta_{CaL}$  adapted to fit the time constant observed *in vitro* (Helton et al., 2005).

The activation follows:

$$x_{CaL}^{\infty}(V) = \left( 1 + \exp \frac{-(V - V_{1/2,CaL})}{K_{CaL}} \right)^{-1}, \quad (6)$$

where  $V_{1/2,CaL}$  and  $K_{CaL}$ , respectively, denote the half-activation potential and the e-fold slope of Boltzmann activation voltage dependence, and were estimated from the  $I$ - $V$  curve obtained *in vitro* (Helton et al., 2005).

### Calcium-activated nonspecific cation current ( $I_{CAN}$ )

The CAN current obeys the following:

$$I_{CAN} = \bar{g}_{CAN} x_{CAN}(V - V_{CAN}), \quad (7)$$

where the activation  $x_{CAN}$  follows first-order kinetics depending on the intracellular calcium concentration, as follows:

$$\frac{dx_{CAN}}{dt} = \frac{x_{CAN}^{\infty}(Ca) - x_{CAN}}{\tau_{CAN}(Ca)}, \quad (8)$$

with

$$\tau_{CAN}(Ca) = \frac{1}{\alpha_{CAN}Ca + \beta_{CAN}}, \quad (9)$$

and

$$x_{CAN}^{\infty}(Ca) = \frac{\alpha_{CAN}Ca}{\alpha_{CAN}Ca + \beta_{CAN}}, \quad (10)$$

where  $\alpha_{CAN}$  and  $\beta_{CAN}$ , respectively, denote activation and deactivation kinetic constants chosen to get significant activation in the micromolar range with time constants fitting those observed *in vitro* after large calcium influx in L5 PFC pyramidal neurons (i.e., ~35 ms in the range 5–10  $\mu$ M in the model and up to ~100 ms at lower  $[Ca^{2+}]$  during interspike intervals (ISIs; Haj-Dahmane and Andrade, 1997)).

### $I_{AHP}$

The AHP current modeled here corresponds to the SK potassium channel type and obeys the following:

$$I_{\text{AHP}} = \bar{g}_{\text{AHP}} x_{\text{AHP}}^2 (V - V_{\text{AHP}}), \quad (11)$$

where the activation  $x_{\text{AHP}}$  follows calcium-dependent first-order kinetics as follows:

$$\frac{dx_{\text{AHP}}}{dt} = \frac{x_{\text{AHP}}^{\infty}(Ca) - x_{\text{AHP}}}{\tau_{\text{AHP}}(Ca)}, \quad (12)$$

with

$$\tau_{\text{AHP}}(Ca) = \frac{1}{\alpha_{\text{AHP}}Ca + \beta_{\text{AHP}}}, \quad (13)$$

and

$$x_{\text{AHP}}^{\infty}(Ca) = \frac{\alpha_{\text{AHP}}Ca}{\alpha_{\text{AHP}}Ca + \beta_{\text{AHP}}}, \quad (14)$$

where  $\alpha_{\text{AHP}}$  and  $\beta_{\text{AHP}}$ , respectively, denote the activation and deactivation kinetic constants, fitted to account for the time constants of medium AHPs observed *in vitro* in L5 PFC pyramidal neurons (Villalobos et al., 2004; Faber and Sah, 2007).

### Calcium concentration dynamics

In the model, calcium concentration dynamics results from the inward influx due to  $I_{\text{CaL}}$  and from first-order buffering /extrusion (Haj-Dahmane and Andrade, 1997) as follows:

$$\frac{dCa}{dt} = -\frac{1}{2F} \frac{\text{Surf}}{\text{Vol}} I_{\text{CaL}} + \frac{Ca_0 - Ca}{\tau_{Ca}}, \quad (15)$$

where  $F$  is the Faraday constant,  $Ca_0$  is the basal intracellular calcium concentration,  $\tau_{Ca}$  is the buffering time constant, and the following:

$$\frac{\text{Surf}}{\text{Vol}} = r_1^{-1} \left( 1 - \frac{r_1}{r_0} + \frac{r_1^2}{3r_0^2} \right)^{-1}, \quad (16)$$

is the surface area-to-volume ratio of an idealized intracellular shell compartment of thickness  $r_1$  situated beneath the surface of a spherical neuron soma of radius  $r_0$ . Calcium dynamics possesses an intrinsic asymmetry resulting from the inward influx due to rapid increases of  $I_{\text{CaL}}$  and the slower first-order buffering process.

### Synaptic currents

In *in vivo* conditions (see Protocols), synaptic activity is simulated with fluctuating excitatory AMPA and inhibitory GABA<sub>A</sub> conductances as studied in L5 PFC pyramidal neurons (Destexhe and Paré, 1999), and the synaptic current is modeled as follows:

$$I_{\text{Syn}} = g_E(V - V_E) + g_I(V - V_I), \quad (17)$$

where  $V_E$  and  $V_I$  are the reversal potentials, and the fluctuating conductances  $g_E$  and  $g_I$  are given by two Uhlenbeck–Ornstein processes, as follows:

$$\frac{dg_E}{dt} = (g_E - g_{E0})/\tau_E + \sigma_E x_E(t), \quad (18)$$

$$\frac{dg_I}{dt} = (g_I - g_{I0})/\tau_I + \sigma_I x_I(t), \quad (19)$$

where  $\tau_E$  and  $\tau_I$  are the respective time constants of the temporal evolution of conductances,  $g_{E0}$  and  $g_{I0}$  are the mean conductances (that depend on the considered protocol),  $\sigma_E$  and  $\sigma_I$  are the SDs, and  $x_E(t)$  and  $x_I(t)$  are Gaussian stochastic processes with zero mean and unit SDs.

### Determination of afterdepolarization potential amplitudes

The amplitude of afterdepolarization potentials (ADPs) is determined using a specific stimulation protocol composed of a 15 ms phasic current of fixed amplitude set to elicit a single action potential. The ADP amplitude is calculated as the maximal membrane potential difference between conditions in the presence and the absence of the tested supralimiar current ( $I_{\text{CaL}}$ ,  $I_{\text{CAN}}$ , or both). This difference was calculated in a window starting 10 ms after the action potential peak (to avoid the influence of different action potential lengths due to the presence/absence of suprathreshold currents) and ending 1 s later, far after complete relaxation to resting potential.

### Standard model parameters

Unless indicated in figure legends, standard parameter values are as follows: for the leak current,  $g_L = 0.05 \text{ mS} \cdot \text{cm}^{-2}$ ,  $V_L = -70 \text{ mV}$ ; AP current parameters are as in a previous model that we developed of excitatory regular-spiking neocortical neurons (Naudé et al., 2012), with  $\bar{g}_{\text{Na}} = 24 \text{ mS} \cdot \text{cm}^{-2}$ ,  $V_{\text{Na}} = 50 \text{ mV}$ ,  $\bar{g}_K = 3 \text{ mS} \cdot \text{cm}^{-2}$ , and  $V_K = -90 \text{ mV}$ . For supralimiar ionic currents,

parameters are  $\bar{g}_{CaL} = 0.0045 \text{ mS} \cdot \text{cm}^{-2}$ ,  $V_{CaL} = 150 \text{ mV}$ ,  $V_{1/2,CaL} = -12 \text{ mV}$ ,  $K_{CaL} = 7 \text{ mV}$ ,  $\alpha_{CaL} = 0.6$ ,  $\beta_{CaL} = -0.02 \text{ mV}^{-1}$ ,  $\bar{g}_{CAN} = 0.025 \text{ mS} \cdot \text{cm}^{-2}$ ,  $V_{CAN} = 30 \text{ mV}$ ,  $\alpha_{CAN} = 0.0056 \mu\text{M}^{-1} \cdot \text{ms}^{-1}$  and  $\beta_{CAN} = 0.0125 \text{ ms}^{-1}$ ,  $\bar{g}_{AHP} = 0.2 \text{ mS} \cdot \text{cm}^{-2}$ ,  $V_{AHP} = -90 \text{ mV}$ ,  $\alpha_{AHP} = 0.05 \mu\text{M}^{-1} \cdot \text{ms}^{-1}$ , and  $\beta_{AHP} = 0.2 \text{ ms}^{-1}$ . Geometrical and intracellular calcium dynamics parameters are as follows:  $F = 96,500 \text{ mol} \cdot \text{s}^{-1} \cdot \text{A}^{-1}$ ,  $r_0 = 4 \mu\text{m}$ ,  $r_1 = 0.25 \mu\text{m}$ ,  $Ca_0 = 0.1 \mu\text{M}$ ,  $\tau_{Ca} = 100 \text{ ms}$ . Synaptic parameters are  $g_{E0,BACKGROUND} = 0.0325 \text{ mS} \cdot \text{cm}^{-2}$ ,  $g_{E0,EVENT} = 0.065 \text{ mS} \cdot \text{cm}^{-2}$ ,  $g_{E0,DELAY} = 0.040 \text{ mS} \cdot \text{cm}^{-2}$ , and independently of the period considered,  $\sigma_E = 0.0125 \text{ mS} \cdot \text{cm}^{-2}$ ,  $g_{I0} = 0.1 \text{ mS} \cdot \text{cm}^{-2}$ ,  $\sigma_I = 0.0075 \text{ mS} \cdot \text{cm}^{-2}$ ,  $\tau_E = 2.5 \text{ ms}$ ,  $\tau_I = 10 \text{ ms}$ ,  $V_E = 0 \text{ mV}$ , and  $V_I = -75 \text{ mV}$ .

### Numerical procedures

The models were numerically integrated using the forward Euler method with a  $1e^{-2} \text{ ms}$  time step. Bifurcation diagrams were obtained using the XPP software for qualitative analysis of dynamical systems (<http://www.math.pitt.edu/~bard/xpp/xpp.html>). Spikes were detected as a maximum of the membrane potential above  $-20 \text{ mV}$ .

In *in vitro* protocols, the behavior maps (see Figs. 2, 3) were built as follows: the discharge during a 10 s delay period was classified as (1) memoryless, when no spike occurred during the delay period or when one spike occurred at  $<25 \text{ ms}$  after the onset of the delay period; (2) transient memory, when an unstable discharge occurred during the delay period and lasted at least 25 ms after the delay period onset (to exclude cases where an ultimate spike is blown just after the phasic current pulse due to the activation of a fast sodium current in the last milliseconds of the phasic current pulse); and (3) stable memory, when the last spike of the discharge occurred after 9.5 s and the mean relative absolute difference between successive ISIs was  $<5\%$  during the last 2 s of the delay period.

In *in vivo* protocols, spikes were defined as belonging to a burst when they were part of a succession of at least three spikes with all ISIs  $<100 \text{ ms}$  (instantaneous frequencies  $>10 \text{ Hz}$ ). Other spikes were defined as not belonging to a burst [i.e., isolated spikes or doublet of spikes (with an intradoublet ISI inferior to 100 ms) that were separated from the rest of the spike train by

ISIs >100 ms]. Bursting episodes were defined as contiguous periods of time within which all spikes belonged to a burst. Non-bursting episodes were defined as the periods outside the bursting episodes. The choice of 100 ms as a cutoff ISI value was arbitrarily set to separate periods with frequency inferior to 10 Hz, which are typical of the spontaneous state of activity in the awake cortex from periods of activity taking part in coding (Destexhe et al., 2001). This exact value is not important to the conclusions drawn in the present study.

### **Statistical methods**

We used a two-tailed Wilcoxon rank-sum test to compare the medians of the CV distributions in the event and delay periods of the event/delay protocol, because the CV distributions were not normal, according to Kolmogorov–Smirnov goodness-of-fit hypothesis tests. A similar procedure was used to compare the medians of the CV<sub>2</sub> distributions in the event and delay periods of the event/delay protocol.



## Figures

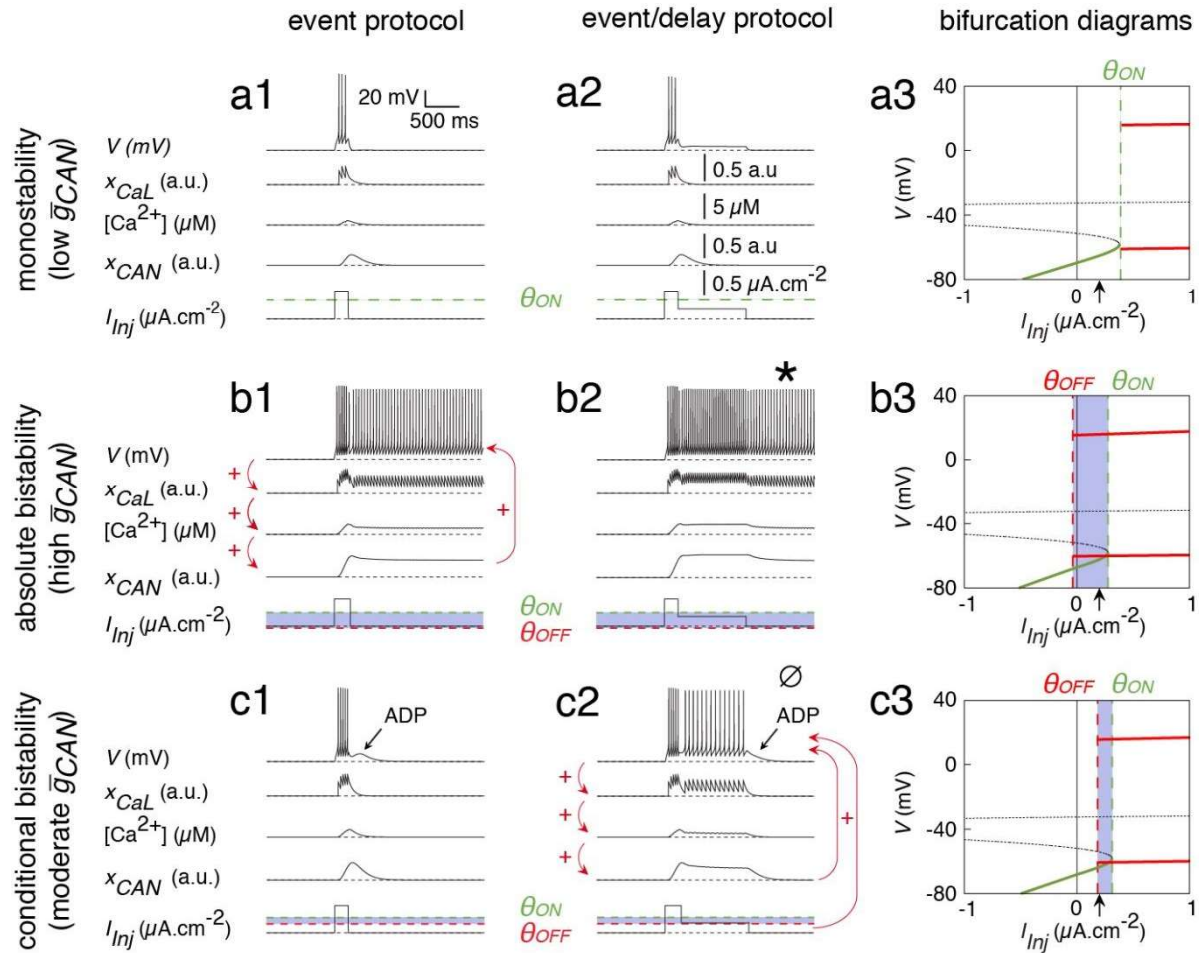


**Figure 4.1. Conditional bistability is a hidden property in neurons endowed with a supra-threshold conductance in response to standard protocols applied “in vitro”.**

Response of monostable (a;  $g_{CAN} = 0.003 \text{ mS.cm}^{-2}$ ), absolute bistable (b;  $g_{CAN} = 0.03 \text{ mS.cm}^{-2}$ ) and conditional bistable (c;  $g_{CAN} = 0.02 \text{ mS.cm}^{-2}$ ) neurons (standard model) to an *event protocol* with a 0.2 second supra-threshold current step (a1, b1, c1) and to the *event-delay protocol*, in which the event is followed by a 1 second sub-threshold depolarizing current mimicking background activity in PFC networks during the delay of a working memory task (a2, b2, c2). Note the afterdepolarization potential (ADP) following spiking in the conditional bistable neuron. The thresholds for initiating ( $\theta_{ON}$ ) and terminating ( $\theta_{OFF}$ ) spiking are represented as green and red dotted lines respectively, and the bistability domains are colored in lavender. Red arrows denote the positive feedback loop between spiking,  $CaL$  activation ( $x_{CaL}$ ), increased  $[Ca^{2+}]$  and  $CAN$  activation ( $x_{CAN}$ ). Right panels (a3, b3, c3): bifurcation diagrams illustrating the stable fixed point (resting potential, green solid curve) and the minimal/maximal potentials of action potentials during the limit cycle (rhythmic spiking, red solid curves), the thresholds for initiating ( $\theta_{ON}$ , green dotted lines) and terminating spiking ( $\theta_{OFF}$ , red dotted lines) and the background delay current during the delay ( $I_{Inj-delay}$ , black arrows). Bistability domains are colored in lavender. Black dotted lines indicate unstable fixed points of the models.

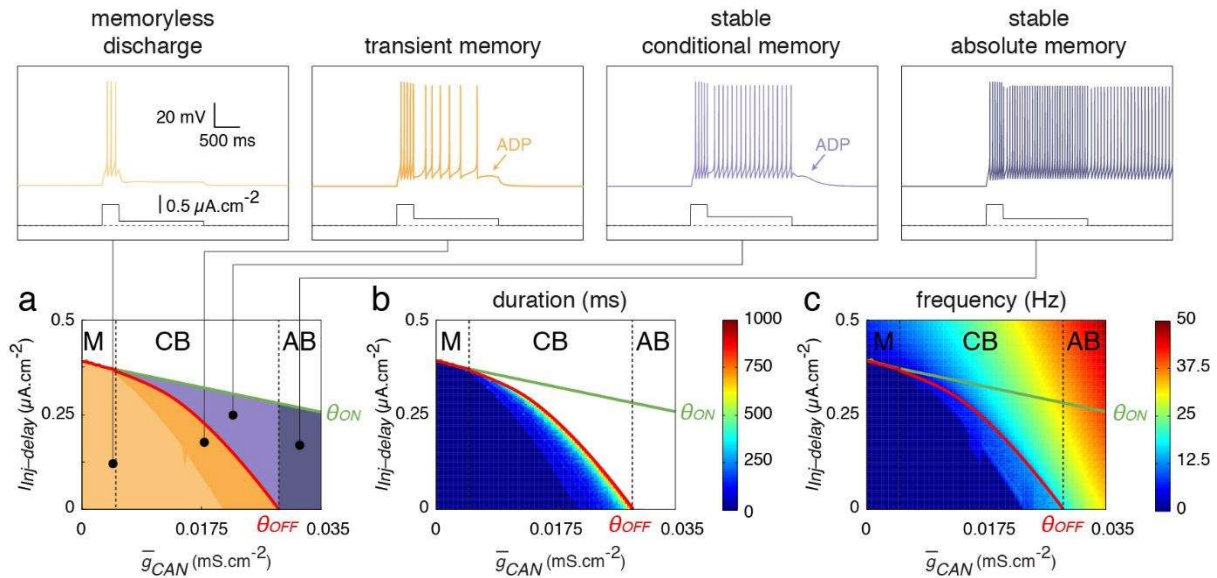


**Figure 4.2. Existence and expression of conditional bistability “in vitro”.**

(a) Discharge behaviors of the standard neuron model in response to the event/delay protocol ( $I_{inj-event} = 0.6 \mu A.cm^{-2}$ ) as a function of the maximal CAN conductance  $g_{CAN}$  and the background delay current  $I_{inj-delay}$ . M, CB and AB indicate the monostability, conditional bistability and absolute bistability domains, respectively. The memoryless and transient memory, stable conditional memory and stable absolute memory behaviors are respectively indicated as yellow, orange, lavender and purple domains (lower panel) and discharges (upper panels). (b, c) Heat maps of the duration of memoryless and transient memory behaviors (b) and of the mean firing frequency of stable memory behaviors (c) during the delay period, as a function of the maximal CAN conductance  $g_{CAN}$  and the background delay current  $I_{inj-delay}$ . Note that above  $\theta_{ON}$ , the tonic current is supra-threshold and the neuron fires even when no event precedes the delay period. Saw-teeth at the border between memoryless and transient regions occur due to the discretization of a continuous behavior: increasing the maximal CAN conductance leads to a single spike at more than 25 ms after the onset of the delay period (transient memory), then before 25 ms (memoryless), then several spikes before and after 25ms (transient memory). See the definition of transient memory behavior in *Methods*.

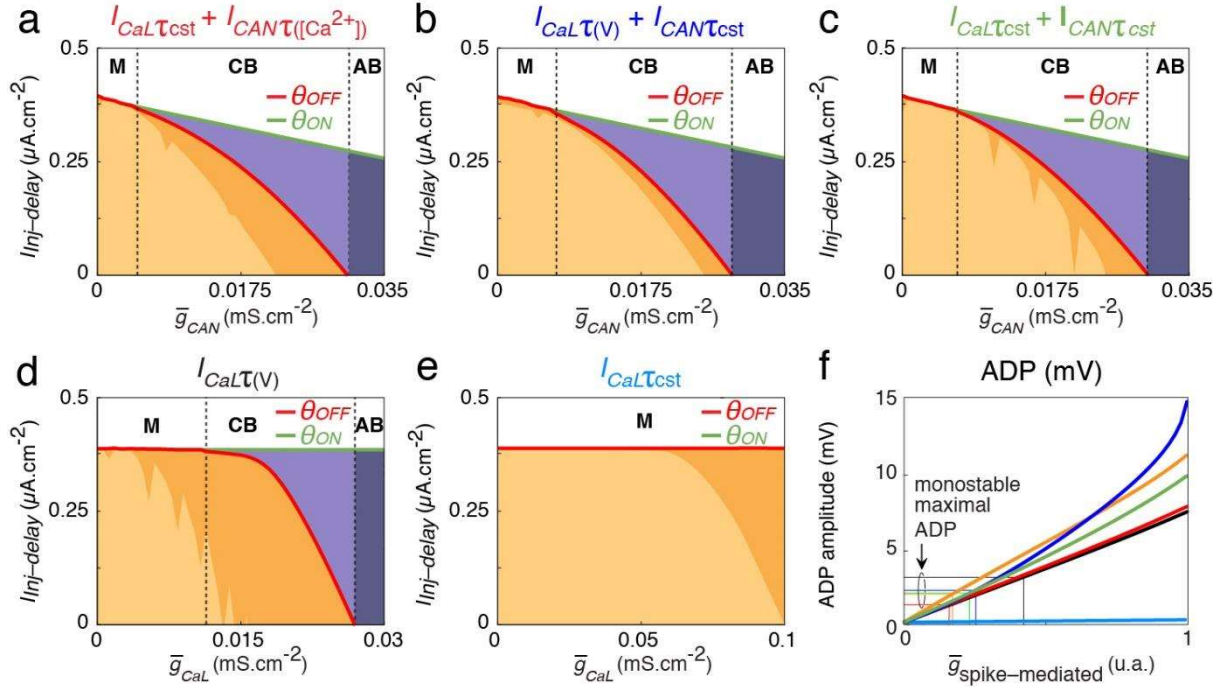


**Figure 4.3. Conditional bistability is a generic mnemonic property of neurons endowed with depolarizing spike-mediated mechanisms.**

Thresholds (a-e) for initiating ( $\theta_{ON}$ , green lines) and terminating spiking ( $\theta_{OFF}$ , red lines) for models with fixed (i.e. voltage- or calcium-independent) time constants suppressing the dynamic asymmetry of the CaL current (a), the CAN current (b) or both (c) or for models endowed with the sole CaL current with a voltage-dependent (d) or a fixed (e) time constant, as a function of the supra-threshold maximal conductance and background delay current. (f) ADP amplitudes of the five alternative models presented in (a-e). Line colors match the respective panel titles and the orange line applies to the standard model. Note that for ADP amplitudes (f) supra-threshold maximal conductances were normalized by the boundary value defining the transition between conditional and absolute bistability for each model. M, CB and AB indicate the monostability, conditional bistability and absolute bistability domains, respectively. Saw-teeth at the border between memoryless and transient regions occur due to the discretization of a continuous behavior: increasing the maximal CAN conductance leads to a single spike at more than 25 ms after the onset of the delay period (transient memory), then before 25 ms (memoryless), then several spikes before and after 25ms (transient memory). See the definition of transient memory behavior in *Methods*.

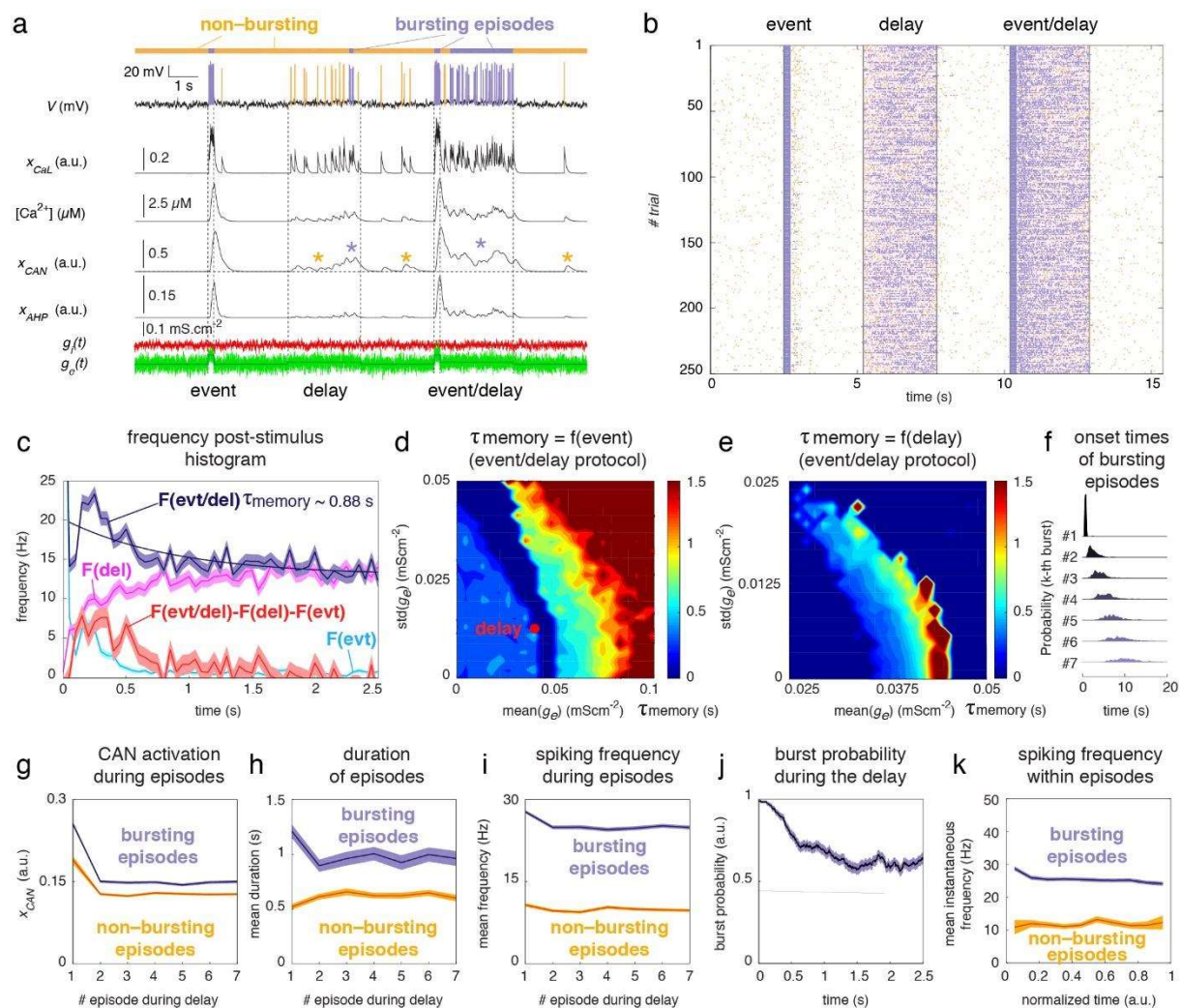


**Figure 4.4. Conditional bistability confers robust event memory under strongly fluctuating synaptic inputs “in vivo”.**

(a) Membrane-potential, CaL and CAN activation, calcium dynamics and AHP activation traces of the standard neuron model in response to the event, delay and event/delay protocols for a realization of the excitatory (green) and inhibitory (red) synaptic fluctuating conductances. Spikes belonging to bursting and non-bursting episodes are indicated in lavender and yellow, respectively. Small activation build-ups of spike-mediated currents during non-bursting episodes and larger build-ups during bursting episodes are signaled by yellow and lavender stars, respectively. See *Methods* for criteria that define bursting episodes. (b) Spike raster plot for 250 trials of the protocol depicted in (a), with different realizations of synaptic fluctuations. Color code as in (a). (c) Frequency poststimulus time histogram (PSTH) of the discharge (250 trials) after the onset of event (light blue), delay (fuschia) and event/delay (lavender) protocols; difference between the PSTH during the event/delay protocol and the sum of PSTHs during the event and delay protocols (salmon). Frequency means  $\pm$  standard error means are displayed. The memory time constant is defined as the time constant of firing frequency relaxation to its steady-state value in the event/delay protocol. (d) Memory time constant map of persistent activity, as a function of the mean and standard deviation of the excitatory fluctuating conductance of the event input during the event/delay protocol. The red dot indicates conductance parameters of the delay background input. When the event mean conductance is smaller than that of the delay input (left

part of the map), the activity builds up to the steady-state during the delay from the lower event-trigger initial frequency (e.g. pink curve in panel (c), for a null event mean conductance) and the time constant is smaller. (e) Memory time constant map of persistent activity, as a function of the mean and standard deviation of the excitatory fluctuating conductance of the delay input during the event/delay protocol. (d-e) Means across 100 trials; other synaptic parameters as in the standard model (see *Methods*). (f) Probability distribution of onset times of bursting episode as a function of their order of occurrence during the delay period (20 s) of the event/delay protocol, across 250 trials. (g-i) CAN conductance activation (g), mean duration (h) and mean spiking frequency (i) during bursting (lavender) and non-bursting (yellow) episodes, as a function of their order of occurrence during a delay period (20 s) in the event/delay protocol. Means  $\pm$  standard error mean across 250 trials. (j) Probability of being in a burst episode during the delay period (2.5 s) in the event/delay protocol. (k) Mean instantaneous spiking frequency as a function of the normalized time within bursting and non-bursting episodes (normalized time equals 0 at the beginning of episodes, 1 at their end). Means  $\pm$  standard error mean across 100 trials.

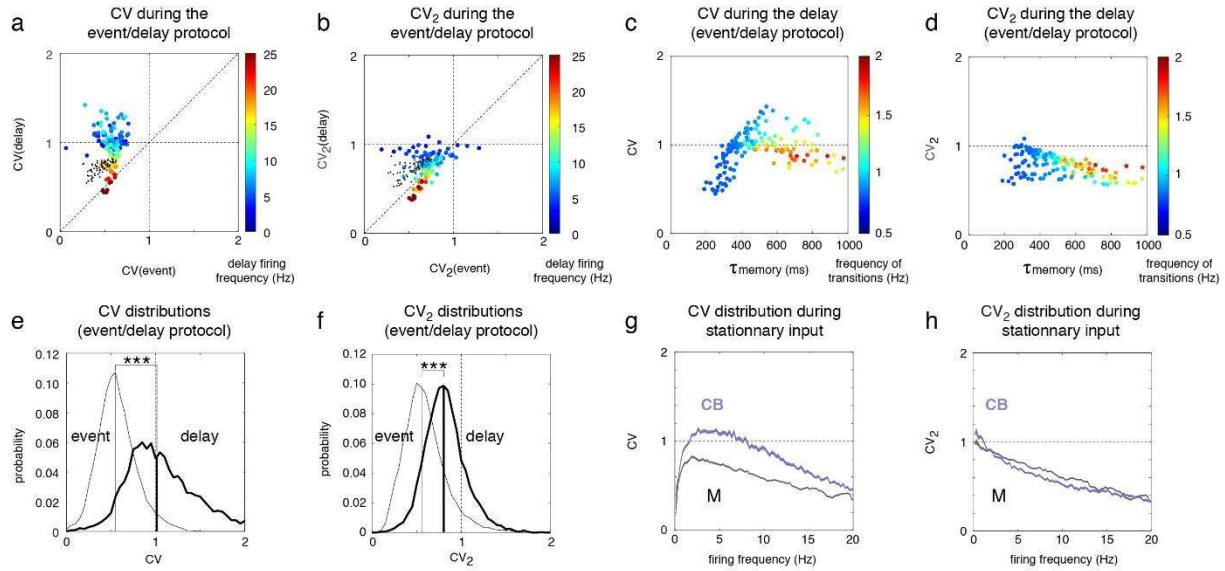


**Figure 4.5. Conditional bistability promotes irregular discharge under “in vivo” conditions.**

(a, b) CV (a) and  $CV_2$  (b) measures of the inter-spike interval (ISI) distribution of the discharge in monostable (black dots;  $g_{CAN} = 0 \text{ mScm}^{-2}$ ) and conditionally bistable (colored dots;  $g_{CAN} = 0.025 \text{ mScm}^{-2}$ ) neurons, in response to the input of an event protocol (x-axis) and to the 2.5 s delay input of an event/delay protocol (y-axis). The color code for conditionally bistable neurons indicates the firing frequency during the delay. Both inputs have the same excitatory input parameter taken in the ranges 0-0.05  $\text{mScm}^{-2}$  for the mean and 0-0.025  $\text{mScm}^{-2}$  for the standard-deviation, to limit the effect of firing frequency, which affects CV/ $CV_2$  measures in a non-trivial fashion (Compte, 2003). In both protocols, the event input lasts 0.5 s, as in reference (Compte, 2003). In the event/delay protocol, the event input has a 0.065  $\text{mScm}^{-2}$  mean and a 0.0125  $\text{mScm}^{-2}$  standard-deviation. (c, d) In the conditionally bistable neuron, the highest discharge irregularity during the delay, measured by the CV (c, y-axis) and the  $CV_2$  (d, y-axis) is observed at intermediate memory time constants ( $\sim 300\text{-}600 \text{ ms}$ ; x-axes) and frequencies of transitions between bursting and non-bursting episodes (color code). (e, f) At moderate memory time constants (400-600 ms), the means of CV (e) and  $CV_2$  (f) probability density functions during the delay are significantly higher in the CB neuron during the delay (thick black curve), compared to those during the event (thin black curve);  $p < 1e^{-9}$  on two-tailed Wilcoxon rank sum tests for both the CV and  $CV_2$  distributions (distributions were not normal, according to Kolmogorov-Smirnov goodness-of-fit hypothesis tests; for the CV distribution  $n_{event} = 29092$ ,  $n_{delay} = 5448$ , median( $CV_{event}$ ) = 0.5478 and median( $CV_{delay}$ ) = 1.0142; for the  $CV_2$  distribution  $n_{event} = 26755$ ,  $n_{delay} = 5345$ , median( $CV_{2,event}$ ) = 0.5634 and median( $CV_{2,delay}$ ) = 0.8043). (g, h) Irregularity of the discharge plotted as a function of firing frequency, for the conditionally bistable (lavender) and monostable neurons (black), in response to stationary synaptic inputs, as measured by the CV (g) and the  $CV_2$  (h).

## References

- Barbieri, F., Brunel, N., 2008. Can attractor network models account for the statistics of firing during persistent activity in prefrontal cortex? *Front Neurosci* 2, 114–122.
- Booth, V., Rinzel, J., 1995. A minimal, compartmental model for a dendritic origin of bistability of motoneuron firing patterns. *J Comput Neurosci* 2, 299–312.
- Boudewijns, Z.S.R.M., Groen, M.R., Lodder, B., McMaster, M.T.B., Kalogreades, L., de Haan, R., Narayanan, R.T., Meredith, R.M., Mansvelder, H.D., de Kock, C.P.J., 2013. Layer-specific high-frequency action potential spiking in the prefrontal cortex of awake rats. *Front Cell Neurosci* 7, 99.
- Bourque, C.W., 1986. Calcium-dependent spike after-current induces burst firing in magnocellular neurosecretory cells. *Neurosci. Lett.* 70, 204–209.
- Brunel, N., Wang, X.J., 2001. Effects of neuromodulation in a cortical network model of object working memory dominated by recurrent inhibition. *J Comput Neurosci* 11, 63–85.
- Camperi, M., Wang, X.J., 1998. A model of visuospatial working memory in prefrontal cortex: recurrent network and cellular bistability. *J Comput Neurosci* 5, 383–405.
- Carrillo-Reid, L., Tecuapetla, F., Vautrelle, N., Hernández, A., Vergara, R., Galarraga, E., Bargas, J., 2009. Muscarinic enhancement of persistent sodium current synchronizes striatal medium spiny neurons. *J. Neurophysiol.* 102, 682–690.

- Compte, A., 2006. Computational and in vitro studies of persistent activity: edging towards cellular and synaptic mechanisms of working memory. *Neuroscience* 139, 135–151.
- Compte, A., Constantinidis, C., Tegner, J., Raghavachari, S., Chafee, M.V., Goldman-Rakic, P.S., Wang, X.-J., 2003. Temporally irregular mnemonic persistent activity in prefrontal neurons of monkeys during a delayed response task. *J. Neurophysiol.* 90, 3441–3454.
- Cossart, R., Aronov, D., Yuste, R., 2003. Attractor dynamics of network UP states in the neocortex. *Nature* 423, 283–288.
- Delord, B., Klaassen, A.J., Burnod, Y., Guigon, E., 1996. An intrinsic bistable mechanism in neocortical pyramidal neurons might be involved in the generation of sustained discharge patterns related to working memory. *Neural Network World* 4, 525-533.
- Delord, B., Klaassen, A.J., Burnod, Y., Costalat, R., Guigon, E., 1997. Bistable behaviour in a neocortical neurone model. *Neuroreport* 8, 1019–1023.
- Dembrow, N.C., Chitwood, R.A., Johnston, D., 2010. Projection-specific neuromodulation of medial prefrontal cortex neurons. *J. Neurosci.* 30, 16922–16937.
- Destexhe, A., Paré, D., 1999. Impact of network activity on the integrative properties of neocortical pyramidal neurons in vivo. *J. Neurophysiol.* 81, 1531–1547.
- Destexhe, A., Rudolph, M., Fellous, J.M., Sejnowski, T.J., 2001. Fluctuating synaptic conductances recreate in vivo-like activity in neocortical neurons. *Neuroscience* 107, 13–24.



- Egorov, A.V., Hamam, B.N., Fransén, E., Hasselmo, M.E., Alonso, A.A., 2002. Graded persistent activity in entorhinal cortex neurons. *Nature* 420, 173–178.
- Faber, E.S.L., Sah, P., 2007. Functions of SK channels in central neurons. *Clin. Exp. Pharmacol. Physiol.* 34, 1077–1083.
- Fellous, J.-M., Rudolph, M., Destexhe, A., Sejnowski, T.J., 2003. Synaptic background noise controls the input/output characteristics of single cells in an in vitro model of in vivo activity. *Neuroscience* 122, 811–829.
- Gee, S., Ellwood, I., Patel, T., Luongo, F., Deisseroth, K., Sohal, V.S., 2012. Synaptic activity unmasks dopamine D2 receptor modulation of a specific class of layer V pyramidal neurons in prefrontal cortex. *J. Neurosci.* 32, 4959–4971.
- Genet, S., Delord, B., 2002. A biophysical model of nonlinear dynamics underlying plateau potentials and calcium spikes in purkinje cell dendrites. *J. Neurophysiol.* 88, 2430–2444.
- Genet, S., Sabarly, L., Guigon, E., Berry, H., Delord, B., 2010. Dendritic signals command firing dynamics in a mathematical model of cerebellar Purkinje cells. *Biophys. J.* 99, 427–436.
- Goldman, M.S., Levine, J.H., Major, G., Tank, D.W., Seung, H.S., 2003. Robust persistent neural activity in a model integrator with multiple hysteretic dendrites per neuron. *Cereb. Cortex* 13, 1185–1195.
- Haj-Dahmane, S., Andrade, R., 1997. Calcium-activated cation nonselective current contributes to the fast afterdepolarization in rat prefrontal cortex neurons. *J. Neurophysiol.* 78, 1983–1989.

- Helton, T.D., Xu, W., Lipscombe, D., 2005. Neuronal L-type calcium channels open quickly and are inhibited slowly. *J. Neurosci.* 25, 10247–10251.
- Hounsgaard, J., Kiehn, O., 1993. Calcium spikes and calcium plateaux evoked by differential polarization in dendrites of turtle motoneurons in vitro. *J. Physiol. (Lond.)* 468, 245–259.
- Kawasaki, H., Palmieri, C., Avoli, M., 1999. Muscarinic receptor activation induces depolarizing plateau potentials in bursting neurons of the rat subiculum. *J. Neurophysiol.* 82, 2590–2601.
- Koulakov, A.A., Raghavachari, S., Kepecs, A., Lisman, J.E., 2002. Model for a robust neural integrator. *Nat. Neurosci.* 5, 775–782.
- Krnjević, K., Pumain, R., Renaud, L., 1971. The mechanism of excitation by acetylcholine in the cerebral cortex. *J. Physiol. (Lond.)* 215, 247–268.
- Larimer, P., Strowbridge, B.W., 2010. Representing information in cell assemblies: persistent activity mediated by semilunar granule cells. *Nat. Neurosci.* 13, 213–222.
- Lee, R.H., Heckman, C.J., 1998. Bistability in spinal motoneurons in vivo: systematic variations in persistent inward currents. *J. Neurophysiol.* 80, 583–593.
- Loewenstein, Y., Mahon, S., Chadderton, P., Kitamura, K., Sompolinsky, H., Yarom, Y., Häusser, M., 2005. Bistability of cerebellar Purkinje cells modulated by sensory stimulation. *Nat. Neurosci.* 8, 202–211.

- MacLean, J.N., Watson, B.O., Aaron, G.B., Yuste, R., 2005. Internal dynamics determine the cortical response to thalamic stimulation. *Neuron* 48, 811–823.
- Major, G., Polsky, A., Denk, W., Schiller, J., Tank, D.W., 2008. Spatiotemporally graded NMDA spike/plateau potentials in basal dendrites of neocortical pyramidal neurons. *J. Neurophysiol.* 99, 2584–2601.
- Marder, E., Calabrese, R.L., 1996. Principles of rhythmic motor pattern generation. *Physiol. Rev.* 76, 687–717.
- McCormick, D.A., Shu, Y., Hasenstaub, A., Sanchez-Vives, M., Badoual, M., Bal, T., 2003. Persistent cortical activity: mechanisms of generation and effects on neuronal excitability. *Cereb. Cortex* 13, 1219–1231.
- Miller, P., Wang, X.-J., 2006. Power-law neuronal fluctuations in a recurrent network model of parametric working memory. *J. Neurophysiol.* 95, 1099–1114.
- Milojkovic, B.A., Radojicic, M.S., Antic, S.D., 2005. A strict correlation between dendritic and somatic plateau depolarizations in the rat prefrontal cortex pyramidal neurons. *J. Neurosci.* 25, 3940–3951.
- Naudé, J., Paz, J.T., Berry, H., Delord, B., 2012. A theory of rate coding control by intrinsic plasticity effects. *PLoS Comput. Biol.* 8, e1002349.
- Ostojic, S., 2014. Two types of asynchronous activity in networks of excitatory and inhibitory spiking neurons. *Nat. Neurosci.* 17, 594–600.

- Perrier, J.-F., Tresch, M.C., 2005. Recruitment of motor neuronal persistent inward currents shapes withdrawal reflexes in the frog. *J. Physiol. (Lond.)* 562, 507–520.
- Rekling, J.C., Feldman, J.L., 1997. Calcium-dependent plateau potentials in rostral ambiguous neurons in the newborn mouse brain stem in vitro. *J. Neurophysiol.* 78, 2483–2492.
- Sanchez-Vives, M.V., McCormick, D.A., 2000. Cellular and network mechanisms of rhythmic recurrent activity in neocortex. *Nat. Neurosci.* 3, 1027–1034.
- Schwindt, P.C., Spain, W.J., Foehring, R.C., Chubb, M.C., Crill, W.E., 1988. Slow conductances in neurons from cat sensorimotor cortex in vitro and their role in slow excitability changes. *J. Neurophysiol.* 59, 450–467.
- Seidemann, E., Meilijson, I., Abeles, M., Bergman, H., Vaadia, E., 1996. Simultaneously recorded single units in the frontal cortex go through sequences of discrete and stable states in monkeys performing a delayed localization task. *J. Neurosci.* 16, 752–768.
- Shafi, M., Zhou, Y., Quintana, J., Chow, C., Fuster, J., Bodner, M., 2007. Variability in neuronal activity in primate cortex during working memory tasks. *Neuroscience* 146, 1082–1108.
- Shouval, H.Z., Gavornik, J.P., 2011. A single spiking neuron that can represent interval timing: analysis, plasticity and multi-stability. *J Comput Neurosci* 30, 489–499.

- Sidiropoulou, K., Lu, F.-M., Fowler, M.A., Xiao, R., Phillips, C., Ozkan, E.D., Zhu, M.X., White, F.J., Cooper, D.C., 2009. Dopamine modulates an mGluR5-mediated depolarization underlying prefrontal persistent activity. *Nat. Neurosci.* 12, 190–199.
- Silva, L.R., Amitai, Y., Connors, B.W., 1991. Intrinsic oscillations of neocortex generated by layer 5 pyramidal neurons. *Science* 251, 432–435.
- Tahvildari, B., Fransén, E., Alonso, A.A., Hasselmo, M.E., 2007. Switching between “On” and “Off” states of persistent activity in lateral entorhinal layer III neurons. *Hippocampus* 17, 257–263.
- Thuault, S.J., Malleret, G., Constantinople, C.M., Nicholls, R., Chen, I., Zhu, J., Panteleyev, A., Vronskaya, S., Nolan, M.F., Bruno, R., Siegelbaum, S.A., Kandel, E.R., 2013. Prefrontal cortex HCN1 channels enable intrinsic persistent neural firing and executive memory function. *J. Neurosci.* 33, 13583–13599.
- Villalobos, C., Shakkottai, V.G., Chandy, K.G., Michelhaugh, S.K., Andrade, R., 2004. SKCa channels mediate the medium but not the slow calcium-activated afterhyperpolarization in cortical neurons. *J. Neurosci.* 24, 3537–3542.
- Wang, M., Ramos, B.P., Paspalas, C.D., Shu, Y., Simen, A., Duque, A., Vijayraghavan, S., Brennan, A., Dudley, A., Nou, E., Mazer, J.A., McCormick, D.A., Arnsten, A.F.T., 2007. Alpha2A-adrenoceptors strengthen working memory networks by inhibiting cAMP-HCN channel signaling in prefrontal cortex. *Cell* 129, 397–410.
- Wang, X.J., 2001. Synaptic reverberation underlying mnemonic persistent activity. *Trends Neurosci.* 24, 455–463.

Washburn, D.L., Anderson, J.W., Ferguson, A.V., 2000. A subthreshold persistent sodium current mediates bursting in rat subfornical organ neurones. *J. Physiol. (Lond.)* 529 Pt 2, 359–371.

Yang, C.R., Seamans, J.K., Gorelova, N., 1996. Electrophysiological and morphological properties of layers V-VI principal pyramidal cells in rat prefrontal cortex in vitro. *J. Neurosci.* 16, 1904–1921.

Zhang, Z., Séguéla, P., 2010. Metabotropic induction of persistent activity in layers II/III of anterior cingulate cortex. *Cereb. Cortex* 20, 2948–2957.

## **Chapter 5 : Conclusion & Future Directions**

As an undergraduate, I served as a leader for a student organization called MIT BrainTrust, which brought together students and individuals with brain injury in the Boston community. Our goals were to provide social support for people living with brain injury, to raise money and awareness for brain injury research, and to inspire students interested in science or medicine to improve health care and treatment of TBI. Working with this organization and hearing the stories of so many individuals with brain injury was a driving factor in choosing my field of study in graduate school. I wanted to do TBI research, with the hope that my discoveries could eventually improve the lives of the friends I had made through BrainTrust.

My thesis work aimed to 1) better understand basic mechanisms of neuronal functions like persistent activity in working memory, which we found is supported by conditional bistability in PFC neurons, 2) investigate how the brain is altered by TBI, and 3) identify potential new therapeutic targets for preventing or treating post-TBI health issues. We looked beyond the injury site, and investigated how TBI changes cellular and circuit excitability across the entire corticothalamic circuit. Importantly, we examined these outcomes three weeks post-TBI, a chronic time point, to understand which effects last longer than others and which might be better targets for treatment. Our findings indicate that while most of the corticothalamic circuit has returned to normal excitability levels by three weeks, the nRT has a significantly lower frequency of spontaneous inhibitory postsynaptic currents. Future studies using cell-type-specific labeling or optogenetic targeting of specific nRT inputs could address remaining questions like which nRT neurons (ex. parvalbumin-expressing vs. somatostatin-expressing, see (Clemente-Perez et al., 2017)) are experiencing this deficit, and whether the synaptic deficit is coming from one or more upstream brain regions.

We also considered the role of one particular inflammatory pathway, the C1q complement pathway, which has been implicated in TBI in a few studies (Al Nimer et al., 2013; Bellander et

al., 2001; Krukowski et al., 2018; Manek et al., 2018; Rostami et al., 2013; von Gertten et al., 2005; You et al., 2007) but whose role had not been studied in detail, particularly in the corticothalamic circuit. We showed that the C1q pathway has a major effect on regulating inflammation and neuron loss in the corticothalamic circuit. Furthermore, we found that treating mice with an antibody that blocks the C1q complement pathway reduces chronic inflammation and nRT neuronal loss after TBI. We hope that future studies will determine if this antibody has other therapeutic effects in TBI, for example improving sensory processing or sleep. It would also be useful to understand the mechanisms of how glia and/or neurons respond to the antibody's effects, to know if there might be any adverse side effects or potential applications of the antibody in other therapeutic contexts.

Our use of electrophysiological techniques has given us valuable information about how the intrinsic, synaptic, and bulk cortical activity of the corticothalamic circuit are chronically altered by TBI, which we examined at a very detailed level. In addition to the reduction of nRT sIPSCs, we saw that TBI mice had increased power in the delta frequency band (1-4 Hz), which is prominent in behavioral states including sleep. Future studies should probe in more detail how these changes might relate not only to sleep disruption, but also to other behavioral outcomes of TBI such as memory loss or epilepsy. We have started a collaboration with Anita Luthi's lab at the University of Lausanne to study whether sleep architecture is altered in TBI, and whether blocking the C1q pathway might improve or restore sleep patterns in TBI mice.

Our preliminary studies testing the potential therapeutic effects of small molecules have just started to scratch the surface. Further studies are needed to understand how RA8, a molecule which alters astrocyte transcriptional states, might be able to protect the brain from chronic inflammation after TBI. We have seen positive outcomes in a mouse model of stroke and we hypothesize that it may have similar protective effects in our TBI model. We are also interested in another small molecule, SM2 (also known as CH-223191), which was also identified as a candidate in a drug screen by our collaborators in Sheng Ding's lab at the Gladstone Institutes



(Kim et al., 2006). SM2 is an antagonist of aryl hydrocarbon receptors, and it is thought to protect cell bodies from dying after axon degeneration (Shackleford et al., 2018), which is a major cause of neurodegeneration in TBI. We have just started investigating the effects of SM2 in our TBI mouse model.

Rodent models of TBI are useful for answering many questions and dissecting circuit mechanisms that could not be studied in humans. However, it is important to find ways to bridge the gap between animal model research and human research in order to make meaningful progress in treating people with brain injury. This project was inspired in part by clinical discoveries, and in turn we hope that our discoveries will inform future clinical TBI studies.

## References

- Al Nimer, F., Lindblom, R., Ström, M., Guerreiro-Cacais, A.O., Parsa, R., Aeinehband, S., Mathiesen, T., Lidman, O., Piehl, F., 2013. Strain influences on inflammatory pathway activation, cell infiltration and complement cascade after traumatic brain injury in the rat. *Brain Behav. Immun.* 27, 109–122.
- Bellander, B.-M., Bendel, O., Von Euler, G., Ohlsson, M., Svensson, M., 2004. Activation of microglial cells and complement following traumatic injury in rat entorhinal-hippocampal slice cultures. *J. Neurotrauma* 21, 605–615.
- Clemente-Perez, A., Makinson, S.R., Higashikubo, B., Brovarney, S., Cho, F.S., Urry, A., Holden, S.S., Wimer, M., Dávid, C., Fenno, L.E., Acsády, L., Deisseroth, K., Paz, J.T., 2017. Distinct Thalamic Reticular Cell Types Differentially Modulate Normal and Pathological Cortical Rhythms. *Cell Rep* 19, 2130–2142.
- Kim, S.-H., Henry, E.C., Kim, D.-K., Kim, Y.-H., Shin, K.J., Han, M.S., Lee, T.G., Kang, J.-K., Gasiewicz, T.A., Ryu, S.H., Suh, P.-G., 2006. Novel compound 2-methyl-2H-pyrazole-3-carboxylic acid (2-methyl-4-o-tolylazo-phenyl)-amide (CH-223191) prevents 2,3,7,8-TCDD-induced toxicity by antagonizing the aryl hydrocarbon receptor. *Mol. Pharmacol.* 69, 1871–1878.
- Krukowski, K., Chou, A., Feng, X., Tiret, B., Paladini, M.-S., Riparip, L.-K., Chaumeil, M.M., Lemere, C., Rosi, S., 2018. Traumatic Brain Injury in Aged Mice Induces Chronic Microglia Activation, Synapse Loss, and Complement-Dependent Memory Deficits. *Int J Mol Sci* 19.

Manek, R., Moghieb, A., Yang, Z., Kumar, D., Kobessiy, F., Sarkis, G.A., Raghavan, V., Wang, K.K.W., 2018. Protein Biomarkers and Neuroproteomics Characterization of Microvesicles/Exosomes from Human Cerebrospinal Fluid Following Traumatic Brain Injury. *Mol. Neurobiol.* 55, 6112–6128.

Rostami, E., Davidsson, J., Gyorgy, A., Agoston, D.V., Risling, M., Bellander, B.-M., 2013. The terminal pathway of the complement system is activated in focal penetrating but not in mild diffuse traumatic brain injury. *J. Neurotrauma* 30, 1954–1965.

Shackleford, G., Sampathkumar, N.K., Hichor, M., Weill, L., Meffre, D., Juricek, L., Laurendeau, I., Chevallier, A., Ortonne, N., Larousserie, F., Herbin, M., Bièche, I., Coumoul, X., Beraneck, M., Baulieu, E.-E., Charbonnier, F., Pasmant, E., Massaad, C., 2018. Involvement of Aryl hydrocarbon receptor in myelination and in human nerve sheath tumorigenesis. *Proc. Natl. Acad. Sci. U.S.A.* 115, E1319–E1328.

von Gertten, C., Flores Morales, A., Holmin, S., Mathiesen, T., Nordqvist, A.-C.S., 2005. Genomic responses in rat cerebral cortex after traumatic brain injury. *BMC Neurosci* 6, 69.


You, Z., Yang, J., Takahashi, K., Yager, P.H., Kim, H.-H., Qin, T., Stahl, G.L., Ezekowitz, R.A.B., Carroll, M.C., Whalen, M.J., 2007. Reduced tissue damage and improved recovery of motor function after traumatic brain injury in mice deficient in complement component C4. *J. Cereb. Blood Flow Metab.* 27, 1954–1964.

## Publishing Agreement

It is the policy of the University to encourage open access and broad distribution of all theses, dissertations, and manuscripts. The Graduate Division will facilitate the distribution of UCSF theses, dissertations, and manuscripts to the UCSF Library for open access and distribution. UCSF will make such theses, dissertations, and manuscripts accessible to the public and will take reasonable steps to preserve these works in perpetuity.

I hereby grant the non-exclusive, perpetual right to The Regents of the University of California to reproduce, publicly display, distribute, preserve, and publish copies of my thesis, dissertation, or manuscript in any form or media, now existing or later derived, including access online for teaching, research, and public service purposes.

DocuSigned by:



5918EED8454344B...

Author Signature

6/2/2020

Date